ARCHIVES OF ACOUSTICS
21, 4, 359–360 (1996)

IN MEMORY OF PROFESSOR HALINA RYFFERT

On 7th August 1996, Polish Acoustics suffered a great loss when Professor Halina Ryffert, a woman of merit in the acoustical community, passed away.

She was born on 4th February 1916 in Bugulma (Russia) to a Polish family. Three years later they moved to Poznań (Poland), where Professor Ryffert lived and worked almost all her life.

She studied mathematics (1933-1939) at University in Poznań. Shortly after she graduated II World War broke out. As a result of her conspiratorial activity against the invader, Halina Ryffert was arrested and then sent to a concentration camp „Ravensbruck", where she stayed until the end of the war. She got back to Poland soon after the liberation in 1945 and started her work as an assistant in the Institute of Mathematics (University in Poznań). In 1952, she was offered a position with the Chair of Acoustics, where she continued her career as a scientist. She received Ph.D. degree in 1958, presenting her thesis on „Acquisition of instantaneous spectra on the basis of a generalized analysis of vibrations". Further work on methods for spectral analysis of non-stationary acoustic signals, conducted both in Poland and abroad during her fellowships at College de France in Paris (1958) and at Technical

University in Stuttgart (Germany, 1960), was a source of many publications. Her main achievement was the application of an instantaneous spectrum to a dynamic evaluation of non-stationary sounds. In 1968, Halina Ryffert became a Professor of Adam Mickiewicz University.

She headed the Chair of Acoustics for 19 years (1962-1981). For 7 years she was a Dean at the Department of Mathematics, Physics and Chemistry and a member of numerous academic boards. In 1965-1984, Proffessor Ryffert was a President of Polish Acoustical Society, converging people interested in diverse fields of Acoustics. During that time she made efforts to set a collaboration with acoustical centres abroad. Those efforts resulted in a particularly fruitful collaborative work with GALF. Since the establishment of Acoustics Commitee of Polish Academy of Sciences in 1964, Professor Halina Ryffert was its Vice-President for 20 years and then its meritorious member.

She was a dedicated academic teacher. Under her supervision, many master and doctoral thesis were completed.

In reward for her scientific and pedagogic work she received high honours both in Poland and abroad.

Her contribution to the development of Polish acoustics is invaluable. She turned the Chair of Acoustics into a thriving acoustical centre – present Institute of Acoustics in Poznań.

Always helpful and understanding, she was a respectable scientist and a great woman. She will remain our mentor. Her passing away is an irreparable loss.

Prof. dr hab. Edward Hojan

ARCHIVES OF ACOUSTICS
21, 4, 361–369 (1996)

ACOUSTIC FIELD MEASUREMENTS USING A PVDF FOIL HYDROPHONE

G. ŁYPACEWICZ, A. NOWICKI, R. TYMKIEWICZ, P. KARŁOWICZ and W. SECOMSKI

Institute of Fundamental Technological Research Polish Academy of Sciences
(00-049 Warszawa, Świętokrzyska 21)

This study was concerned with a membrane, pdvf foil and double-screened hydrophone, manufactured by Sonic Technologies, USA. Using the producer's data in the form of discrete data, power functions, describing the input impedance and the sensitivity of the hydrophone, depending on the frequency, were found. This made it possible to represent the measuring system in the form of a equivalent circuit containing a pressure source, a transformer which converted the acoustic pressure into the electric intensity (the hydrophone sensitivity), the hydrophone impendance, an additional coaxial cable and the input receiver impedance. The impacts of the receiver impedance and that of the additional cable on the accuracy of measurements of the acoustic pressure using a hydrophone were subsequently investigated.

As an example, an ultrasonographic measurement using the hydrophone in question was cited.

1. Introduction

The broad application of ultrasound methods in medical diagnostics requires accurate knowledge of the intensities of acoustic waves being applied. Ultrasonography is considered a safe method for the patient, but to an even greater extent this obliges producers and doctors to define accurately the doses used in the course of an examination. Ultrasound fields are defined by a number of parameters – the wave frequency, the repetition frequency, the pulse duration, the beam cross-section and the wave intensity – the maximum and mean ones in time and space. The mechanism of the impact of ultrasound on the organism is complex [3], depending to a varying degree on each of these quantities. Therefore, measurements of the diagnostic apparatus are performed in keeping with the recommendations of international standards developed by the IEC (the International Electrotechnical Commission) [1], [4], which recommend that a foil hydrophone should by applied for this purpose.

The object of this study is a membrane hydrophone of PVDF foil, screened on both sides, with a 60 cm long coaxial cable, and produced by Sonic Technologies, USA. The producers give its sensitivity and input impedance for frequencies from

1 to 20 MHz. Oscilloscopes with different input impedances and capacitances are applied in measurements. When the hydrophone cable is too short it is elongated by an additional cable. The producers give a formula for calculating the hydrophone sensitivity, depending on the input impedance of the receiver and the additional cable, which is treated as lumped capacitance. To check the admissibility of this approximation and to investigate more accurately the impact of the additional cable on the pressure measurement, it was represented in the form of a long line. Then, functions were found which described the input impedance and sensitivity, depending on the frequency and a equivalent circuit of the measuring system was applied in the further analysis. In the work performed at the Department on the design and work analysis of ultrasound transmitting-receiving systems their equivalent circuits were used, in the form of a chain of four-terminal networks, and so was the FFT technique [6], [7]. The representation of the measuring hydrophone in an analogous way will make it possible for it to be read in a simple way into computer programmes developed by the authors and to analyze systems with a receiving transducer in the form of a hydrophone.

2. The parameters of the hydrophone

Piezoelectric foil hydrophones are usually built in two versions a needle or foil extended over a ring with a diameter of several cm, with sputtered electrodes of diameters below 1 mm [2]. Because of good acoustic matching to water, the latter do not disturb significantly the acoustic field being measured.

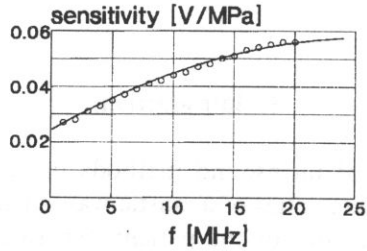

Fig. 1. Sensitivity modelling using the power functions (the circles denote the producer's data).

An analysis of measurements using a hydrophone produced by Sonic Technologies, USA, will be presented below. The producer gives the characteristics of sensitivity and input impedance of the hydrophone as a function of the frequency f in the range of 1 to 20 MHz [5]. To examine the impact of the parameters of the receiving system on the accuracy of measurements, the parameters of the hydrophone were described with power functions. The sensitivity function of the hydrophone was adopted in the following form:

$$a\left(\frac{f-b}{b}\right)^2+c,$$

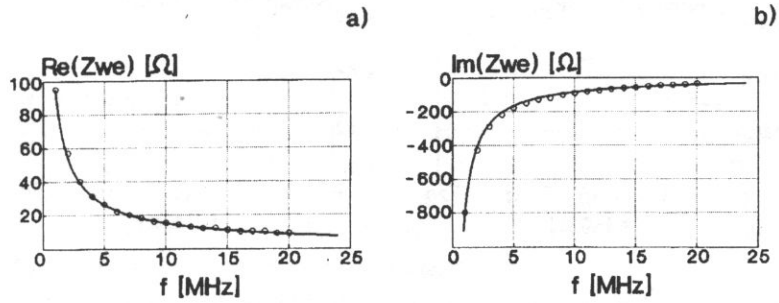

Fig. 2. Modelling of the real part (a) and the imaginary part (b) of the input impedance of the hydrophone (the circles denote the producer's data).

while the constants a, b and c were varied so that the calculated curve would coincide with the producer's data. It was achieved for a = -0.335, b = 26.5 and c = 0.0578.

The impedance of the hydrophone was described by the functions

$$\mathrm{Re}(Z_{\mathrm{in}}(f)) = \frac{d}{f^g} \qquad \mathrm{Im}(Z_{\mathrm{in}}(f)) = \frac{h}{f^k}.$$

The calculated functions coincided with the producer's data for d = 95, g = 0.8, h = -815 and k = 0.955. Figure 1 shows the calculated sensitivity curves, whereas Fig. 2 represents the real part (a) and the imaginary part (b) of the impedance of the hydrophone, along with the producer's data marked with points. It can be seen that the curves coincide with the points, therefore, the work of the hydrophone may be described using the system shown in Fig. 3. It includes a pressure source, a four-terminal network, describing a transformer which converts the acoustic pressure into the electric voltage (the hydrophone sensitivity), the hydrophone impedance, a coaxial cable in the form of a long line and the input impedance of the receiver in a parallel system of resistances and capacitances.

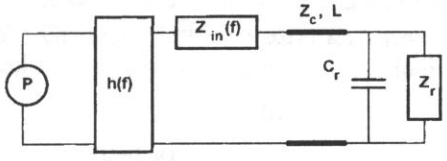

Fig. 3. A equivalent circuit for the hydrophone: P the measured pressure, $h(f)$ a fourterminal network representing a transformer which converts the acoustic pressure P into intensity (with the hydrophone sensitivity as a function of frequency), $Z_{\mathrm{in}}(f)$ – the input impedance of the hydrophone, Z_cL the additional coaxial cable (with the characteristic impedance Z_c and the lenght L), Z_r the input receiver impedance and C_r the input receiver capacitance.

To examine the impact of the impedance of the receiver and the parameters of the additional coaxial cable on the accuracy and sensitivity of field measurements using the hydrophone, the received transmission functions and electric pulses were calculated with the assumption of the acoustic pressure in the form of one sinusoid course with a frequency of 3.5 MHz and an amplitude of 1 MPa [6], [7].

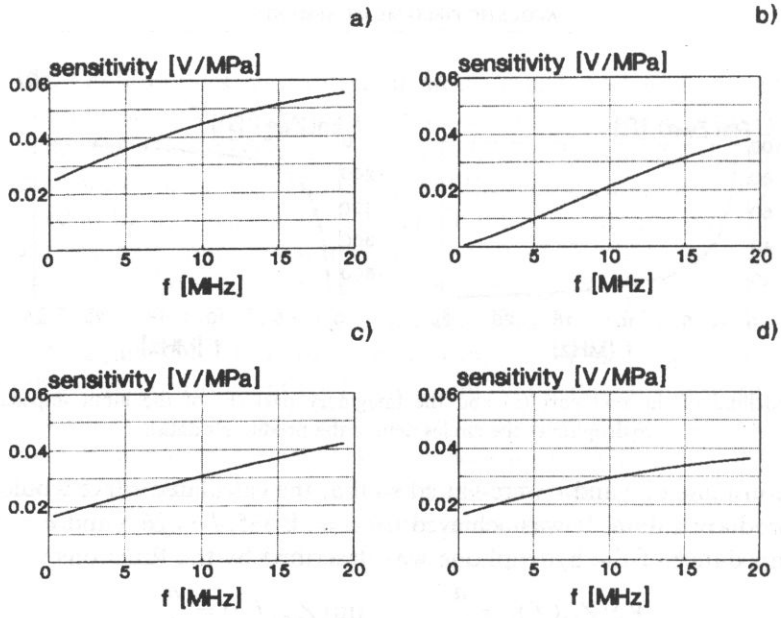

Fig. 4. Hydrophone sensitivities for dirrerent input receiver impedances:
a – 1MΩ, 0 pF, no additional cable,
b – 50Ω, 0 pF, no additional cable,
c – 1MΩ, 0 pF, an additional 1 m cable,
d – 1 MΩ, 100 pF, no additional cable.

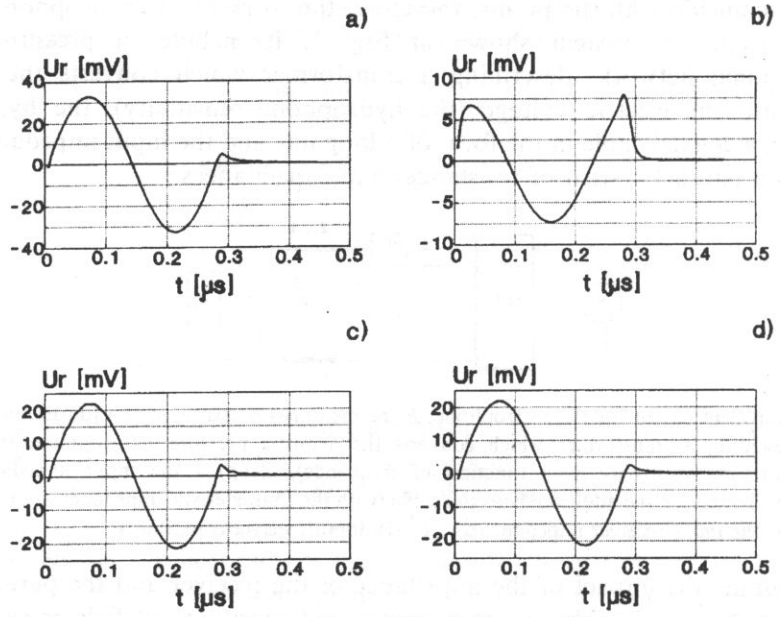

Fig. 5. The pulses detected by the hydrophone as in Fig. 4. The transmitted pressure pulse in the form of a single sinusoid with a frequency of 3.5 MHz and an amplitude of 1 MPa.

The results of these calculations are shown in Figs. 4 and 5. Figures 4a and 5a show the results calculated for the optimum case, for a system without an additional cable and a receiver with the real impedance of 1MΩ, i.e., for the producer's data.

Figures 4b and 5b show the results calculated for the receiver impedance of 50Ω. It can be seen that the low-ohm input of the receiver causes a sensitivity drop; moreover, it is distinctly greater for low frequencies, which, in turn, causes a disastrous distortion of the pulse. Therefore, it should be borne in mind that a high-ohm input of the receiver should be applied.

Figures 4c and 5c show the results calculated for a system with an additional, 1 m long cable. It can be seen that the addition of the cable causes lower sensitivity, but the shape of the pulse does not deteriorate visibly.

Therefore, the hydrophone producers [2], [3] recommend that the sensitivity drop should be considered, in keeping with the formula

$$M_{\text{eff}} = M_c \left\{ \frac{\text{Re}(Z_L)^2 + \text{Im}(Z_L)^2}{[\text{Re}(Z_L) + \text{Re}(Z)]^2 + [\text{Im}(Z_L) + \text{Im}(Z)]^2} \right\}^{1/2},$$

where Z_L – the impedance of the measuring device (the receiver and cable), Z – the hydrophone impedance, M_c – the sensitivity given by the producer.

According to the producer, an additional cable should be regarded as lumped capacitance. In order to check the validity of this assumption and to examine more accurately the impact of the impedance of the measuring equipment on the sensitivity and shape of the pluses received, the sensitivity and pulses received by the hydrophone were calculated for the case when lumped capacitance, equal to the capacitance of a 1 m long open cable, i.e., one of 100 pF, was added. Comparing the results of hydrophone sensitivity calculations when the lumped capacitance is added (Fig. 4d) with those obtained with an added cable (Fig. 4c), it can be seen that the sensitivity curves are close to each other at low frequencies. It is permissible to treat the cable as lumped capacitance (of 100 pF in this case) up to about 10 MHz. On the other hand, at higher frequencies, the error committed for this assumption grows, reaching 10% at 20 MHz (the hydrophone is scaled up to this frequency).

3. Conclusion

The equivalent circuit of the system for measuring acoustic pressures will make it possible to read it into the computer programmes developed by the authors for the purposes of not only designing ultrasound transmitting-receiving systems, but also conducting analyses of systems with a receiving transducer in the form of a hydrophone.

Foil hydrophones are primarily applied for measuring ultrasound wave doses in diagnostic apparatus. The mechanism of the impact of ultrasound on the organism is complex, depending on particular parameters, such as the wave frequency, the repetition frequency, the pulse duration, the beam cross-section, the wave intensity

the maximum and those averaged in time and space. Knowledge of these quantities is necessary from the point of view of the patient safety and the research on the ultrasound impact on living organisms.

Only the impact of the electric circuit on the measured results was discussed in this study. When measuring the acoustic field distribution it should be borne in mind that these measurements involve an error which results from the finite hydrophone diameter comparable to the wavelength being measured. The measurement error diminishes as the distance from the transducer grows, and, according to the standards, it may be neglected when the following condition is satisfied for the hydrophone radius [2]:

$$b_{\mathrm{Max}} = \frac{\lambda}{4}\left[(1/2a)^2 + 0.25\right]^{1/2},$$

where 1 – the distance from the transducer and a – the transducer radius.

It should also be borne in mind that the hydrophone sensitivity as a function of frequency is provided by the producer for measurements along the axis of the transducer being measured; the higher the frequency, i.e., the shorter the wave, to the greater extent the directivity grows. Usually, the producer provides directivity curves for a few chosen frequencies.

4. Appendix: Measurements of the ultrasonographic parameters in keeping with international standards

The development of foil hydrophones facilitated measurements of the parameters of ultrasound diagnostic apparatus in keeping with the requirements of international standards of the IEC (the International Electrotechnical Commission). As an example, the relevant definitions as introduced by the ICC [1] are shown and so are the methods for measuring excited to vibration, resembling the one applied in ultrasonographs manufactured by Echoson S.A.

The pulses applied in ultrasonography should be as short as possible, with a wide frequency band. The **pulse frequency** is defined as the arithmetic mean from the lobe frequencies of the main pulse spectrum as read out for a 6 dB drop in the spectrum amplitude. Fig. 6a shows a pulse measured by the hydrophone and in Fig. 6b its Fourier transform may be seen.

In keeping with the definition, the pulse frequency is $f_0 = \dfrac{f_1 + f_2}{2} = 2.4$ MHz.

The amplitude of an electric pulse as measured using a hydrophone placed in the focus of the probe was $U_m = 0.04$ V. **The pressure amplitude in the focus** may be calculated taking into account the hydrophone sensitivity M for the measured frequency (in the case under consideration, it was 2.4 MHz).

$$p_{\mathrm{m}} = U_m \,/\, M = 0.04\mathrm{V} \,/\, 0.028\,\frac{\mathrm{V}}{\mathrm{MPa}} = 1.43\ \mathrm{MPa}.$$

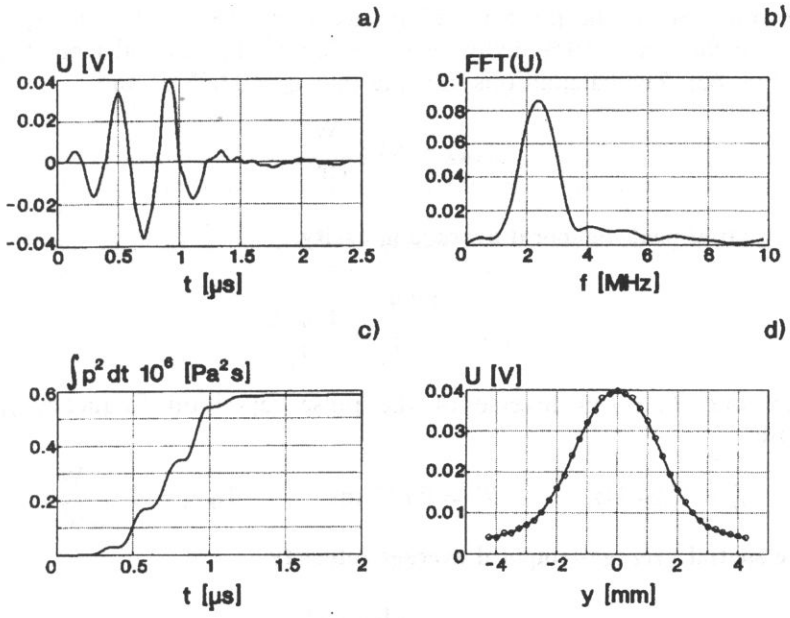

Fig. 6. The ultrasonographic parameters having been measured using the hydrophone. The acoustic pulse in the focus (a), its Fourier transform (b), an integral over time with a squared pressure (c) and the focal pressure distribution (d).

The mechanism of the ultrasound wave impact on the human organism is complicated. Therefore, it was necessary to perform accurate measurements of such parameters of the wave as could be responsible for mechanical, thermal or cavitation impacts. International standards recommend that measurements should be taken not only of the maximum wave intensity in the focus, but also **the one averaged it time and space.** The subscripts introduced in the intensity terms reflect the first letters of English words:
maximum – m, spatial – s, temporal – t, peak – p, averaged following a pulse – p and average – a.

The intensities are measured with the assumption that the wave is a plane one; this is met in practice as the measurements are carried out in the focal plane.

I_{SPTP} — the spatial peak-temporal peak intensity:

$$I_{SPTP} = \frac{p^2}{Z} \qquad I_{SPTP} = 136 \frac{W}{cm^2}$$

($Z = 1.5 \cdot 10^6 \frac{kg}{m^2 s}$ – the acoustic water impedance);

I_{SPPA} – the spatial peak – pulse avarege intensity:

$$I_{SPPA} = \frac{\int_{t_d} p^2 dt}{Z t_d},$$

where the duration of the pulse is defined as: $t_d = 1.25(t_2 - t_1)$, and t_2 and t_1 are calculated for 90% and 10% drops in the value of the integral from the squared pressure (Fig. 6c). The calculations indicate that $t_d = 0.625$ μs and

$$\mathrm{I_{SPPA}} = 54.5 \frac{\mathrm{W}}{\mathrm{cm}^2},$$

$\mathrm{I_{SPTA}}$ – the spatial peak-temporal avarage intensity:

$$\mathrm{I_{SPPA}} = \frac{\int_T p^2 dt}{Z T_p} = \frac{\mathrm{I_{SPPA}} t_d}{T_p},$$

where the time T_p is an inverse of the pulse repetition frequency f_p. In the present case,

$$f_p = 1224 \text{ Hz}, \qquad T_p = 0.817 \text{ ms}, \qquad \mathrm{I_{SPTA}} = 42 \frac{\mathrm{mW}}{\mathrm{cm}^2},$$

$\mathrm{I_{SATA}}$ – the spatial average-temporal average intensity:

$$\mathrm{I_{SATA}} = \frac{\int_A \mathrm{I_{SPTA}} dA}{A},$$

where A is the integration space.

Figure 6d shows the pressure distribution in the focus as measured using the hydrophone. By calculating the integral over the surface and by averaging it, the following result is obtained:

$$\mathrm{I_{SATA}} = 2 \frac{\mathrm{mW}}{\mathrm{cm}^2},$$

The ultrasonic power:

$$P = \int_A \mathrm{I_{SATA}} \, dA$$

For the measurements described above: $P = 0.96$ mW.

The results, presented in the Appendix, of the determination of the parameters of the acoustic field radiated by an ultrasound probe are examples of measurements and should be carried out by all producers or users of ultrasound devices, in keeping with the recommendations of international standards as developed by the IREC (the International Electrotechnical Commission).

5. References

[1] K. BREDEL, *Hydrofone measurements*, pp. 116-125 in: Ultrasonic Exposimetry, [Ed.] M. C. Ziskin, P. A. Lewin, CRC Press, Inc. N.W., Boca Raton, Florida, 1993.

[2] M. E. SCHAFER, *Techniques of hydrofone calibration*, pp. 217-257 in: Ultrasonic Exposimetry, [Ed.] M. C. Ziskin, P. A. Lewin, CRC Press, Inc. N.W., Boca Raton, Florida, 1993.

[3] K. E. THOMENIUS, *Estimation of the potential for bioeffects*, pp. 371–407 in: Ultrasonic Exposimetry, [Ed.] M. C. Ziskin, P. A. Lewin, CRC Press, Inc. N.W., Boca Raton, Florida, 1993.

[4] IEEE Transactions on Ultrasonics, Ferroelectrics, and Frequency Control, **35**, No 2, 87-213, 1988.

[5] *Test methodology report* (M.E. Schafer, D. Hillegass), Sonic Technologies, 2935 Byberry Rd., Hatboro, PA 1940.

[6] G. ŁYPACEWICZ, *Piezoelectric transmitting-receiving systems applied for ultrasonagraphic purposes* (in Polish), Reports of the Institute of Fundamental Technological Research, the Polish Academy of Sciences, 22/1995.

[7] G. ŁYPACEWICZ, *Influence of the electrical parameters on the ultrasonic probe impedance and the reflected pulses*, Archives of Acoustics., **19**, 4, 47-66, (1994).

ARCHIVES OF ACOUSTICS
21, 4, 371–386 (1996)

CALCULATIONS OF EFFECTIVE MATERIAL TENSORS AND THE ELECTROMECHANICAL COUPLING COEFFICIENT OF A TYPE 1-3 COMPOSITE TRANDSUCER

K. KYCIA*, A. NOWICKI*, O. GAJL* and T. D. HIEN**

* Institute of Fundamental Technological Research,
Polish Academy of Sciences
(00-049 Warsaw, 21 Świętokrzyska Street)

** Ocean and Ship Technology Institute,
Technical University of Szczecin
(71-065 Szczecin, 41 Aleja Piastów)

In this paper the purpose and manner of conducting the process of asymptotic homogenization of a type 1-3 composite structure are presented. The formulation of the homogenization process is reduced to numerical static analysis of an elementary symmetry cell of the composite with generalized forces applied at the boundaries of material phases. It is demonstrated that the effective values of the material tensors of the composite depend not only on the tensors of the component materials, but also on variability course of the aforementioned tensors defined over the volume of the solid of an elementary symmetry unit of the composite. The latter factor becomes particularly significant in the case of a step-like discontinuity which occurs, e.g., in the type 1-3 composite structure.

1. Introduction

A type 1-3 composite piezoelectric and polymer ultrasound transducer (Fig. 1), used in ultrasonic medical diagnosis, is characterized by a number of desirable properties compared with a typical piezoceramic transducer made from lead titanate and zirconate.

These properties are as follows:

1 – Acoustic impedance of the composite equal to 8-10 MRayl is matched better, acoustically to anatomical tissue with impedance of 1.5 MRayl than piezoceramics with impedance of 33 MRayl.

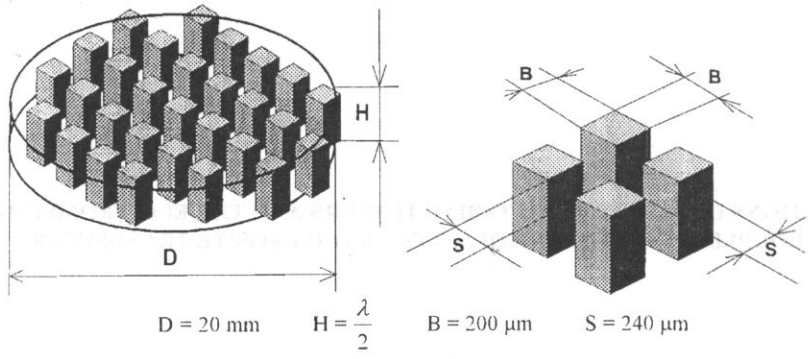

Fig. 1. Structure of the type 1-3 composite transducer.

2 – Reduction of the energy coefficient of the reflection at the transducer-tissue boundary (which results from property 1), from 85% for piezoceramics to 50% for the composite.

3 – Energy efficiency of the transducer, measured by the value of the electromechanical coupling coefficient, is half as high for the composite (60%) than for the piezoceramics (40%).

4 – The greater broad-band width of the composite transducer than that of the piezoceramic one because it is not necessary to use thin quaterwave layers for the reason given in point 1.

5 – The technological workability of forming composite solids with a predetermined curvature radius, eliminating the necessity of using acoustic lenses if it is necessary to obtain focussed heads.

6 – The possibility of making a dynamically focussed head without having to work the material of the transducer itself – by depositing one of the electrodes on the composite transducer, in the form of insulated concentric metallized rings.

The analytical calculation of the electroacoustic quantities of the composite transducer is extremely difficult because all the three dimensions of the smallest symmetry element of the transducer are commensurable with the length of the transmitted longitudinal ultrasonic wave (a threedimensional problem).

An alternative approach is based on the finite element method (FEM) in which the calculations of the electromechanical coupling coefficient consist in the determination of the energy quantities of both the electromagnetic field and the stress and strain fields in the transducer solid.

In practice, the energy quantities can be calculated using the FEM only for a small fragment of the composite soild because of the second power increasing order of magnitude of the rigidity matrix as the total number of degrees of freedom increases. It is possbile to perform, on the other hand, a dynamic analysis of the whole composite solid by dividing the numerical problem into the two following stages:

1 – A static analysis of the elementary symmetry unit of the composite, leading to the determination of substitute material tensors of a hypothetical homogeneous structure.

2 – A dynamic analysis of a substitute homogenous composite structure of the whole solid [2]. In the proposed, modified process of the numerical solution, the FEM mesh nodes is extended twice, and independently of one another. Each time the FEM network generated in this way reaches a degree of densification which is upper-bound only by the order of the global rigidity matrix permitted by the computing applied environment. At the first stage, it applies only to the volume limited to a single elementary cell, and the large density of the FEM network on the elementary volume means high accuracy of calculations of substitute material tensors. At the next homogeneous as a whole, and the homogenized material does not require the necessary densification of the FEM network close to the discontinuity zones – which would be necessary in the composite. As an effect, it becomes possible to perform a dynamic analysis of the whole solid with a much reduced total number of degrees of freedom relative to the unmodified FEM solution. This is achieved without diminishing the calculation accuracy.

2. Asymptotic homogenization of the elementary cell of a transducer

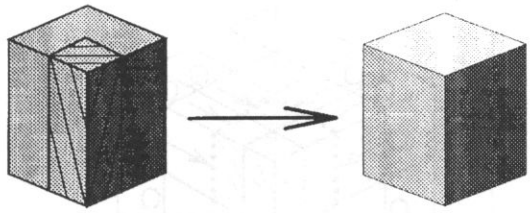

Fig. 2. The idea of homogenization of the elementary cell of the composite transducer.

The purpose of homogenization of the elementary cell of a composite transducer (Fig. 2) is to determine the substitute elementary symmetry unit built of hypothetical homogeneous material. This material shows values of effective material tensors related to:

1 – The averaged values of the tensors of the component materials of the composite

2 – A step-like character of changes in the physical properties at the boundaries of the material phases in the volume of the elementary symmetry unit of the composite solid (3).

The process of homogenization of the composite soild can begin with asymptotic transformation [4]. A composite soild with a periodical structure consisting of the volume Ω is considered (Fig. 3). The object under consideration is only the solid Ω with its total size much larger than that of its single elementary symmetry unit Y.

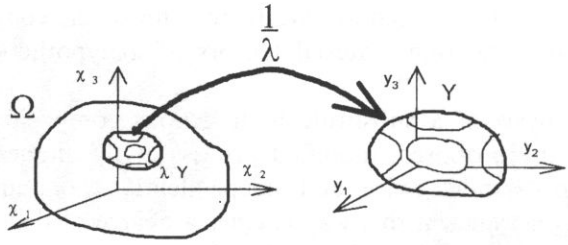

Fig. 3. A transformation of the coordinate system.
(χ_1, χ_2, χ_3) – the global coordinate system,
(y_1, y_2, y_3) – the local coordinate system,
Ω – the composite solid,
Y – the symmetry element.

The matrix notation will be employed throughout in the text. The tensorial notation will be used at places with specific comments, summation over twice repeated indices being employed. The above assumption is defined in equation (1), where dia (Ψ) is the characteristic dimension of the solid (Ψ).

$$\lambda = \frac{\text{dia}(Y)}{\text{dia}(\Omega)} \ll 1. \tag{1}$$

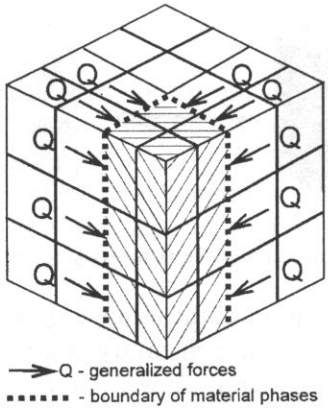

Fig. 4. Static analysis with the division 4x4x3 of the elementary.

The assumption formulated in equation (1) provides the basis for an asymptotic analysis of the solid of composite material with the parameter λ tending to zero (Fig. 3) [6].

In keeping with Fig. 4, the coordinate system is transformed from the global system of the solid (χ_1, χ_2, χ_3) to the local one (y_1, y_2, y_3) related to a single symmetry element of the composite. In the course of the transformation, the scale of the axes of the coordinate system changes, as shown by equation (3).

$$x_i = \bar{\mathbf{x}}_i + y_i, \tag{2}$$

$$\{\mathbf{y}_i\} = \frac{\{\mathbf{x}_i\}}{\lambda} \tag{3}$$

In equation (2), $\mathbf{x}_i$ is the tracking vector, while in (3) $\{x_i\}$ and $\{y_i\}$ are the lengths of unit vectors of the axes x_i and y_i, respectively.

Considering (2) and (3), the partial derivative with respect to the variable x_i can be written in the form of (4),

$$\frac{\partial}{\partial x_i} = \frac{\partial}{\partial \bar{x}_i} + \frac{1}{\lambda}\frac{\partial}{\partial y_i}. \tag{4}$$

In the further analysis, the symmetrical gradient operator sym ∇_{x_i}(5) and the divergence operator div_{x_i} (6) will be applied

$$\mathrm{Sym}\,\nabla_{x_i} = \begin{bmatrix} \frac{\partial}{\partial x_1} & 0 & 0 \\ 0 & \frac{\partial}{\partial x_2} & 0 \\ 0 & 0 & \frac{\partial}{\partial x_1} \\ 0 & \frac{\partial}{\partial x_3} & \frac{\partial}{\partial x_2} \\ \frac{\partial}{\partial x_3} & 0 & \frac{\partial}{\partial x_1} \\ \frac{\partial}{\partial x_2} & \frac{\partial}{\partial x_1} & 0 \end{bmatrix}, \tag{5}$$

$$\mathrm{div}_{x_i} = \begin{bmatrix} \frac{\partial}{\partial x_1} & 0 & 0 & 0 & \frac{\partial}{\partial x_3} & \frac{\partial}{\partial x_2} \\ 0 & \frac{\partial}{\partial x_2} & 0 & \frac{\partial}{\partial x_3} & 0 & \frac{\partial}{\partial x_1} \\ 0 & 0 & \frac{\partial}{\partial x_3} & \frac{\partial}{\partial x_2} & \frac{\partial}{\partial x_1} & 0 \end{bmatrix}. \tag{6}$$

The notation of the partial derivative with respect to the variable x_i in (4) determines the form of the Nabel operator (7), the symmetrical gradient operator (8), the gradient operator (9) and the divergence operator (10).

$$\nabla_{x_i} = \nabla_{\bar{x}_i} + \frac{1}{\lambda}\nabla_{y_i}, \tag{7}$$

$$\mathrm{sym}\,\nabla_{x_i} = \mathrm{sym}\,\nabla_{\bar{x}_i} + \frac{1}{\lambda}\mathrm{sym}\,\nabla_{y_i}, \tag{8}$$

$$\operatorname{grad}_{x_i} = \operatorname{grad}_{\bar{x}_i} + \frac{1}{\lambda}\operatorname{grad}_{y_i}, \tag{9}$$

$$\operatorname{div}_{x_i} = \operatorname{div}_{\bar{x}_i} + \frac{1}{\lambda}\operatorname{div}_{y_i}, \tag{10}$$

In keeping with (11) and (12), the two independent variables of the electroacoustic field, the displacement u and the potential Φ, can be expanded into convergent asymptotic expansions:

$$u(\bar{x}, y) = u_0(\bar{x}, y) + \lambda u_1(\bar{x}, y) + \lambda^2 u_2(\bar{x}, y) + \ldots, \tag{11}$$

$$\Phi_0(\bar{x}, y) = \Phi_0(\bar{x}, y) + \lambda \Phi_1(\bar{x}, y) + \lambda^2 \Phi(\bar{x}, y) + \ldots \tag{12}$$

The problem of the electroacoustic field wave propagation in the composite material containing a piezoelectric component is formulated in the form of a system of six equations (13) – (18):

$$\operatorname{div}_x \mathbf{T}(\bar{x}, y) = \rho(y)\ddot{\mathbf{u}}(\bar{x}, y), \tag{13}$$

$$\operatorname{div}_x \mathbf{D}(\bar{x}, y) = 0, \tag{14}$$

$$\mathbf{T}(\bar{x}, y) = c(y)\mathbf{S}(\bar{x}, y) - e(y)\mathbf{E}(\bar{x}, y), \tag{15}$$

$$\mathbf{D}(\bar{x}, y) = e(y)\mathbf{S}(\bar{x}, y) + \varepsilon(y)\mathbf{E}(\bar{x}, y), \tag{16}$$

$$\mathbf{S}(\bar{x}, y) = \operatorname{sym}_x u(\bar{x}, y), \tag{17}$$

$$\mathbf{E}(\bar{x}, y) = -\nabla_x \Phi(\bar{x}, y), \tag{18}$$

where $\mathbf{u}$ is the vector of mechanical displacement, Φ is the scalar of the electric potential, $\mathbf{S}$ is the displacement tensor, $\mathbf{T}$ is the stress tensor, $\mathbf{E}$ is the vector of the intensity of the electric field, $\mathbf{D}$ is the vector of electric induction, ρ is the scalar of mass density, $\mathbf{c}$ is the tensor of mechanical rigidity, $\mathbf{e}$ is the piezoelectric tensor and $\boldsymbol{\varepsilon}$ is the dielectric tensor.

Thus, equation (13) is a notation of Newton's second principle of dynamics for a continuous medium. Equation (14) is one of four Maxwell equations, stating that in the volume of the composite solid there are no free electric charges. Dependencies (15) and (16) contain a notation of the simple and converse piezoelectric effects which take place in the composite solid. Through (15) and (16), in the piezoelectric material there occurs the effect of coupling of the stresses and strains field with the electromagnetic one (through the nonzero tensor $\mathbf{e}$), which thus form one electroacoustic field. Dependence (17) is a principle which is generally valid in the continuous medium mechanics, linking the mechanical quantities of strain and displacement. Equation (18) determines the relation between the quantities of the

electric field the intensity and the potential. The expansion of the two independent variables of the electroacoustic field, the mechanical displacement u and the electric potential Φ, into convergent asymptotic series with respect to λ implies asymptotic expansions of all the derivative quantities (19) – (22):

$$\mathbf{S}(\bar{x}, y)= \lambda^{-2}S_{-2}(\bar{x},y)+\lambda^{-1}S_{-1}(\bar{x},y)+S_o(\bar{x},y)+\lambda S_1(\bar{x},y)+\lambda^2 S_2(\bar{x},y)+... \quad (19)$$

$$\mathbf{T}(\bar{x}, y) = \lambda^{-2}T_{-2}(\bar{x},y)+\lambda^{-1}T_{-1}(\bar{x},y)+T_o(\bar{x},y)+\lambda T_1(\bar{x},y)+\lambda^2 T_2(\bar{x},y)+... \quad (20)$$

$$\mathbf{E}(\bar{x}, y) = \lambda^{-2}E_{-2}(\bar{x},y)+\lambda^{-1}E_{-1}(\bar{x},y)+E_o(\bar{x},y)+\lambda E_1(\bar{x},y)+\lambda^2 E_2(\bar{x},y)+... \quad (21)$$

$$\mathbf{D}(\bar{x}, y)= \lambda^{-2}D_{-2}(\bar{x},y)+\lambda^{-1}D_{-1}(\bar{x},y)+D_o(\bar{x},y)+\lambda D_1(\bar{x},y)+\lambda^2 D_2(\bar{x},y)+... \quad (22)$$

The asymptotic expansions of equations (19)–(22) will also contain terms involving the powers of λ equal to minus one and minus two. It results from the fact that, in keeping with (17, 18 and 15, 16), all the derivatives (19)–(22) are functions od the mechanical displacement u and the electric potential Φ acted by the differential operators (7)–(10). In turn, operators (7)–(10) contain the partial derivatives (5, 6) in their structure. On the other hand, the partial derivatives (4) contain a component including the fraction $1/\lambda$. It is exactly the component that causes decreasing order of λ^k by one.

Subsequently the values of the **u**, Φ, **S**, **T**, **E**, **D** in equations (13) – (18) can be replaced by their infinite power expansions (11) – (12), (19) – (22). Then on both sides of the system of equations (13-18), there are only infinite power series with the given small parameter λ. The terms on both sides of the equations related to the same powers of λ are equal to one another. The terms containing the zero power of λ (23) – (28) can be compared:

$$S_0(\bar{x}, y) = \operatorname{sym}\nabla_{\bar{x}} u_0(\bar{x}, y), \quad (23)$$

$$E_0(\bar{x}, y) = -\nabla_{\bar{x}}\Phi(\bar{x}, y) - \nabla_y \Phi(\bar{x}, y), \quad (24)$$

$$T_0(\bar{x}, y) = c(y)S_0(\bar{x}, y) - e(y)E_0(\bar{x}, y) \quad (25)$$

$$D_0(\bar{x}, y) = e(y)S_0(\bar{x}, y) - \varepsilon(y)E_0(\bar{x}, y) \quad (26)$$

$$\operatorname{div}_y T_1(\bar{x}, y) + \operatorname{div}_{\bar{x}} T_0(\bar{x}, y) = \rho(y)\ddot{u}x(\bar{x}, y), \quad (27)$$

$$\operatorname{div}_y D_1(\bar{x}, y) + \operatorname{div}_{\bar{x}} D_0(\bar{x}, y) = 0. \quad (28)$$

Then, the same can be done for the terms which contain the power λ equal to minus one (29) – (34):

$$S_{-1}(\bar{x}, y) = \operatorname{sym}\nabla_y u_0(\bar{x}, y), \quad (29)$$

$$E_{-1}(\bar{x}, y) = -\nabla_y \Phi_0(\bar{x}, y), \quad (30)$$

$$T_{-1}(\bar{x}, y) = c(y)S_{-1}(\bar{x}, y) - e(y)E_{-1}(\bar{x}, y), \quad (31)$$

$$D_{-1}(\bar{x}, y) = e(y)S_{-1}(\bar{x}, y) - \varepsilon(y)E_{-1}(\bar{x}, y), \quad (32)$$

$$\operatorname{div}_y T_0(\bar{x}, y) + \operatorname{div}_{\bar{x}} T_{-1}(\bar{x}, y) = 0, \tag{33}$$

$$\operatorname{div}_y D_0(\bar{x}, y) + \operatorname{div}_{\bar{x}} D_{-1}(\bar{x}, y) = 0, \tag{34}$$

Finally, the terms containing the power of λ equal to minus two (35)–(40) can be compared:

$$S_{-2}(\bar{x}, y) = 0, \tag{35}$$

$$E_{-2}(\bar{x}, y) = 0, \tag{36}$$

$$T_{-2}(\bar{x}, y) = 0, \tag{37}$$

$$D_{-2}(\bar{x}, y) = 0, \tag{38}$$

$$\operatorname{div}_y T_{-1}(\bar{x}, y) = 0, \tag{39}$$

$$\operatorname{div}_y D_{-1}(\bar{x}, y) = 0. \tag{40}$$

The following two important dependencies result from equations (39)–(40) and (29)–(30):

$$\operatorname{div}_y \left[c(y) \operatorname{sym} \nabla_y u_0(\bar{x}, y) - e(y) \nabla_y \Phi_0(\bar{x}, y) \right] = 0, \tag{41}$$

$$\operatorname{div}_y \left[e(y) \operatorname{sym} \nabla_y u_0(\bar{x}, y) - \varepsilon(y) \nabla_y \Phi_0(\bar{x}, y) \right] = 0, \tag{42}$$

The system of equations (41)–(42) is satisfied in terms of identity only when the dependencies specified in equations (43 – 44) occur:

$$u_0(\bar{x}, y) = u_0(\bar{x}), \tag{43}$$

$$\Phi_0(\bar{x}, y) = \Phi_0(\bar{x}). \tag{44}$$

From (43)–(44), an important conclusion results concerning the terms of the zero order of the expansion of the two independent variables of the electroacoustic field, the displacement **u** (11) and the potential Φ (12), into power series. On the basis (43) – (44), it can be stated that these terms are independent of the local variable y.

Considering dependencies (43)–(44) in the system of equations (29)–(34), the following system of equations is obtained (45)–(50):

$$S_{-1}(\bar{x}, y) = 0, \tag{45}$$

$$E_{-1}(\bar{x}, y) = 0, \tag{46}$$

$$T_{-1}(\bar{x}, y) = 0, \tag{47}$$

$$D_{-1}(\bar{x}, y) = 0, \tag{48}$$

$$\operatorname{div}_y T_0(\bar{x}, y) = 0, \tag{49}$$

$$\operatorname{div}_y D_0(\bar{x}, y) = 0. \tag{50}$$

For a value of λ much lower than unity (for a solid with the geometry shown in Fig. 1, λ is approximately equal to 0.011), it is permissible to neglect in the asymptotic

expansion of any electroacoustic quantity Ψ all terms, apart from λ, related to the zero power (1). This means the approximation of the exact value Ψ of the term Ψ_0 of its asymptotic expansion. Then, the effecxtive value $\Psi_E(x)$ of any electroacoustic quantity Ψ on the volume of the symmetry element Y of the asymptotic expansion $\Psi(45)$. The volume of the symmetry element Y is designated as vol(Y).

$$\Psi_E(\bar{x}) \equiv \| \Psi_0(\bar{x}, y) \|_y \equiv \frac{1}{\mathrm{vol}(Y)} \fint\!\!\!\fint_Y \Psi_0(\bar{x}, y) dY. \tag{51}$$

As a result of applying operator (51), on both sides, in the system of equations (13) $-(18)$, the system of equations $(52)-(57)$, describing the relations between the effective quantities, that is, those averaged over the volume of the elementary cell Y, according to formula (45). The sought quantities are c^{EF}, e^{EF}, ε^{EF} – the effective values of the material tensors of the substitute homogeneous piezoelectric material with respect to the two-component composite in question.

$$\mathrm{div}_x T_E(\bar{x}) = \rho^{EF} \ddot{u}_E(\bar{x}), \tag{52}$$

$$\mathrm{div}_x D_E(\bar{x}) = 0, \tag{53}$$

$$T_E(\bar{x}) = c^{EF} \mathrm{S}_E(\bar{x}) - e^{EF} E_E(\bar{x}), \tag{54}$$

$$D_E(\bar{x}) = e^{EF} S_E(\bar{x}) + \varepsilon^{EF} E_E(\bar{x}), \tag{55}$$

$$S_E(\bar{x}) = \mathrm{sym} \nabla_x u_E(\bar{x}), \tag{56}$$

$$E_E(\bar{x}) = -\nabla_x \Phi_E(\bar{x}). \tag{57}$$

From equations (23) – (24), (43) – (44) and (56) – (57), the following dependencies (58) – (59) result:

$$S_0(\bar{x}, y) = S_E(\bar{x}) + \mathrm{sym} \nabla_y u_1(\bar{x}, y), \tag{58}$$

$$E_0(\bar{x}, y) = E_E(\bar{x}) - \nabla_y \Phi_1(\bar{x}, y), \tag{59}$$

From equations ((49) – (50), (23) – (26) and (58) – (59)), the following dependencies (60) – (61) result:

$$\mathrm{div}_y \left[c(y) \cdot \mathrm{sym} \nabla_y u_1(\bar{x}, y) - e(y) \cdot \nabla_y \Phi_1(\bar{x}, y) \right] = -\mathrm{div}_y c(y) \cdot S_E(\bar{x}) + \\ + \mathrm{div}_y e(y) \cdot E_E(\bar{x}), \tag{60}$$

$$\mathrm{div}_y \left[e(y) \cdot \mathrm{sym} \nabla_y u_1(\bar{x}, y) + \varepsilon(y) \cdot \nabla_y \Phi_1(\bar{x}, y) \right] = -\mathrm{div}_y \varepsilon(y) \cdot S_E(\bar{x}) + \\ + \mathrm{div}_y \varepsilon(y) \cdot E_E(\bar{x}). \tag{61}$$

In keeping with equations (62), (63), the following auxiliary tensors **A(y), B(y), G(y), H(y)**, which mutually link $u_1(x, y)$, $\Phi_1(x, y)$ with $S_E(\mathrm{x})$, $E_E(x)$, are then derived:

$$u_1(\bar{x}, y) = \mathbf{A(y)} \cdot S_E(\bar{x}) + \mathbf{B(y)} \cdot E_E(\bar{x}), \tag{62}$$

$$\Phi_1(\bar{x}, y) = \mathbf{G(y)} \cdot S_E(\bar{x}) + \mathbf{H(y)} \cdot E_E(\bar{x}). \tag{63}$$

From equations (60), (61), (62), (63), the system of equations (64) – (67) is obtained, the solution of which are the values of the auxiliary quantities of the tensors **A(y), B(y), G(y), H(y)**:

$$\operatorname{div}_y\left[c(y)\cdot \operatorname{sym}\nabla_y \mathbf{A}(\mathbf{y}) - e(y)\cdot \nabla_y \mathbf{G}(\mathbf{y})\right] = -\operatorname{div}_y c(y), \tag{64}$$

$$\operatorname{div}_y\left[e(y)\cdot \operatorname{sym}\nabla_y \mathbf{A}(\mathbf{y}) + \varepsilon(y)\cdot \nabla_y \mathbf{G}(\mathbf{y})\right] = -\operatorname{div}_y e(y), \tag{65}$$

$$\operatorname{div}_y\left[c(y)\cdot \operatorname{sym}\nabla_y \mathbf{B}(\mathbf{y}) - e(y)\cdot \nabla_y \mathbf{H}(\mathbf{y})\right] = -\operatorname{div}_y e(y), \tag{66}$$

$$\operatorname{div}_y\left[e(y)\cdot \operatorname{sym}\nabla_y \mathbf{B}(\mathbf{y}) + \varepsilon(y)\cdot \nabla_y \mathbf{H}(\mathbf{y})\right] = -\operatorname{div}_y \varepsilon(y). \tag{67}$$

The system of equations (64)–(67) can be expressed using the tensor notation (68)–(71):

$$\left[c_{ijkl}\,\mathbf{A}^{pq}_{k,l} - e_{kij}\,\mathbf{G}^{pq}_{,k}\right]_{,j} = -c_{ijpq,j}, \tag{68}$$

$$\left[e_{ikl}\,\mathbf{A}^{pq}_{k,l} + \varepsilon_{ik}\,\mathbf{G}^{pq}_{,k}\right]_{,i} = -e_{ipq,i}, \tag{69}$$

$$\left[c_{ijkl}\,\mathbf{B}^{p}_{k,l} - e_{kij}\mathbf{H}^{p}_{,k}\right]_{,j} = e_{pij,j}, \tag{70}$$

$$\left[e_{ikl}\,\mathbf{B}^{p}_{k,l} + \varepsilon_{ik}\mathbf{H}^{pq}_{,k}\right]_{,i} = -e_{ip,i}. \tag{71}$$

Equations (64)–(67) and (68)–(71) are static equations (Fig. 3) with generalized excitations in the form of generalized forces (72)–(73) and generalized charges (74)–(75) as well as generalized inputs in the form of generalized forces (76)–(77) and generalized charges (78)–(79) shown below.

The generalized excitations in terms of generalized forces (72)–(73) are:

$$\overline{\mathbf{T}}^{kl}_{ij} = c_{ijpq}\mathbf{A}^{kl}_{p,q} - e_{pij}\mathbf{G}^{kl}_{,p}, \tag{72}$$

$$\overline{\mathbf{T}}^{k}_{ij} = c_{ijpq}\mathbf{B}^{k}_{p,q} - e_{pij}\mathbf{H}^{k}_{,p}. \tag{73}$$

The generalized response expressed in context of generalized charges (74)–(75) are:

$$\overline{\mathbf{D}}^{ij}_{k} = e_{kpq}\mathbf{A}^{ij}_{p,q} + \varepsilon_{kp}\mathbf{G}^{ij}_{,p}, \tag{74}$$

$$\overline{\mathbf{D}}^{j}_{i} = e_{ipq}\mathbf{B}^{j}_{p,q} + \varepsilon_{ip}\mathbf{H}^{j}_{,p}. \tag{75}$$

The generalized inputs in the form of generalized forces (76)–(77) are as follows: where $\mathbf{n}_j = \{n_1, n_2, n_3\}$ is the vector of the external normal vector.

$$(\mathbf{F})_i^{pq} \equiv \left[|c_{ijpq}| \right] \cdot \mathbf{n}_j, \tag{76}$$

$$(\mathbf{F})_i^{p} \equiv \left[|e_{pij}| \right] \cdot \mathbf{n}_j, \tag{77}$$

The generalized inputs in the form of generalized charges (78)–(79) are:

$$(\mathbf{Q})^{pq} \equiv \left[|e_{ipq}| \right] \cdot \mathbf{n}_i, \tag{78}$$

$$(\mathbf{Q})^{pq} \equiv \left[|\varepsilon_{ipq}| \right] \cdot \mathbf{n}_i. \tag{79}$$

The static problem formulated in the form of the equation of statics (68)–(71) is illustrated in Fig. 4. For the system of equations (68)–(71), predetermined loads on the boundaries of material phases on the volume of the symmetry element Y of the composite solid were determined in the form of generalized forces (76)–(77) and generalized charges (78)–(79) which are induced by a step-like change in the values of the material tensors on the boundaries of the phases in the volume of the aforementioned element Y (Fig. 3). The boundary conditions mentioned above are reflected in the form of the right-hand side of the system of equations (64)–(67) and (68)–(71).

The mechanical rigidity matrices for piezoceramics and polymers have the form:

PIEZOCERAMICS

$$\begin{bmatrix} c_{1111} & c_{1122} & c_{1133} & 0 & 0 & 0 \\ . & c_{1111} & c_{1133} & 0 & 0 & 0 \\ . & . & c_{3333} & 0 & 0 & 0 \\ . & . & . & c_{2323} & 0 & 0 \\ . & \text{symmetry} & . & . & c_{2323} & 0 \\ . & . & . & . & . & c_{1212} \end{bmatrix}$$

POLYMERS

$$\begin{bmatrix} c_{1111} & c_{1122} & c_{1122} & 0 & 0 & 0 \\ . & c_{1111} & c_{1122} & 0 & 0 & 0 \\ . & . & c_{2222} & 0 & 0 & 0 \\ . & . & . & c_{2222} & 0 & 0 \\ . & \text{symmetry} & . & . & c_{2222} & 0 \\ . & . & . & . & . & c_{1212} \end{bmatrix}$$

The dielectric rigidity matrices for piezoceramics and polymers:

PIEZOCERAMICS

$$\begin{bmatrix} \varepsilon_{11} & 0 & 0 \\ . & \varepsilon_{11} & 0 \\ \text{symmetry} & . & \varepsilon_{33} \end{bmatrix}$$

POLYMERS

$$\begin{bmatrix} \varepsilon_{11} & 0 & 0 \\ . & \varepsilon_{11} & 0 \\ \text{symmetry} & . & \varepsilon_{11} \end{bmatrix}.$$

The piezoelectric rigidity matrices for piezoceramics and polymers:

PIEZOCERAMICS

$$\begin{bmatrix} 0 & 0 & e_{311} \\ 0 & 0 & e_{311} \\ 0 & 0 & e_{333} \\ 0 & e_{223} & 0 \\ e_{223} & 0 & 0 \\ 0 & 0 & 0 \end{bmatrix}.$$

In view of the form of the material tensors c_{ijkl}, e_{kij}, ε_{ik} for polarized piezoceramics (orthotropic material) and polymers (isotropic properties), most terms in the matrix representation of the aforementioned tensors beyond the main diagonal are zero in value. Equations (80)–(82) show the proposed form of the formula for the effective calculation of the values of the material tensors c^{EF}, e^{EF}, ε^{EF} for the substitute homogeneous piezoelectric material.

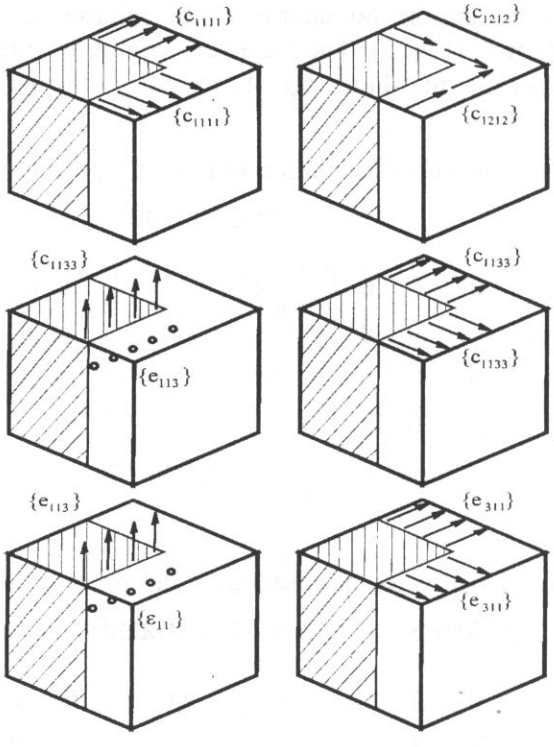

Fig. 5. Six elementary static related to the load of the elementary symmetry unit of the composite caused by a step-like change in the value of the material tensors at the boundaries of material phases.

$$c_{ijkl}^{EF} = \|c_{ijkl}\|_Y + \|\overline{\mathbf{T}}_{ij}^{kl}\|_Y, \tag{80}$$

$$\varepsilon_{ij}^{EF} = \|\varepsilon_{ij}\|_Y + \|\overline{\mathbf{D}}_i^j\|_Y, \tag{81}$$

$$e_{ijk}^{EF} = \|e_{ijk}\|_Y + \|\overline{\mathbf{T}}_{ij}^{p}\|_Y = -\|e_{ijk}\|_Y + \|\overline{\mathbf{D}}_k^{ij}\|_Y. \tag{82}$$

In equations (80)–(82), two terms were separated on the right-hand side of each equation. The first is related to the weighted average of the value of the material tensors of the composite components on the volume of the solid of the elementary cell. The other illustrates, in turn, the impact of the step-like discontinuity of the value of the aforementioned tensors on the volume of the solid in question.

In keeping with equations (76)–(79), the static analysis shown in Fig. 4 is reduced to the solution of six independent static problems with load cases presented in Fig. 5.

On the basis of (80)–(82), calculations of the values of the components of the tensors were made and they are listed in Table 1.

Table 1. Calculations of the values of the components of the material tensors of piezoceramics, an epoxy resin and the composite made from two afromentioned materials.

		Piezoceramics	Epoxy resin	Composite subject homogenization
c_{11}	$kg/(m*s^2)$	$12.1*10^{10}$	$7.4*10^{10}$	$3.09*10^{10}$
c_{12}	$kg/(m*s^2)$	$7.5*10^{10}$	$1.4*10^{10}$	$1.65*10^{10}$
c_{13}	$kg/(m*s^2)$	$7.7*10^{10}$	$1.4*10^{10}$	$1.63*10^{10}$
c_{33}	$kg/(m*s^2)$	$7.3*10^{10}$	$7.4*10^{10}$	$2.91*10^{10}$
c_{44}	$kg/(m*s^2)$	$2.1*10^{10}$	$4.7*10^{10}$	$9.09*10^{10}$
c_{66}	$kg/(m*s^2)$	$2.3*10^{10}$	$4.7*10^{10}$	$8.49*10^{10}$
ε_{11}	$A^2*s^4/kg*m^3$	$14.6*10^{-9}$	$3.53*10^{-11}$	$1.08*10^{-9}$
ε_{33}	$A^2*s^4/kg*m^3$	$15*10^{-9}$	$3.53*10^{-11}$	$1.48*10^{-9}$
e_{31}	$A*s/m^2$	-5.4	0	-1.66
e_{33}	$A*s/m^2$	15.1	0	3.19
e_{15}	$A*s/m^2$	12.3	0	2.60

3. Dynamic analysis of the electromechanical coupling coefficient

The values of the electromechanical coupling coefficient k are calculated using a numerical dynamic analysis involving direct integration within the framework of the finite element method:

$$k = \frac{E_m}{\sqrt{E_{st}E_d}} \tag{83}$$

$$E_m = \frac{1}{4}\left(u^t K_{u\Phi}\Phi + \Phi_t K_{u\Phi}^t u\right), \tag{84}$$

$$E_{st} = \frac{1}{2} u^t K_{uu} u, \tag{85}$$

$$E_d = \frac{1}{2} \Phi^t K_{\Phi\Phi}\Phi, \tag{86}$$

where E_m is the electromechanical energy, E_{st} is the energy of the field of strains and stresses, E_d is the electric field energy, u is the displacement matrix, Φ is the potential matrix, K_{uu} is the mechanical matrix rigidity, $K_{\Phi\Phi}$ is the dielectric rigidity matrix and K^t is the matrix transposed with respect to the matrix K.

The values of the electromechanical coupling coefficient k were calculated from formula (98) for the composite transducer (Fig. 1) and the PZT transcuder with the same electrical resonance frequency and disk diameter. The results are listed in Table 2.

Table 2. Values of the electromechanical coupling coefficient k for the piezoceramic and composite transducers previously subjected to homogenization.

Transducer type	Electrical resonance frequency MHz	Electromechanical coupling coefficient k
Piezoceramics	1.80	0.48
Composite previously subjected to homogenization	1.86	0.69

4. Conclusions

The approximation of the values of the effective material tensors of hypothetical homogeneous material only by weighted averages of its components involves the error related to neglecting the impact of a step-like change (in the case of the type 1-3 composite) in the physical properties at the boundaries of the material phases in the volume of the elementary symmetry unit of the composite. The division of the numerical calculations into two independent stages (static and dynamic analyses) makes it possible to carry them out for the whole composite solid, since in this way the limitation imposed by the permissible order of the global rigidity matrix of the problem is bypassed. The

calculations confirmed an approximately 50% increase in the value of the electromechanical coupling coefficient of the composite with respect to the piezoceramics.

References

[1] W. SMITH, *New Device in Ultrasonic Transducers*, The International Society for Optical Engineering, Bellingham, USA, State Washington, 1992, Vol. 1733, pp.3-26.

[2] T. D. HIEN, *Deterministic and stochastic sensitivity in computational structural mechanics*, Institute of Fundamental Technological Research Reports, Warsaw, Poland, 1990, vol. 46, pp. 18-20.

[3] J. J. TELEGA, *Piezoelectricity and Homogenisation*, Application to Biomechanics, Continuum Models and Discrete Systems, [Ed.] G. A. Maugin, vo. 2, pp. 220-229, Longman, Essex, 1991.

[4] A. GAŁKA, J. J. TELEGA, and R. WOJNAR, *Homogenisation and Thermopiezoelectricity*, Mech. Res. Comm., **19**, pp. 315-324, 1991.

[5] A. BENSOUSSAN, J. LIONS, G. PAPANICOLAOU, *Asymptotic analysis for periodic structures*, North-Holland, Amsterdam, 1978.

[6] E. SANCHEZ-PALENCIA, *Non homogeneous media and vibration theory*, Springer, Berlin, 1980.

ARCHIVES OF ACOUSTICS
21, 4, 387–398 (1996)

SURFACE ACOUSTIC WAVE DESIGN FUNDAMENTALS

D.C. MALOCHA

Electrical and Computer Engineering Dept.
University of Central Florida
(Orlando, FL 32816-2450, USA)

This paper will provide a fundamental approach to the design of SAW transducers and filters. Although SAW devices are often modeled with complex and large programs, the basic design principles can be analyzed with simple programs and commercially available analysis tools, such as Mathcad or Matlab. The beginning of the paper reviews the basis for the impulse response model. Design equations for fundamental window time functions as applied to apodized transducers will be presented. The development shows an analytical approach to the solution of apodized transducers. The solutions provide the SAW radiating beam profile as a function of frequency as well as the frequency dependent acoustic transducer parameters. The electrical network effects on the overall transducer response are presented which provides a complete first order analysis for fundamental SAW trandsucer design.

1. Introduction

This paper will discuss a fundamental approach to simple but important SAW transducer designs which illustrate the principles in the design process. The principles of finite impulse response design, are not presented in this work. The focus will be on a single transducer design. In it's simplest form, a SAW filter is composed of two transducers which may have different center frequencies, bandwidths, and other filter specifications. The product of two frequency responses produces the total filter response.

The four most popular and widely used SAW models include the transmission line model, the coupling of modes model, the impulse response model, and the superposition model. The superposition model is an extension of the impulse response model and is the principle model used for the majority of SAW bi-directional and multiphase filter synthesis which do not have inband, inter electrode reflections because of its simplicity and ease of understanding. This paper will use the simple impulse response model to illustrate fundamental SAW design principles.

2. The SAW impulse response transducer model

The basic SAW impulse response model can be derived by using energy arguments. To first order, the acoustic impulse response under the transducers is assumed to be sinusoidal having the electrode period as shown in Figure 1. This assumption ignores the actual charge distribution under the electrodes which is proportional to the actual SAW waveform, but yields a good approximation to the fundamental SAW frequency response. First, the single electrode center frequency conductance can be found using energy arguments [1]. The following variables are defined as:

C_s' capacitance per electrode per unit beam width,
W_a acoustic beam width,
E_e stored electric energy,
ΔE_e change in the stored electric energy,
E_a acoustic energy in a single half wavelength,
ΔE_a change in the stored acoustic energy in a single half wavelength,
ΔP_a change in the acoustic power.

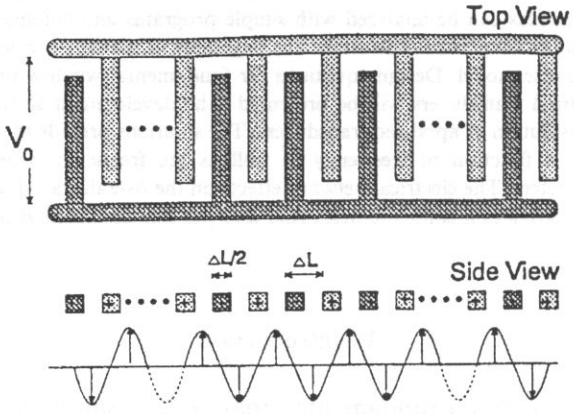

Fig. 1. Schematic representation of a SAW IDT and the fundamental wave perturbation under the electrode pattern when driven by an impulse.

As energy is absorbed acoustically, the electric energy must be decreasing. Then, assuming no losses, $\Delta E_a = -\Delta E_e$ and $\Delta P_a = -\Delta E_e/\Delta t$. Energy will be coupled electro-acoustically to the wave, given by

$$k^2 E_e = \frac{1}{2}\Delta E_a = -\frac{1}{2}\Delta E_e, \tag{2.1}$$

where k^2 is defined as the acousto-electric coupling coefficient to the wave. The one-half in accounts for the fact that there is both a forward and reverse traveling wave, each containing equal energy. The electric energy transferred to the SAW each half wavelength is

$$E_e = C_s' W_a V_0^2, \tag{2.2}$$

where $C_s' W_a$ is the single electrode transducer capacitance and V_0 is the potential. Assuming no losses and equal static and kinetic energy, the change in acoustic power at center frequency is given by

$$\Delta P_a = -\Delta E_e / \Delta t = 4 f_0 k^2 C_s' W_a V_0^2, \tag{2.3}$$

where $\Delta t = 1/2f_0$ is the period of one-half wavelength and $v_a \Delta t = \Delta L$. From the power relationship, the acoustic conductance per one-half wavelength is given by

$$G_o = \Delta P_a / V_0^2 = 4k^2 f_0 C_s' W_a, \tag{2.4}$$

where C_s' is the capacitance per electrode. Equation (2.4) is the synchronous (or center frequency) acoustic conductance for a single half wavelength (or single electrode) for the transducer.

For a linear causal system, the inverse Fourier transform of the device's frequency response is the device time impulse response. The SAW impulse response for an uniform beam transducer with arbitrary electrode spacing can be written as

$$h(t) = A_0 \cos[\theta(t)] \operatorname{rect}(t/r) \qquad \text{where } \theta(t) = 2\pi \int_0^t f_i(\tau) d\tau \tag{2.5}$$

and where $f_i(t)$ equals the instantaneous frequency at a time, t, and A_0 equals a constant. For a uniform beam transducer with periodic electrode spacing, $f_i(t) = f_0$ and $\cos\theta(t) = \cos\omega_0 t$.

Given the form of the time response, energy arguments are used to determine the device equivalent circuit parameters for a transducer of arbitrary length. Assume a delta function voltage input, $v_0(t) = \delta(t)$, then $V_0(\omega) = 1$. Given $h(t)$, $H(\omega)$ is known and the energy launched as a function of frequency is given by $E(\omega) = 2 \cdot |H(\omega)|^2$ [2]. Then

$$E(\omega) = V_0^2(\omega) \cdot G_a(\omega) = 1 \cdot G_a(\omega), \tag{2.6}$$

or

$$G_a(\omega) = 2 \cdot |H(\omega)|^2. \tag{2.7}$$

There is a direct relationship between the transducer frequency transfer function and the transducer conductance. Consider an IDT with uniform overlap electrodes having N_p interaction pairs. Each gap between alternating polarity electrodes is considered a localized SAW source. The SAW impulse response at the fundamental frequency will be continuous and of duration τ, where $\tau = N \cdot \Delta t$, and $h(t)$ is given by

$$h(t) = A_0 \cdot \cos(\omega_0 t) \cdot \operatorname{rect}(t/r), \tag{2.8}$$

where ω_0 is the carrier frequency, in radians per second.

The corresponding frequency response is given by

$$H(\omega) = \frac{A_0 \tau}{2} \left\{ \frac{\sin(x_1)}{x_1} + \frac{\sin(x_2)}{x_2} \right\}, \tag{2.9}$$

where $x_1 = (\omega - \omega_0) \cdot \tau/2$ and $x_2 = (\omega + \omega_0) \cdot \tau/2$.

The ideal SAW continuous response in both time and frequency is now known. This can be related to the sampled response by a few substitutions of variables, let

$$\Delta t = \frac{1}{2 \cdot f_0} \qquad t_n = n \cdot \Delta t \qquad N \cdot \Delta t = \tau \qquad N_p \cdot \Delta t = \tau/2, \tag{2.10}$$

where N is the total number of electrodes (or half wavelengths) and N_p is the total number of electrode pairs. Assuming a frequency bandlimited response, the negative frequency component centered around $-f_0$ can be ignored. Then the frequency response, using (2.9) is given by

$$H(\omega) = A_0 \left\{ \frac{N}{4 f_0} \right\} \cdot \frac{\sin(x_n)}{x_n}, \tag{2.11}$$

where $x_n = \dfrac{(\omega - \omega_0)}{\omega_0} \pi N_p$. The conductance, given using (2.7) and (2.9), is

$$G_a(f) = \frac{A_0^2}{8} \left\{ \frac{N}{f_0} \right\}^2 \cdot \frac{\sin^2(x_n)}{x_n^2} = \frac{A_0^2}{2} \left\{ \frac{N_p}{f_0} \right\}^2 \cdot \frac{\sin^2(x_n)}{x_n^2}. \tag{2.12}$$

A_0 can be found solving (2.12) using (2.4) at center frequency and with $N = 1$. Then

$$A = (32 k^2 f_0^3 C_s' W_a)^{1/2} \qquad \text{for } N = 1, \tag{2.13}$$

and

$$A_N [(32 k^2 f_0^3 C_s' W_a N^2)^{1/2}, \qquad \text{for all } N, \tag{2.14}$$

where A_N represents the peak wave amplitude under the transducer for N electrodes. It is typical to define the wave amplitude per wavelength (or electrode pair), given as

$$A_{Np} = (4 k^2 f_0^3 C_s W_a N_p^2)^{1/2}, \tag{2.15}$$

where the electrode pair capacitance is $C_s = 2C_s'$. The peak wave amplitude is proportional to the number of electrodes (or impulse length) at the synchronous center frequency. The energy within the confines of the transducer area is given as $E = A_{N_p}^2$. The energy exiting the transducer from either end is $\frac{1}{2} E$, therefore, the peak wave amplitude for either the forward or reverse traveling wave is $A_{N_p} \sqrt{2}$.

The center frequency conductance is given from (2.12) as

$$G_a(f_0) = G_0 = 8 k^2 f_0 C_s W_a N_p^2 \tag{2.16}$$

or the frequency dependent transducer conductance is

$$G_a(f_0) = G_0 \cdot \frac{\sin^2(x_n)}{x_n^2}. \tag{2.17}$$

The transducer electrode capacitance is given as

$$C_e = C_s W_a N_p . \tag{2.18}$$

Finally, the last term of the SAW transducer's equivalent circuit is the frequency dependent susceptance. Given any system where the frequency dependent real part is known, there is an associated imaginary part which must exist for the system to be real and causal. This is given by the Hilbert transform susceptance, defined as B_a, where [3]

$$B_a(\omega) = \frac{1}{\pi} \int_{-\infty}^{\infty} \frac{G_a(u)}{(u-\omega)} du = G_a(\omega) * 1/\pi\omega , \tag{2.19}$$

where "*" indicates convolution.

The simple impulse model treats each electrode as an ideal impulse, however, the electrodes have a finite width which distorts the ideal impulse response. The actual SAW potential has been shown to be closely related to the electrostatic charge induced on the transducer by the input voltage and the details will not be presented here [4].

3. Apodized SAW transducers

Apodization is the most widely used method for weighting a SAW transducer, as depicted in Figure 2. The desired time sampled impulse response is implemented by assigning the overlap of opposite polarity electrodes at a given position to a normalized sample weight at a given time. Typical computer analysis divides the acoustic beam into a number of parallel tracks where the impulse response can be represented, to any required accuracy, as the summation of uniform samples located at the proper positions in time in a given track. Mathematically this is given by

$$h(t) = \sum_{i=1}^{I} h_i(t) , \tag{3.1}$$

and

$$H(\omega) = \sum_{i=1}^{I} H_i(\omega) = \sum_{i=1}^{I} \left\{ \int_{-\tau/2}^{\tau/2} h_i(t) e^{-j\omega t} dt \right\} . \tag{3.2}$$

Although this approach is general, exact analytical solutions are obtainable for some important types of simple functions which provide insight into the spatial distribution of the energy in an apodized transducer acoustic beam.

A mapping can be obtained from time to space for some simple but useful time functions. For illustration, let's assume a cosine envelope time function given by

$$h(t) = A \cdot \cos(\pi t/\tau) \cos(\omega_0 t) \operatorname{rect}(t/\tau)) .$$

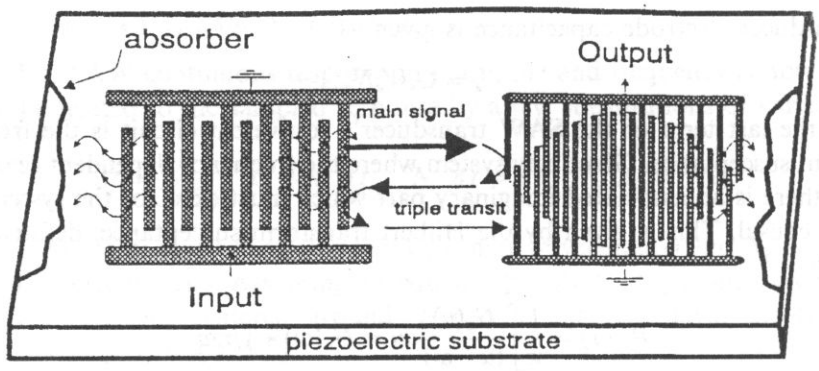

Fig. 2. Schematic diagram of a typical SAW filter composed of one unweighted interdigital transducer (IDT) and an apodized transducer.

Defining the y-direction as the propagation direction and the x-direction as transverse to the propagation direction, then a mapping can be made between the functional description and the time impulse response lenght as a function of x which describes $h(t, x)$. Looking at the apodization pattern at each point in x shows that the impulse response length is centered at time $t = 0$ and the time response is

$$h(t, x) = A \cdot \cos(\omega_0 t) \cdot \mathrm{rect}(t/\tau_1(x)),$$

where $\tau_1(x)$ is the impulse response lenght at each point in x.

The impulse response length as a function of x is given as

$$\tau_i(x) = \frac{2 \cdot \tau}{\pi} \cdot \mathrm{arc\ cos}\left(\frac{2 \cdot |x|}{W_a}\right).$$

The form of the solution has the familiar Fourier transform

$$H(x, f) = \frac{A \cdot \tau_1(x)}{2} \cdot \left\{ \frac{\sin[y_1(x, f)]}{y_1(x, f)} + \frac{\mathrm{sin} y_2(x, f)]}{y_2(x, f)} \right\},$$

where

$$y_1(x, f) = \frac{f - f_0}{f_0} 2\pi f_0 \frac{\tau_1(x)}{2} \quad \text{and} \quad y_2(x, f) = \frac{f + f_0}{f_0} 2\pi f_0 \frac{\tau_1(x)}{2}.$$

This yields the spatially dependent frequency response which allows the amplitude profile emerging from the transducer to be plotted. The amplitude profile spatially varies and is dependent on the frequency of interest as well as the fractional bandwidth. The overall frequency response is given by

$$H(f) = A \cdot \int_{-Wa/2}^{Wa/2} H(x, f)\, dx.$$

Figure 3 shows the transducer frequency response and the amplitude beam profile for several frequencies. As another example, an inverse cosine time function is given by

$$h(t) = \frac{2 \cdot A}{\pi} \cdot \arccos(2|t|/\tau)\cos(\omega_0 t)\,\mathrm{rect}(t/\tau).$$

and the spatially dependent time function is given as

$$h(t, x) = \arccos(\omega_0 t)\,\mathrm{rect}\,(t/\tau_2(x)] \quad \text{where} \quad \tau_2(x) = \frac{\tau}{2} \cdot \cos(\pi x/Wa).$$

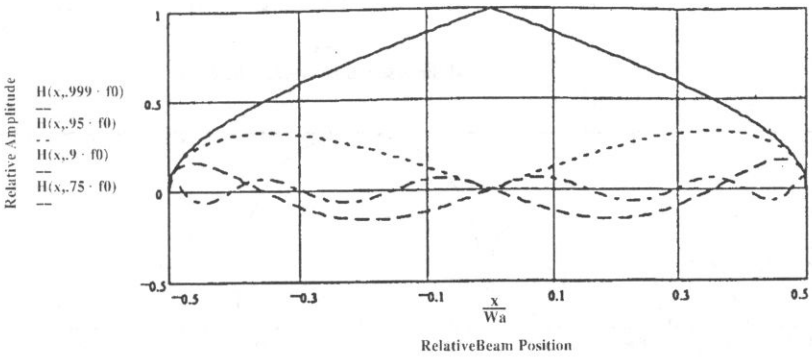

a) Cosine Window Function

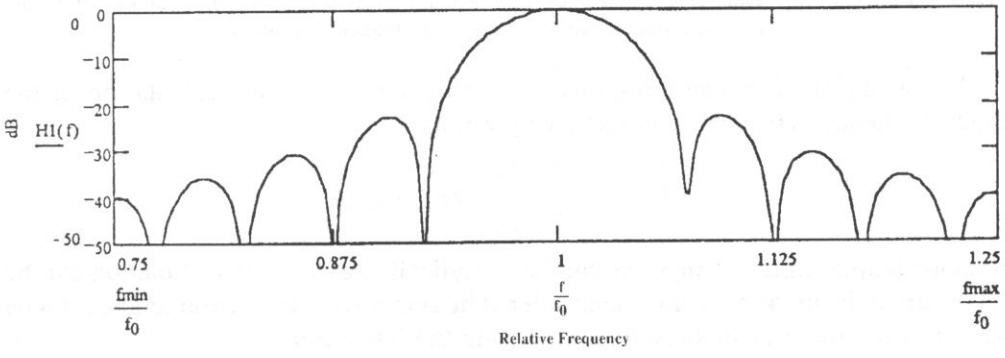

b) Frequency Response

Fig. 3. Calculated SAW beam profile and frequency response for cosine envelope time function. a) Cosine window function; b) Frequency response.

The spatially dependent amplitude response as a function of frequency is shown in Figure 4. Notice that the amplitude profile is much smoother at the beam center than for the cosine envelope time function. The inverse cosine time function is often used in resonator structures because of its smoother amplitude beam profile and maximum energy confinement to the beam center. This analysis is also useful if examining transverse mode coupling in a waveguide.

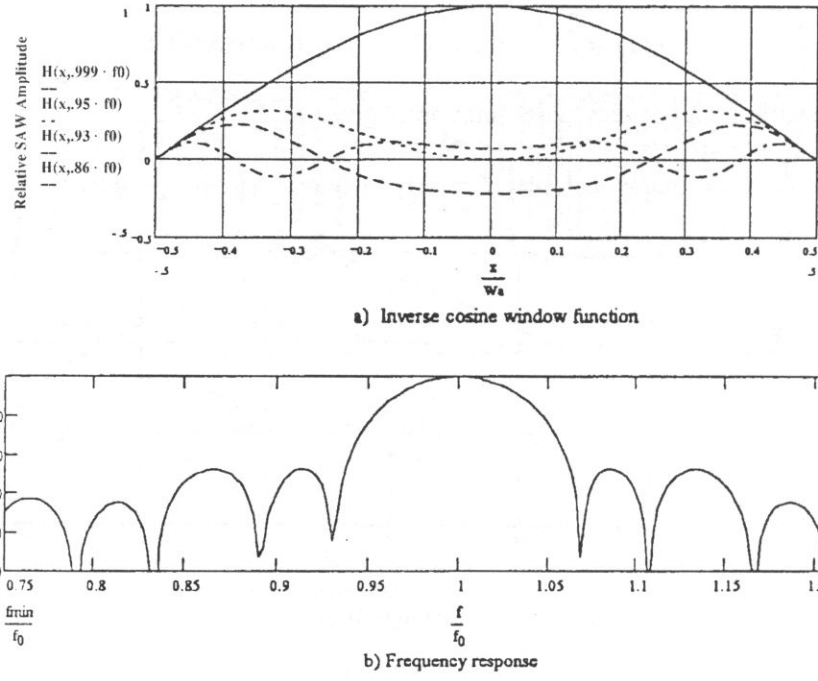

Fig. 4. Calculated SAW beam profile and frequency response for inverse cosine envelope time function. a) Inverse cosine window function; b) Frequency response.

Knowning the frequency response as a function of x allows calculation of the exact frequency dependent conductance given as

$$G_a(f) = 2\int_{-Wa/2}^{Wa2/2} |H(f, x)|^2 dx .$$

Because simple window functions can be analytically described, this function can be sloved analytically or by using a computer. The center frequency conductance can be written using the previous results and sloving the integral as

$$G_a(f_0) = 8k^2 f_0 C_s W_a N_{\text{eff}}^2 .$$

N_{eff} is a function of the impulse response lenght and the form of the time function. For the transverse cosine time function $N_{\text{eff}} = \dfrac{N_p}{\sqrt{2}}$ and for the cosine time envelope $N_{\text{eff}} = .68 * N_p$. The plot of the conductance and frequency response are given in Figure 5. Note that there is energy radiated even at the nulls of the frequency response due to the apodization effect.

There is also a secondary effect of apodization when attempting to extract energy. Not all of the power of a non-uniform SAW beam can be extracted by an a uniform transducer, and reciprocally, not all of the energy of a uniform SAW

beam can be extracted by an apodized transducer. The transducer efficiency is calculated at center frequency for an analytic function as

$$E = \frac{\left| \int_{-Wa/2}^{Wa/2} H(f_0, x)\,dx \right|^2}{Wa \int_{-Wa/2}^{Wa/2} |H(f_0, x)|^2\,dx}$$

and the apodization loss is defined as: apodization loss $= 10 \cdot \log(E)$. For the transverse cosine function the apodization loss is .921 dB and for the cosine time function the apodization loss is .571 dB.

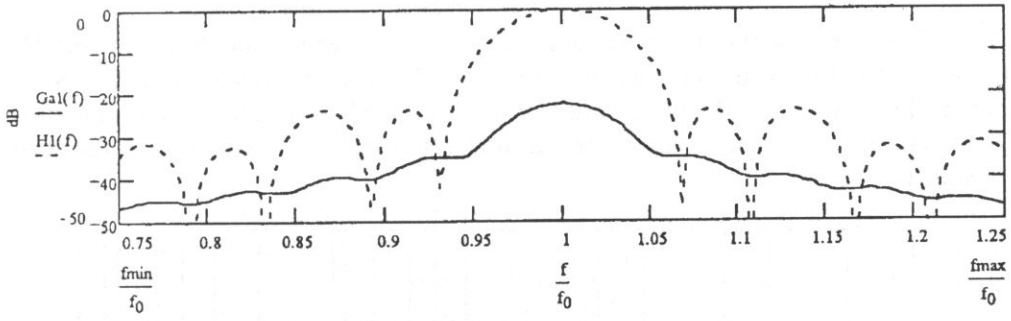

Fig. 5. Plots of the calculated frequency response and acoustic conductance for an apodized inverse cosine time function. The center frequency-impulse responde lenght product equals 20.

4. Electrical network effects

Given the acoustic conductance and Hilbert transform susceptance, and the transducer static capacitance, the SAW transducer equivalent circuit is known, shown in Figure 6, and the electrical network effects can be determined. Define the transducer Q and the load Q, respectively, as

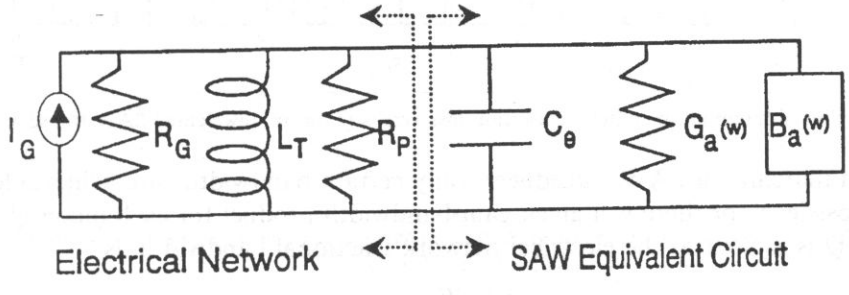

Fig. 6. SAW equivalent circuit model which includes the generator, parasitic resistance, and a tuning inductor.

$$Q_r = \frac{\omega_0 C_3 Wa}{Ga(f_0)} \quad \text{and} \quad Q_g = \frac{\omega_0 C_3 Wa}{G_g},$$

where C_g is the generator conductance. Then the center frequency transducer gain can be written as

$$G_T = \frac{4Q_g/Q_r}{(1+Q_g/Q_r)^2+Q_g^2}.$$

The minimum unmatched insertion loss can be found for a given transducer Q with a certain generator Q by taking the derivative of G_T and setting it to zero which yields.

$$Q_G = \sqrt{\left[\frac{Q_r^2}{1+Q_r^2}\right]}.$$

Figure 7 is a plot of the minimum unmatched transducer mismatch loss versus Q_r. To obtain the lowest unmatched insertion loss, for low Q transducers it is best to match the real part of the transducer to the load resistance while for high Q transducers it is best to match the transducer's reactive impedance to the load resistance.

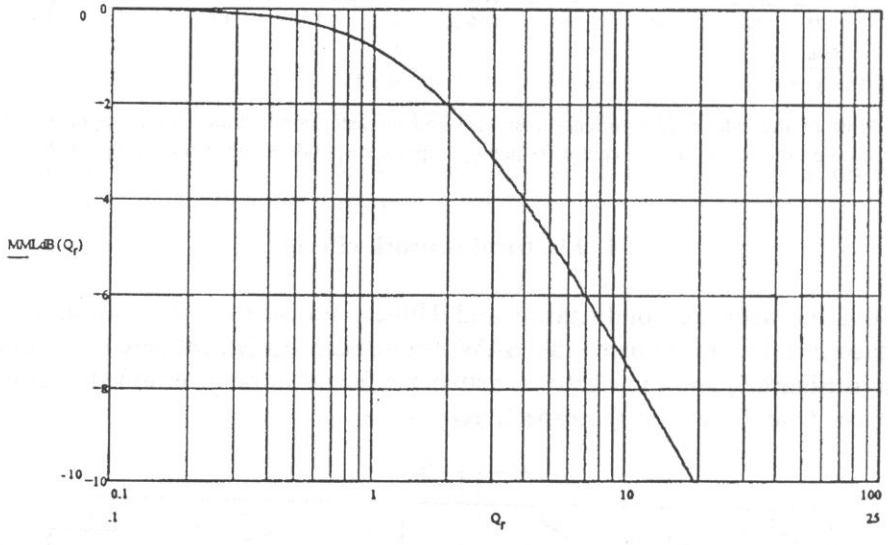

Fig. 7. Plot of minimum unmatched insertion loss versus Q for an unweighted SAW transducer.

When matching a SAW transducer, only certain bandwidths are achievable for a given loss level, or there is a given gain-bandwidth product for each material. The network Q is related to the electrical network fractional bandwidth as

$$Q_r = \frac{\omega_0 C_3 Wa}{2 \cdot Ga(f_0)} = f_0/\Delta f_e.$$

For minimum electrical distortion it is usually assumed that the electrical fractional bandwidth is twice the acoustical bandwidth, or $\Delta f_e = 2\Delta f$. Then back substituting from the previous equations and assuming a uniform weighted IDT, yields

$$\frac{\omega_0 C_3 Wa}{2 \cdot Ga(f_0)} = \frac{\pi/8k^2}{N_p} = \frac{f_0}{2\Delta f} \quad \text{or} \quad \{\Delta f/f_0\}_{\max} \leq \sqrt{4k^2/\pi}\,.$$

If the fractional bandwidth is larger than given above, then the transducer insertion loss increases at a rate of 6 dB per octave.

The effects of the electrical network can be demonstrated by assuming a simple parallel matching inductor, and no parasitic resistance. It will be assumed that the transducer can be exactly matched to the real load impedance. The transfer function, ignoring the Hilbert transform susceptance can be written as

$$H_e(\omega) = \frac{G_g/\omega_0 C_e}{\dfrac{\beta G_a(f_0)}{\omega_0 C_e} + \dfrac{G_a(f)}{G_a(f_0)} + \left[\dfrac{\omega}{\omega_0} - \dfrac{\omega_0}{\omega}\right]}, \quad \text{where } \beta = G_g/G_a(f_0)\,.$$

Figure 8 shows a series of plots of the effects of the electrical network transfer function as a function of Q. At center frequency, half the voltage is on the SAW conductance, which corresponds to the -6 dB level. Off center frequency, the voltage increases which causes a loss in sidelobe rejection.

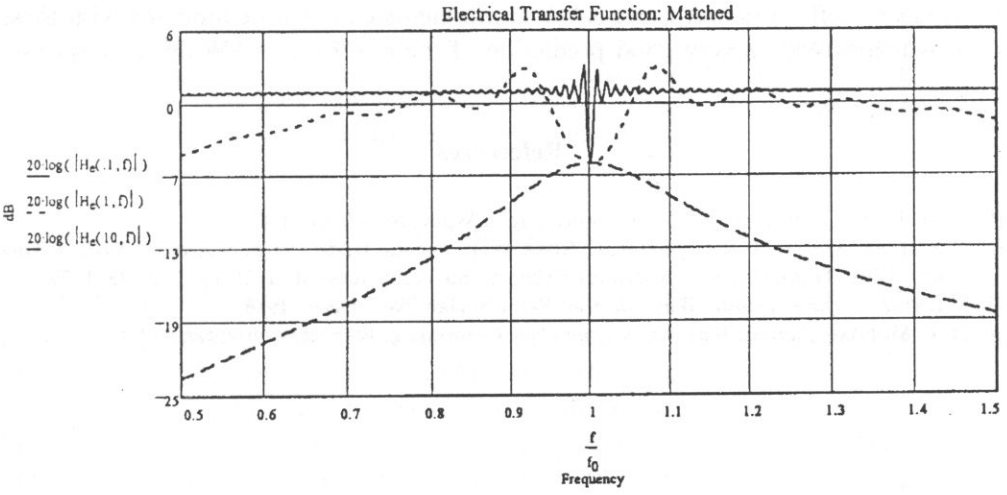

Fig. 8. Electrical network transfer function versus frequency for SAW transducer Q_s of 0.1, 1, 10, respectively, for $\beta = 1$.

The effect on the overall filter response is shown in Fig. 9, which shows a degradation in the sidelobe levels and a slight distortion of the bandwidth.

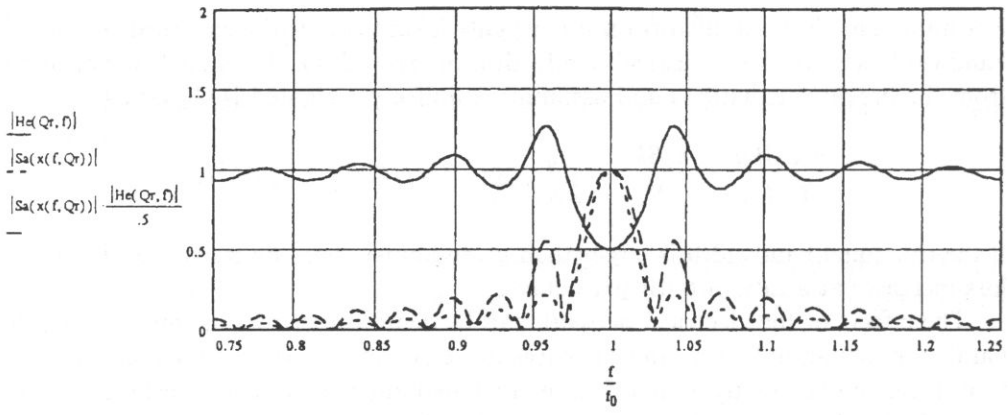

Fig. 9. The effects of the electrical network for a SAW transducer with a Q of 0.5. The solid line is the voltage transfer function, the dotted line is the ideal $\sin x / x$ response and the dashed line is the product response.

5. Conclusion

This paper has presented a simple approach to the first order design of SAW filters, including the apodization effect. All of the figures and plots were obtained using Mathcad, which is a very affordable tool for accomplishing first order analysis of elementary SAW transducers. More complicated structures, such as multiphase transducers, reflectors and other SAW components can also be modeled with these tools which provide a very good prediction of the first order SAW device response.

References

[1] V. M. RISTIC, *Principles of Acoustic Devices*, John Wiley, New York, 1983.

[2] C. S. HARTMANN, D. T. BELL, and R. C. ROSENFELD, *Impulse Model Design of Acoustic Surface Wave Filters*, IEEE Transactions on Microwave Theory and Techniques, MTT-21, pp. 162-175, 1979.

[3] S. DATTA, *Surface Acoustic Wave Devices*, Prentice Hall, New Jersey, 1986.

[4] D. P. MORGAN, *Surface Wave Devices for Signal Processing*, Elsevier, Amsterdam, 1991.

ARCHIVES OF ACOUSTICS
21, 4, 399–412 (1996)

STUDY OF DISCONTINUITIES LOCALIZATION IN ROCK USING ACOUSTIC EMISSION

M. CH. REYMOND

Unité Mixte Centre National de la Recherche Scientifique
Laboratoire Central des Ponts et Chaussées
(2 Allée Kepler, 77420 Champs sur Marne, France)

A. JAROSZEWSKA

Institute of Fundamental Technological Research
Polish Academy of Sciences
(00-049) Warszawa, Świętokrzyska 21)

A slow failure process of Rothbach sandstone and schist from Beringen in Belgium was examined, with particular attention to fault plane localization. The samples of rock were tested under uniaxial compressive stress. Acoustic emission and strain were measured during loading. The data obtained show that the localization threshold of fault plane occurred at stress levels with substantial variability relative to the ultimate strength, depending on the degree of dilatancy and homogeneity of rock under test.

1. Introduction

Deformation process and thershold of localization of strains i.e. of eventual fault plane, under uniaxial compressive stress of rock until macroscopic failure, have been investigated using acoustic emission (AE) and extensometric techniques.

Evolution of a microcrack was studied during various stages of failure process. Special attention was given to its localization to enable extrapolation of the AE data obtained in the final loading stage in laboratory, to field conditions. The experimental results obtained by TROMBIK and ZUBEREK [1] and BRADY *et al.* [2] show substantial amount of similarities between the seismic data from the surface observations and those obtained in laboratory in failure process of rock. These similarities seem to indicate that the examined phenomena in spite of significant difference in the scale, have much in common.

2. Specimen materials

The measurements were performed on laboratory samples of Rothbach sandstone and schist from Beringen, Belgium.

The Rothbach sandstone is a brittle rock, of isotropic structure, with mean porosity of 18%. Its mean compressive strength is between 40 and 50 MPa and mean longitudinal elastic wave velocity amounts to 2680 m/s.

The tested schist is a dense anisotropic, layered rock with layer planes inclined 5° to 25°. Its mean compressive strength is between 80 to 99 MPa, while mean longitudinal elastic waves velocity in this rock falls in the range 4500-4800 m/s.

The cylindrical samples 40 mm in diameter and 80 mm in length were used throughout the experiment.

3. Apparatus

3.1. *Strain measurement*

For strain measurement, the extensometers in the form of a rosette made of three resistance-type strain gauges, with the angles of 120° were attached to the rock samples surface on half of their length. The strain gauges were connected to a bridge and its output to a PC computer. Graphic form of the strain data as a function of applied stress was obtained using Mc Intosh system.

3.2. *AE measurement*

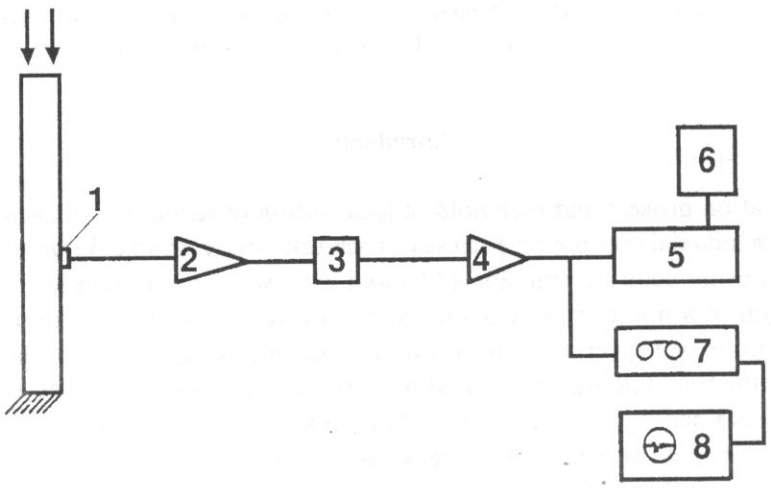

Fig. 1. Block diagram for AE measurement: (1) accelerometer, (2) preamplifier, (3) filter, (4) amplifier, (5) digital counter, (6) printer, (7) magnetic recorder, (8) digital oscilloscope.

The block diagram of the testing equipment for acoustic emission measurement is given in Fig. 1. AE signals were detected by a Bruel & Kjaer accelerometer (1) with sensitivity of 60 mV/g and flat frequency response in the range 2 Hz-20 kHz. The accelerometer was attached to the side surface of the rock samples. Its output was connected through preamplifier (2) to AE monitoring apparatus. The filtered (3) and amplified (4) signals were fed to a digital counter (5) and to a printer (6) and AE count rate was determined above the fixed reference threshold. The AE signals at the output of the amplifier (4) were recorded using a Nagra (7) magnetic tape recorder with frequency response flat in the range 20 Hz-20 kHz. The recorded signals were further processed using a digital oscilloscope (8) for determination of AE cumulative (total) count, maximum frequency spectrum, rise-time of AE signals, their maximum (peak) amplitude and also for determining of the relationship between AE and mechanical parameters i.e. load and strain.

The experimental arrangement as given in Fig. 1 was used for investigation performed in France. The measurements of AE event rate, cumulative (total) number of events and of cumulative peak amplitude were performed in Poland on several samples of the schist. The equipment used in Poland for the AE measurements was principally almost the same as used in France but its frequency range was from 1 kHz up to 100 kHz.

3.3. *Loading apparatus*

The rock specimens were loaded in a manually–operated hydraulic testing machine to avoid interference of its noises with the AE signals.

4. Experimental procedure

Loading rate effect on rock behaviour under uniaxial compression test was investigated e. g. by HOUPERT [3], SALA [4] and KHAIR [5]. Behaviour characteristic of geologic material is highly affected by the rate of applied stress and heterogeneity of the vertical stress field distribution within the structure. Inhomogeneities and discontinuities in rock which constitute obstacles for the fractures development, generally recognised as "barries" that usually form the regions of increased strength, are progressively overcome by the propagating fractures. An intervention of these "bariers" is larger with lower loading rate than with higher loading rate. This concept seems to be supported by examination of the rock failure surfaces performed by HOUPERT [3] because under lower loading rate, fracture surfaces were more rough and the fragmentation of rock samples into much smaller pieces was observed. Strength and dynamic behaviour of geologic material are reduced substantially while the AE activity increases under very low rate of applied stress, indicating also larger intervention of structural defects under lower stress rate [5]. The stress rate effect is more pronounced especially if geologic material contains larger number of defects i.e. inhomogeneities and discontinuities.

The process of rock failure in laboratory under very low loading rate is analogous to the failure process of rock mass in situ which usually occurs as a result of very low stress rate. This process is investigated in seismology where a concept of the "barriers" in a sense of the obstacle for a propagating crack was introduced by DAS and AKI [6]. Long term seismological observations usually show an increase of seismicity which precedes occurrence of dynamic rock mass failure [7, 8, 9]. Long term observations show also local rise of the terrain which precedes some of earthquakes indicating higher rate of rock mass displacement i.e. a change of the state of deformation relative to certain more or less long-lasting stable periods. Thus these observations implied performance of the AE laboratory measurements at low loading rate. They also implied concurrent measurements of both AE and strain with the aim to use the data and the relationship between them in predicting of the occurrence of dynamic seismic phenomena [10, 11, 12, 13].

In the present experiment the rock samples were tested under constant loading rate of 170 N/s in 1 min intervals. After each 1 min increment of the load it was kept constant up to the total decay of acoustic emission.

5. Sandstone data analysis

5.1. *Strain analysis*

The dependence of relative longitudinal (axial) strain ε_1, transversal strain ε_2 and volumetric strain $\varepsilon_v = \varepsilon_1 + 2\varepsilon_2$ on axial stress σ, is given in Fig. 2a for a sandstone sample. Several stages of deformation can be distinguished in the graph:

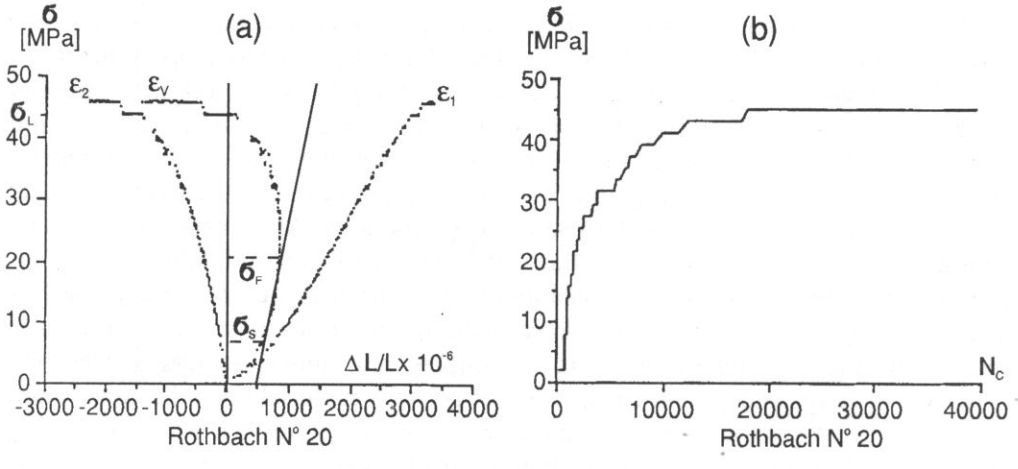

Fig. 2. Dependence of: (a) longitudinal strain ε_1, transversal strain ε_2, voulmetric strain ε_v and (b) cumulative count N_c of acoustic emission on stress σ for sandstone.

- stage in which defects do not develop; in case of primarily fissured rock it corresponds to closing of the pre-existing microfissures which can be observed on curves ε_1 and ε_v as a convexity towards the strain axis; limit of compactness stage corresponds to stress σ_s.
- stage of linear-elastic deformation, characterised by linearity of all stress–strain relationships; this phase is limited by the threshold of microcracking σ_F.
- stage of stable microcracks propagation; in this phase, above the threshold σ_F, a propagation of pre-existing microdefects begins and new microcracks develop resulting in the effect of the so called microdilatancy (or relative dilatancy); stress-transversal and volumetric strain plots loose their linearity, and growth of transversal strain occurs; relative sample volume ($\frac{\Delta v}{v} = \varepsilon_1 + 2\varepsilon_2$) decreases whilst longitudinal strain characteristic remains linear.
- stage of unstable, self- suporting microcracks propagation, observed above stress σ_L, characterised by nonlinearity of all the stress-strain curves; substantial increase of ε_2 and increase of absolute sample volume, i.e. characterised by effect of dilatancy (absolute dilatancy or macrodilatancy).

A macroscopic failure occurs as a result of bifurcation and localization of strains in a limited region that constitutes a "nucleus" of approaching failure, usually in a vertical spalling manner or in a shear mode [5]. Failure occurs at stresses higher than the threshold at which the damage begins to localize.

HOUPERT *et al.* [14] characterise stress – volumetric strain relation for brittle rock fracture by the ratio of the surface between stress axis σ and the volumetric strain curve ε_v, to the surface between stress axis σ and the linear extrapolation of the linear part of the volumetric strain curve (which corresponds to the volumetric strain curve for the same but not dilatant material), Fig. 2a. According to the authors [14] this ratio properly defines a relative value of dilatancy.

A different representation of stress and strain curves, namely as a function of loading time, Fig. 3, confirms existence of the discussed stages of the sandstone deformation process.

5.2. *Analysis of AE in sandstone*

Simultaneous analysis of strain and of acoustic emission, i.e. of cumulative count N_c as a function of compressive stress, Fig. 2b and count rate $\dot{N}_c$ as a function of loading time t, Fig. 3, confirms existence of the four stages of the sandstone failure process, namely:

- compactness stage in which AE is mostly due to the friction produced by closing of the pre-existing fissures and which occurs up to approximately 10% of the ultimate strenght σ_M,
- linear–elastic deformation stage with low AE level that is observed up to approximately 30% of σ_M,

- between 30% and 60% of σ_M, the curve of volumetric deformation indicates an effect of microdilatancy; this effect is accompanied by stable increase in AE which begins near the threshold of microcracking σ_F,
- between 60% and 80% of σ_M, AE activity increases which corresponds to the effect of dilatancy; on average at about 70-80% σ_M a marked increase of AE is observed which indicates the beginning of the heterogeneous strains distribution that is the beginning of the process of their localization.

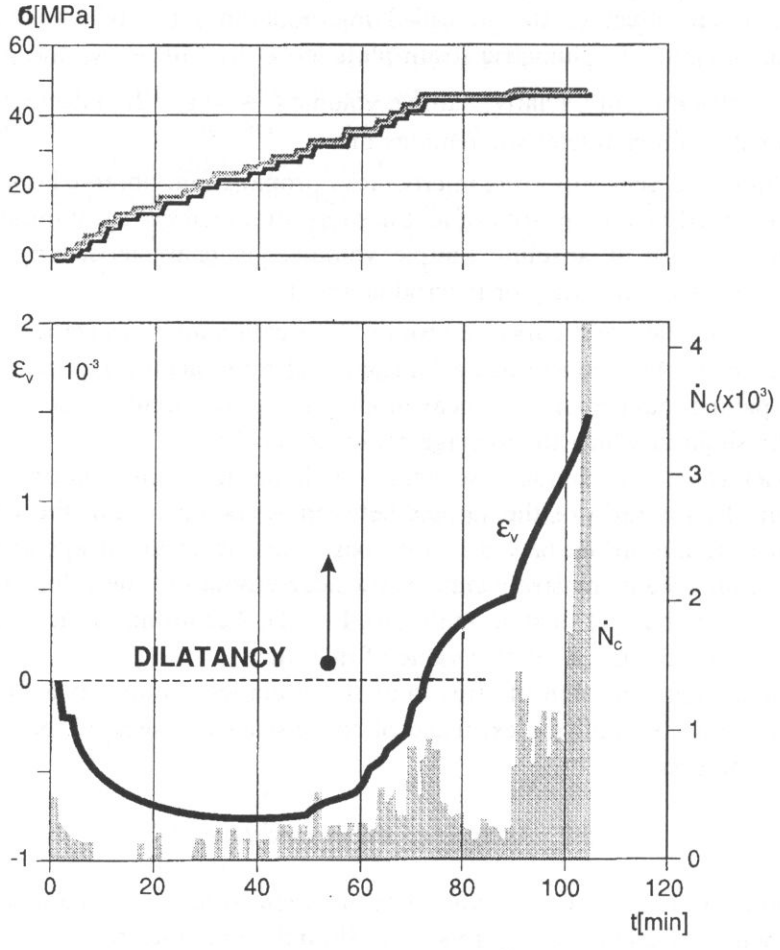

Fig. 3. Dependence of stress σ, volumetric strain ε_v and AE count rate $\dot{N}_c$ on loading time t for sandstone.

In general the AE cumulative count as a function of stress observed for the sandstone, corresponded to "Mogi" type, as presented in Fig. 4, [15].

Frequency spectrum analysis. A spectrum analysis was performed for the AE recorded signals and the maximum spectra were determined for the successive stages of deformation. The results obtained indicate evolution of the AE frequency spectra as

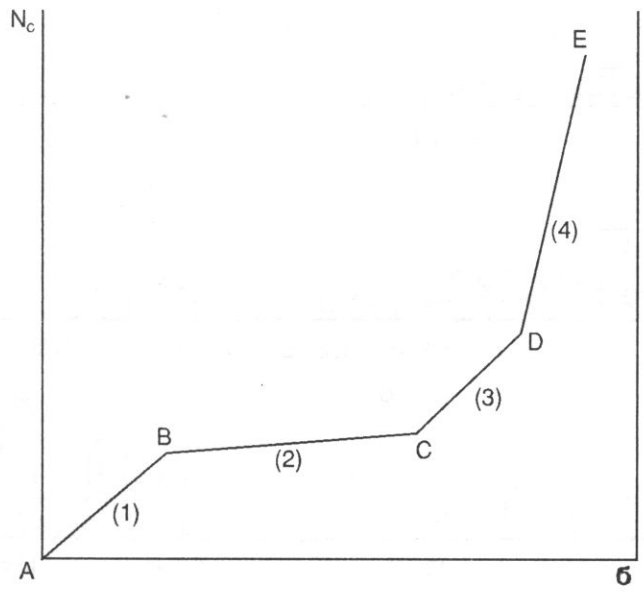

Fig. 4. AE coumulative number of events or count as dependent on stress or loading time characteristic for "Mogi" type of rock behaviour: (1) closing of fissures, (2) linear-elastic deformation, (3) stable propagation, (4) unstable propagation of microcracks.

a function of load applied to the sample [16, 17]. The results of AE spectrum analysis can be used for determining of the sample deformation stages in the failure process of rock. Characteristic maximum frequency spectra of AE for various stress levels are presented in Fig. 5 where:

a – corresponds to a stage of closing of pre-existing microfissures; relatively low frequency spectral components are observed,

b, c, d – correspond respectively: to the initiation of microcracks, to the growth of the microcracks grid density and to their coalescence: progressive upward shift of the spectral components is observed,

e – corresponds to microcracks localization, since for 70-80% of σ_M, a shift of the spectrum towards lower frequencies and decrease of dominant frequency from 8 kHz for the spectrum "d", to 2 kHz for the spectrum "e" is observed; this effect indicates an increase of the AE source dimensions.

Maximum amplitude and rise-time. A relationship between peak amplitude of AE signals and their rise-time was determined using a digital storage oscilloscope. This relationship is given in Fig. 6 for three sandstone samples. Each data point in the graph is a mean of 10 measurements for each sample. The results obtained indicate smaller rise-times for larger amplitudes of AE signals. The data are in agreement with the model of behaviour of a concrete described by REYMOND [18] for which smaller rise-times corresponded to AE signals of larger energy. With the increase of stress level and consequently with the increase of energy in AE signals, these signals

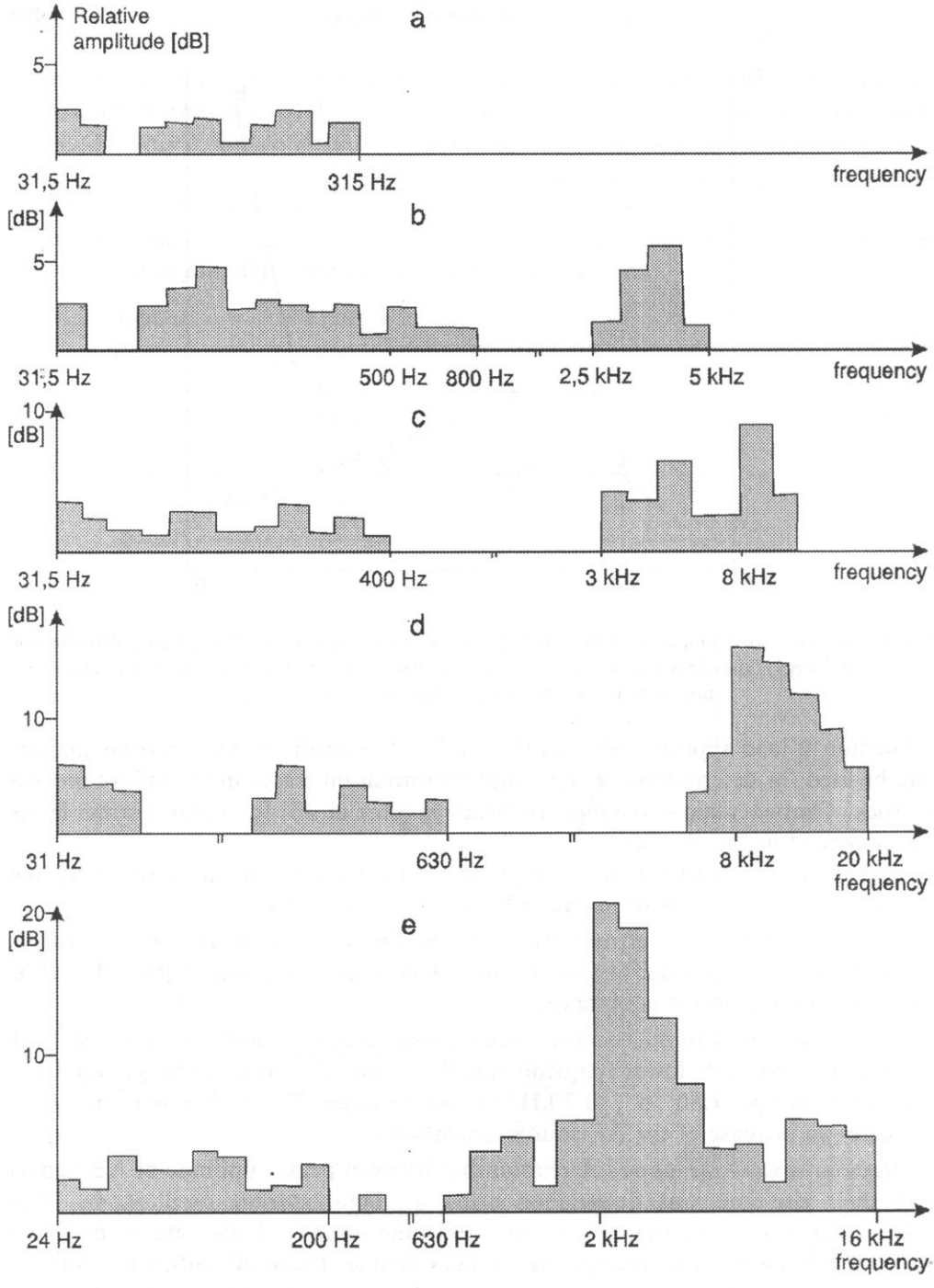

Fig. 5. Maximum AE frequency spectra of sandstone for various deformation stages: a, b, c, d, e.

had smaller rise-times and thus gained spectral components of higher frequency. These experiments [18] however, were carried out below the threshold of strains localization and therefore the effect of lowering of AE signal frequencies in the final stage of loading were not observed.

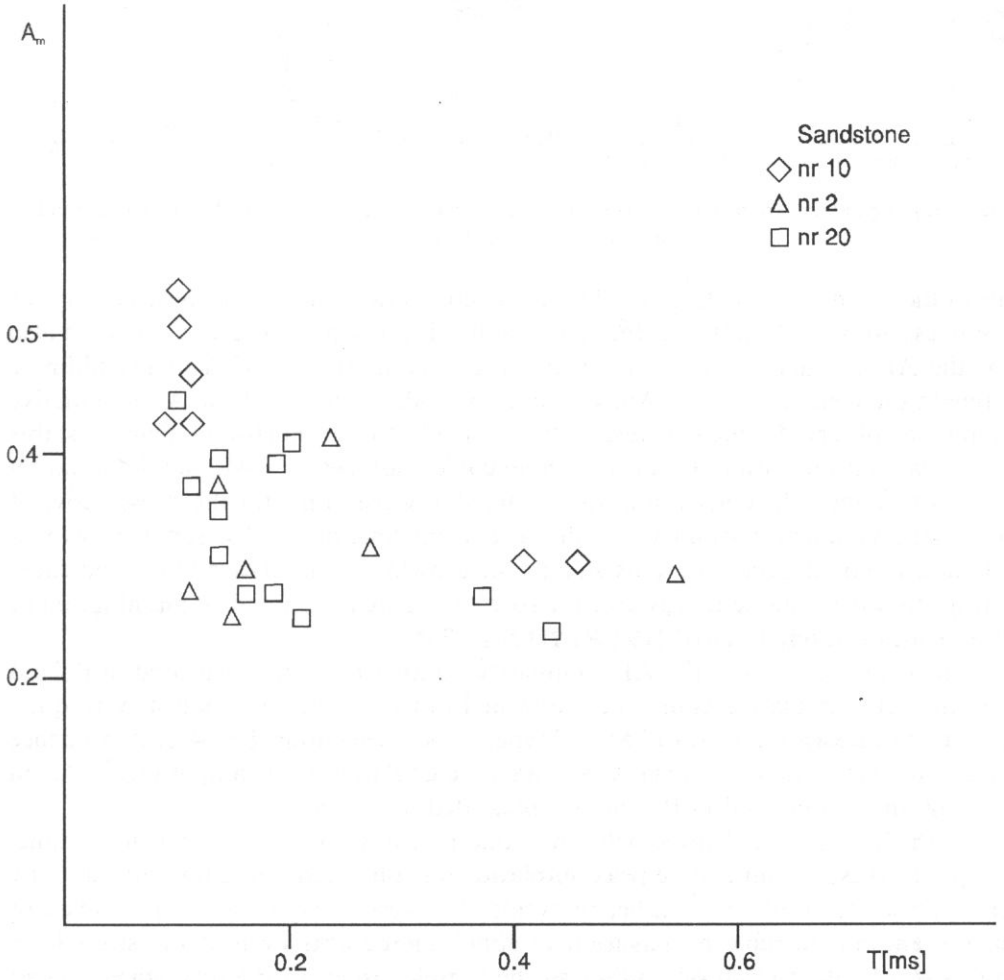

Fig. 6. Relations between maximum amplitude A_m and rise-time T of AE signals in sandstone.

6. Schist data analysis

6.1. *Analysis of strain and AE*

Strain curves for shist in a process of compressive load show a linear character of these functions, Fig. 7a. An effect of dilatancy was practically absent in the tested samples. The samples deformed linearly almost in the whole range of the stress level

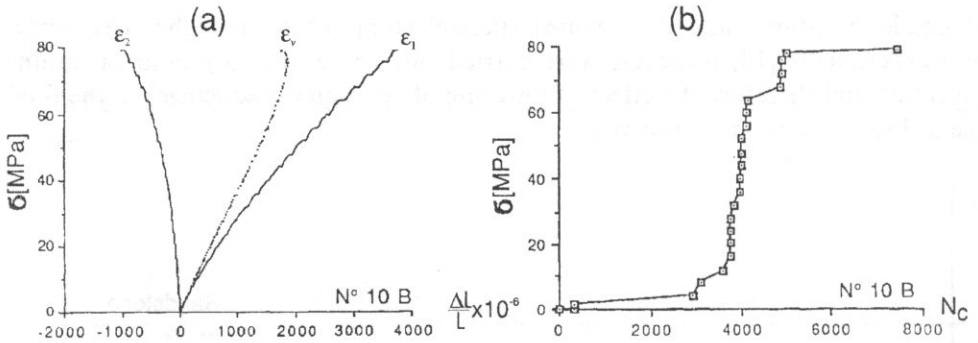

Fig. 7. (a) Logitudinal strain ε_1, transversal strain ε_2, volumetric strain ε_v and (b) AE cumulative count N_c in schist as a function of stress σ.

up to the ultimate strength limit. The volumetric strain curve lost linearity only for the stress above 90% of the ultimate strength. Linear dependence was observed also for the AE cumulative count up to the stress amounting to 85% of the ultimate strenght on average, Fig. 7b. Above this value stable increase of the AE cumulative count was observed which corresponded probably to the short-term stage of stable microcracks propagation. In this region no correlation between AE and deformation plots was found. The correlation was observed however, only for the stress above of which the volumetric strain curve declined from linearity and a rapid growth of cumulative count occurred. This significant growth of cumulative count indicated a transition from stable to unstable microcracks propagation and so an initiation of strains localization, THIMUS [19], REYMOND [20].

The characteristics of the AE cumulative number of events measured in Poland and the AE cumulative count measured in France on the same schist were quite similar. Both corresponded to "Mogi" type of rock behaviour, Fig. 4. A dependence of cumulative number of evants N_e and of cumulative peak amplitude $\sum A_m$ on loading time t, obtained in Poland are presented in Fig. 8.

Both the curves had principally the same plot however, for some loading time, a rapid increase of cumulative peak amplitude was observed, preceding substantially an increase of cumulative number of events. This result may indicate an increase of energy and an unstable propagation of some microcracks even at the stress level corresponding to 15 min of loading, in the sample tested. In the final stage of load after relatively short period of acoustic „quiescence", a rapid increase of cummulative number of AE events and of cumulative peak amplitudes, for stress about 90% of the ultimate strength, was observed indicating an initiation of strains localization. The data on maximum amplitude show that it is a "sensitive" indicator of rock behaviour under load and is a parameter closely correlated with AE source mechanism.

The evolution of AE frequency spectrum and the dependence of maximum amplitude of AE signal on its rise-time, have qualitatively the same character for the schist as for the sandstone tested.

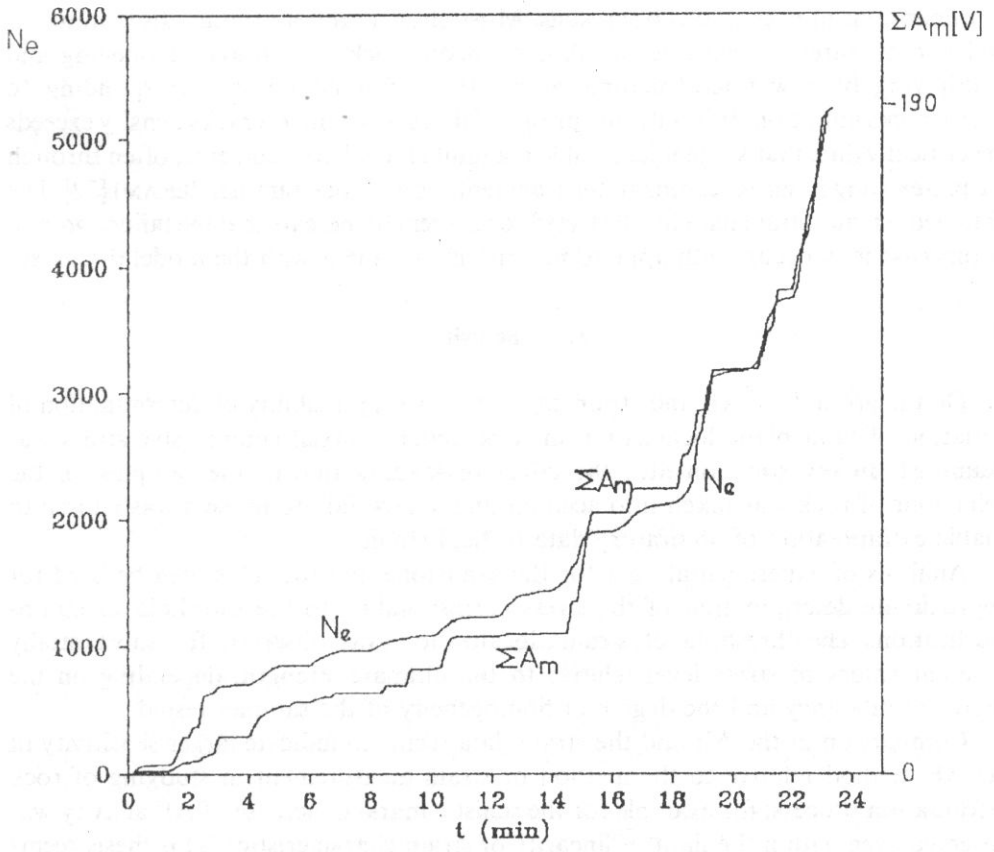

Fig. 8 Comulative number of events N_e and cumulative maximum amplitude $\sum A_m$ of acoustic emission in schist as a function of loading time t.

7. Discussion

A model of the failure process of inhomogeneous materials is generally, with certain approximation, in agreement with Griffith's theory and stems from the assumption that cracks propagate chiefly by increasing in length. In this model an initiation of microcracks is recognised, occuring above the threshold of microcracking and next a stable and an unstable propagation of cracks [21]. To this model such materials as glass, ceramics and some metals seem to suit well, whereas propagation of cracks by their elongation does not seem to be compatible with mineralogical data and with experimental observations of the behaviour of inhomogeneous rock. Actually, a failure of inhomogeneous rock seems to result from the growth in number (density) of elementary microcracks and consequently from the expansion of the dense grid of these microcracks with the dimensions determined

by dimensions of rock grains or crystals. Most often a grid of primary discontinuities and microfissures pre-existing in inhomogeneous rock is a source of opening and multiplying of new microfractures above the threshold stress corresponding to microcracks initiation. It is only just prior to failure when microcracks density exceeds the critical value, that some microcraks in a limited local area coalesce, often through the pre-existing fissures, leading to the fragmentation of rock sample, PERAMI [22]. The obtained AE and strain data for the tested schist seem to indicate that the failure process in this case may occur, with approximation, in agreement with the model discussed.

8. Conclusion

On the grounds of AE and strain characteristics a possibility of determination of initiation of fault plane localization in rock under uniaxial compressive stress was examined. In investigation also the effect of loading rate of the samples on the behaviour of rock was taken into account and a slow failure process was chosen to enable extrapolation of laboratory data to field studies.

Analysis of experimental data for the sandstone and the schist can be used for approximate determination of the stress corresponding to the threshold of strains localization. The threshold of strains localization was observed for substantially different values of stress level relative to the ultimate strength, depending on the degree of dilatancy and the degree of homogeneity of the samples tested.

Comparison of the AE and the strain data seems to indicate larger sensitivity of the AE method relative to the method of strain measurement in studying of rock deformation process; for example for the schist a marked increase of AE activity was observed even within the limit of linearity of strain characteristics. This thesis seems to be justified since the AE signals are generated by the discrete local material instabilities while the strain characteristics result from averaged data for the whole sample. The present results are in agreement with the data obtained by THIERCELIN [23] who reported the microcracks initiation thresholds for some rocks as determined by AE, to occur at lower stresses than the thresholds determined on the grounds of strain measurements.

Acknowledgements

The authors wish to express their thanks to Mr F. MARTINEAU, Unité Mixte CNRS–LCPC Paris, for technical co-operation and to professor J. F. THIMUS, Université Catholique de Louvain, for supplying of the rock samples used in the experiments.

References

[1] M. TROMBIK, and W. ZUBEREK, *Microseismic research in Polish coal mines*, Proc. 1st Conf. AE/MS Act. Geol. Struct. Mat., Trans Tech Publications, Clausthal, Germany 1975, p. 183-187.

[2] B. T. BRADY, *An investigation of the scale invariant properties of failure*, Int. J. Rock Mech. Min. Sci. Geomech. Abstr., 14, 121-126 (1977).

[3] R. HOUPERT, *Le role du temps dans le comportement à la rupture des roches*, C.R. 3 Congr. Internat. Mec. Roches, Denver, 2 et A, 1974, p. 325-329.

[4] Ph. SALA, *Etude experimentale de la fissuration et de la rupture des roches par émission acoustique*. Application à l'étude de la sismogenese, Thèse Dr Ing, Université de Grenoble 1982, p. 166.

[5] A. W. KHAIR, *Stress rate effect on A.E., Proc.* 5th Conf. AE/MS Act. Geol. Struct. Mat., Trans Tech Publications, Clausthal, Germany 1995, p. 29-43.

[6] S. DAS and K. AKI, *Fault plane with barriers; a versatile earthquake model*, J. Geoph. Res., 82, 5658-5670 (1977).

[7] C. B. RALEIGH, G. BENNETT, H. CRAIG, T. HANKS, P. MOLNAR, A. NUR, J. SAVAGE, C. B. SCHOLZ, R. TURNER, and F. WU, *The prediction of the Haicheng earthquake*, EOS Trans. Am., Geoph. Union, 58, 236-272 (1977).

[8] M. WYSS, and W. H. K. LEE, *Time variations of the average earthquake magnitude in Central California*, Proc. Conf. Tectonic Problems of the San Andreas Fault System, Stanford Univ., Publ. Geol. Sci., 13, 1973, p. 24-42.

[9] B. T. BRADY, *Anomalous seismicity prior to rock bursts; Implication for earthquake prediction*, Pageoph, 115, 357-374 (1977).

[10] T. HIRATA, *Omori's power law aftershock sequences of microfracturing in rock fracture experiment*, J. Geoph. Res., 92, B7, 6215-6221 (1987).

[11] R. REVALOR, J. P. JOSIEN, J. Ch. BESSON, A. MAGRON, *Seismic and seismoacoustic experiments applied to the prediction of rockbursts in French coal mines*, University of Minnesota USA 1988.

[12] K. MISHIHIRO, *Study on estimating initial stress and predicting failure in rock masses by AE. Rock at great depth.*, Maury and Fourmaintraux, Balkema, Rotherdam, ISBN 90619754 (1989).

[13] H. R. HARDY, Jr., *A review of international research relative to the geotechnical field application of AE/MS techniques*, Jour. Acoust. Emission, 8, 4, 65-91 (1989).

[14] F. HOMAND-ETIENNE, R. HOUPERT, *Le comportement dilatant des roches*, Laboratoire de Geomecanique-Ecole de Geologie de Nancy (1976).

[15] A. JAROSZEWSKA, *Acoustic emission in geologic materials*, in Acoustic Emission; Sources, Methods, Applications (in Polish), Pascal Publications, Warsaw 1994, p. 323-352.

[16] M. C. REYMOND, and A. JAROSZEWSKA, *Study of the AE frequency spectra of some rocks*, Archives of Acoustics, 14, 1-2, 97-109 (1989).

[17] A. JAROSZEWSKA, M. C, REYMOND, *Characteristic features of AE in some rocks*, Proc. 5th Conf. AE/MS Act. Geol. Struct. Mat., Trans Tech Publication, Clausthal, Germany 1995, p. 19-27.

[18] M. C. REYMOND, *Signature acoustique du béton*, 11 Congrés International d'Acoustique, Revue Acoust., hors serie, 5, 115-118 (1983).

[19] J. F. THIMUS, O. MOUSTACHI, J. BERGUES, M. C. REYMOND, F. MARTINEAU, *Contribution de l'émission acoustique à l'étude de la fissarution des roches*, Colloque R. Houpert, Nancy 1992, p. 229-232.

[20] M. C. REYMOND, J. F, THIMUS, and Ph. LINZE, *Acoustic emission characteristics of schists and sandstones*, British J. Non-Destructive Testing, 33, 4, 183-185 (1991).

[21] Z. T. BIENIAWSKI, *Mechanism of brittle fracture of rock*. Theory of the fracture process, Int. J. Rock Mech. Min. Sci., 4, 395-430 (1967).

[22] R. PERAMI, *Influence de la microfissuration thermique des roches sur leurs proprieties en compression*, Structure et Comportement Mécanique des Geomateriaux, Colloque R. HOUPERT, Nancy 1992, p. 77-86.

[23] M. THIERCELIN, *Application de l'émission acoustique á l'étude de la fissuration et de la rupture des roches*, Thèse de doctorat, Université de Grenoble 1980.

ARCHIVES OF ACOUSTICS
21, 4, 413–420 (1996)

SAW SENSOR FOR NO_2 DETECTION UTILIZING THE DYNAMIC CHARACTERISTIC OF THE DEVICE

W. JAKUBIK and M. URBAŃCZYK

Institute of Physics, Silesian Technical University
ul. Krzywoustego 2, 44-100 Gliwice, Poland

A surface acoustic wave (SAW) sensor for NO_2 detection with CuPc and PbPc layers, based on the dynamic characteristic of the lowest frequency mode has been developed. For the investigated concentrations range the changes in the device response, $\Delta f = f - f_0$, were very large (from a few kHz to even 10kHz), which resulted in a "jumping" of the generation system to the next frequency modes. Thus, we were not able to observe the saturation levels for the investigated concentrations and prepared phthalocyanine layers. Therefore, we decided to determine the NO_2 concentration after 480s from the moment when gas was allowed to flow through the measuring chamber. At a constant gas flow rate we have obtained a good linear dependence between the device output signal and the NO_2 concentration in pure air. In the case of CuPc films (0.27μm and 0.72 μm) the greatest sensitivity (130 Hz/ppm) has been obtained at a thinner layer and a higher gas flow rate. The sensitivity of the investigated PbPc layer (0.083 μm) was much higher (from 1200 Hz/ppm at 27°C to 2000 Hz/ppm at 70°C), thus was had to use a small concentration range (from 0.6 to 3.2 ppm NO_2) in order to maintain oscillations for at least 480s. Besides, the response of the device depends on temperature. At a higher temperature the magnitude of the response was greater and the response time shorter at this same gas concentration.

1. Introduction

Increasing pollution of the natural environment (especially of the atmosphere) stimulates research concerning new methods of monitoring the existing pollution. Gas detectors based on surface acoustic waves are now intensively investigated [1-5, 9, 10]. Adequately chosen active phthalocyanine layers in an acoustic dual delay line system have made it possible to design sensors with an especially high sensitivity, a small size and at a relatively low price. The basic principle of the measuring system, which is now well known, has been shown in Fig. 1.

Investigations carried out by many research teams in the past proved, that for the detection of NO_2 thin films of copper or lead phthalocyanines should be used [6-8]. Principally, any change in the physical properties of the thin active laver placed on a piezoelectric surface, can affect SAW propagation, However, from the practical

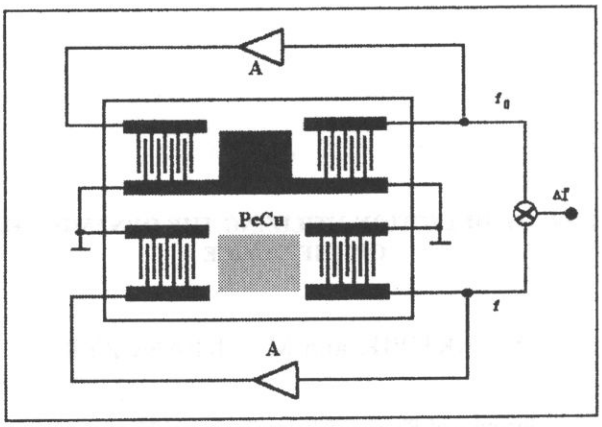

Fig. 1. The basic principle of the SAW dual delay-line oscillator system.

point of view only the two following effects have a potential meaning for phthalocyanines. Namely, a change in the mass density of the film, and a change in its electrical conductivity. Moreover, in the case of semiconducting layers the change in electrical conductivity is about three orders of magnitude bigger than that induced by mass loading [1, 5]. So, we can say, that as a result of changing the mass density and electrical conductivity of the thin phthalocyanine layer, the SAW velocity undergoes a change. These changes can be observed and measured as a frequency difference in dual acoustic delay lines – the delay line with an active thin layer and the reference delay line.

As a result of analysing the phase conditions of the generation system, the following formula defining the difference frequency has been derived [6, 12]:

$$\Delta f = f - f_0 = \frac{2\pi n - \Phi_e}{2\pi L}(v - v_0), \tag{1.1}$$

where n – integer, defining the number of frequency modes, f – frequency in the measuring path with the phthalocyanine layer, f_0 – frequency in the reference delay line, Φ_e – phase shift in the entire external circuit, v – propagation velocity of SAW in the measuring path, v_0 – velocity in the reference line, L – length of the acoustic path (distance between the central points of the transducers).

If we aasume, that Φ_e is constant (which is possible when the amplifier works in stable conditions) and the temperature is constant, then the relative change of the difference frequency is:

$$\frac{\Delta f}{f_0} = k\frac{\Delta v}{v_0}, \tag{1.2}$$

where k is the fraction of the centre- to-centre distance between the transducers affected by perturbation.

The change of the SAW velocity, v_0, can then be measured by means of precise measurements of the operating frequency, f, in the oscillator circuit of the device.

The only problem of the SAW sensor is caused by "jumping" of the generation system to higher operating frequencies during the interaction of the thin CuPc layers with NO_2 molecules. This problem is connected with the modal characteristic of the device and will be described in detail in the reference [11].

The best solution of this problem has been proposed in paper [1], where the authors made the transducers as long as the delay distance between the transducers. The oscillator operated only at one mode determinated by the fundamental resonant frequency.

2. Experimental

2.1. *Layer preparation*

CuPc layers with a thickness of about 0.27 μm and 0.72 μm and 0.083 μm for PbPc on a$LiNbO_3$ substrate, made by means of the vacuum sublimation method, have been prepared for investigations. The source of phthalocyanine vapour consisted of a quartz crucible placed in a properly formed tungsten spiral. Before the specific process of the sublimation, a copper phthalocyanine was initially out-gassed for 15 to 20 minutes at a temperature of 200°C, in a vacuum (10^{-4} Tr). The source temperature was about 600°C and the thickness was measured making use of the interference method.

2.2. *Acoustic paths*

Two identical delay lines were fabricated on the y-cut, z-propagating $LiNbO_3$ substrate.

We have obtained the fundamental resonant frequency $f_0 = 42$ MHz and the transducer bandwidth was about $\Delta f = 0.9$ MHz.

For investigations we utilized the lowest frequency modes of the device ($n = 1$). It was about 30 kHz for the 0.27 μm and 103 kHz for the 0.72 μm CuPc layer and 103 kHz for the 0.083 μm PbPc layer in the differential frequency of two acoustic oscillators. These modes were most sensitive for the studied film thicknesses and investigated NO_2 concentration range in pure air. The sensitivities of the higher frequency modes will be the subject of further researches.

3. Experimental system

All measurements were carried out with the use of a microprocessor system, which permitted the acquisition of difference frequencies, Δf. The main part of the setup was an aluminium vacuum chamber, wherein the prepared acoustic waveguides were placed. The temperature was measured on the crystal surface by a thermocouple which permitted its stabilization inside the chamber within 0.1°C. Almost

all the measurements were carried out at this same temperature of 30°C. Before measurements were taken, the chamber was initially evacuated to about 1 torr. Next, only pure air was allowed to flow through the chamber. It was then possible to determine the most stable working points of the oscillators at the required temperature. The maximal long-term (5h) temperature drift of the differential frequency, Δf, was about 20 Hz.

NO_2 gas and synthesised air were batched by means of simple system described in the reference [12]. The process of attaining the required homogeneous concentrations i the measuring chamber can be described by a simple equation (analogicaly to the charging of the condenser);

$$t(t) = c_0\left(1 - e^{\frac{-Q}{V_0}t}\right), \tag{3.1}$$

where: c_0 – is the demanded gas concentration defined by the dosing system, Q – the gas flow rate, V_0 – the cell and tubing volume.

For our experimental system we had the following magnitudes: cell volume – 30 cm^3 and tubing volume – 20 cm^3, thus V_0 is equal to 50 cm^3. The measurements were carried out for two values of the gas flow rates, namely for Q equal to 55 cm^3/s or 27.5 cm^3/s.

The time constants defined by $\tau = V_0/Q$ are then equal to about 1 or 2 seconds. A homogeneous concentration is obtained after flushing the chamber seven times for 7 or 14 seconds, respectively [2].

4. Results

In the case of the investigated thin phthalocyanine films and NO_2 concentrations we were not able to detect the saturation level of the difference frequencies. It was caused by too large frequency changes and "jumping" of the generation system to higher frequency modes. Thus, we have decided to utilize the dynamic characteristics of the device. They are shown in Figs. 2 and 3 for the 0.27 μm CuPc layer, for two different flow rates. The same characteristic has been obtained for 0.72 μm CuPc and 0.083 μm PbPc films. From the dynamic characteristic of this type it is possible to determine the device response, for example after 480s, from the moment when gas was allowed to flow through the measuring chamber.

The device response response signal, $\Delta f(480)$, for two investigated CuPc films, versus the NO_2 concentration in air is shown in Fig. 4. For the 0.27 μm layer two different flow rates have been studied. A good linear dependence, with correlation coefficients from 0.983 to 0.998, has been reached. For the 0.083 μm PbPc film the response was so high that we had to use much smaller concentrations (from 0.6 to 3.2 ppm in air) in order to maintain the oscillations for at least 480 s. The results are shown in Fig. 5 for two different temperatures.

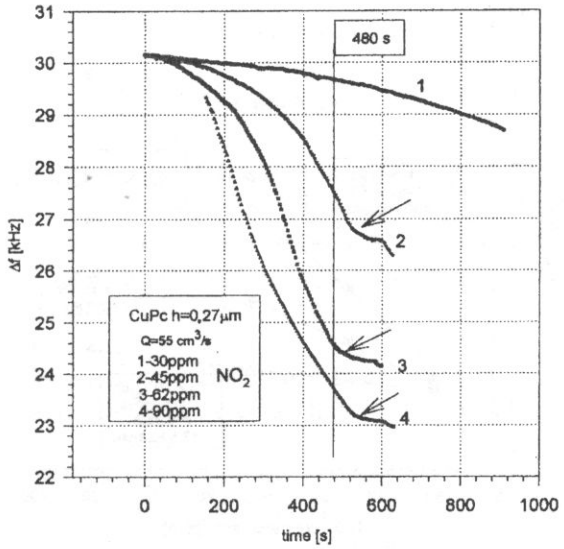

Fig. 2. Responses of the 0.27 μm CuPc layer to four NO_2 concentrations in air and for an entire gas flow rate of 27.5 cm^3/s. The small arrows indicate the moments when the NO^2 flow is cut off.

The regeneration times of the investigated layers in the measuring temperature 30°C, were very long (~10 h). Practically, for other gas concentrations the measurements were possible on the next day. In higher temperature however, the recovery time becomes much shorter (~1h).

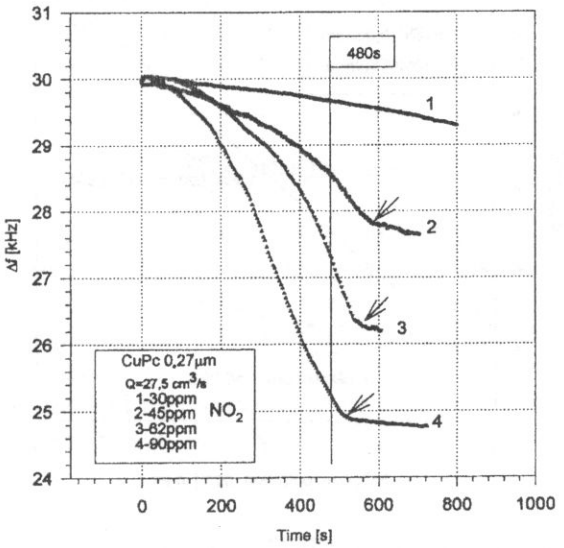

Fig. 3. Responses of the 0.27 μm CuPc layer to four NO_2 concentrations in air and for an entire gas flow rate of 27.5 cm^3/s. The arrows indicate the same as in Fig. 2.

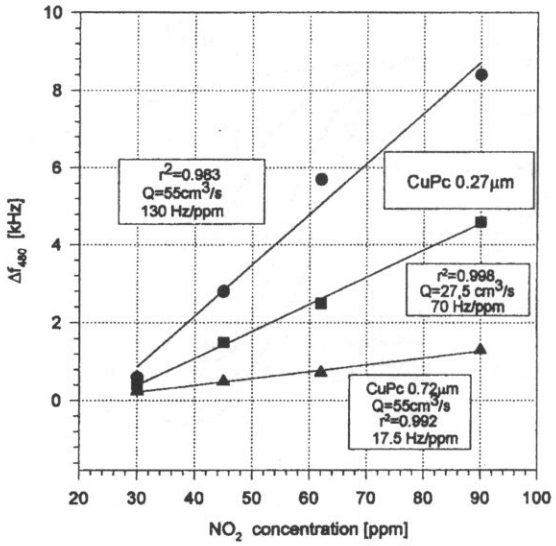

Fig. 4. Difference frequency atter 480s since the moment when the gas was allowed to flow through the measuring chamber in the case of CuPc layers, versus NO_2 concentrations in air, at a constant temperature of 27°C (300K). The device response is defined as, $\Delta f_{480} = \Delta f(0) - \Delta f(480)$, for the data in Figs. 2 and 3. For the 0.27 μm CuPc layer two gas flow rates have been studied.

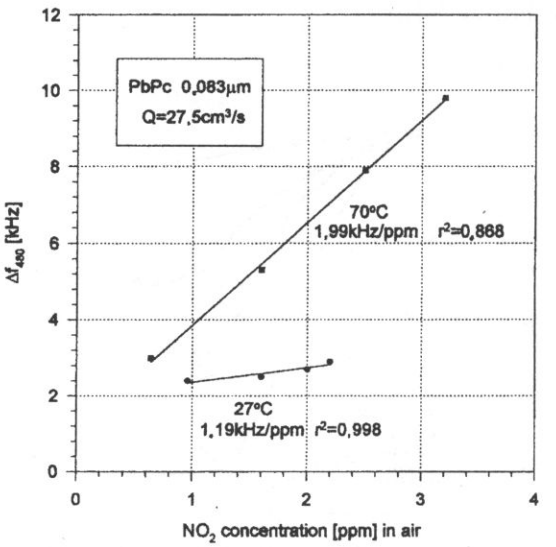

Fig. 5. Difference frequency after 480s since the moment when the gas was allowed to flow through the measuring chamber in the case of the PbPc film, versus NO_2 concentrations in air, at two different temperatures.

5. Conclusions

We are proposing a new way of determining the gas concentration basing on the dynamic characteristic of the device. In the case of our experimental system it was rather necessary, but we think that it can be a good method to determine the gas concentration for the layers with long response times (at room temperature). The determining time (480s in our case) should be much longer than the time constant of the experimental system.

For the investigated concentration range from 30 to 90 ppm of NO_2 in air for CuPc and 0.6 to 3.2 ppm for PbPc layer we have obtained a good linear dependence (Fig. 4 and 5).

The best sensitivity (130 Hz/ppm) was reached for the thinner (0.27 μm) CuPc layer and for higher (50 cm^3/s) gas flow rates. This is connected with the sheet conducitivity of the films (product of thickness and conductivity). For the thinner layer we have a smaller sheet conductivity and thus a greater change in the relative changes of velocity. The flow rate dependence of the response can be explained by the greater creating velocity of the ionised states at the surface [7], and thus in a faster change in the surface conductivity. The almost complete lack of reversibility of the NO_2 effect is undoubtedly connected with the temperature. At higher temperatures the recovery times become much shorter [8].

The sensitivity of the PbPc layer for the detection of NO_2 was much greater – from 1200 Hz/ppm at 27°C to 2000 Hz/ppm at 70°C (Fig. 5). The temperature dependence of the sensitivity can be related to the temperature dependence of the mobility of the charge carriers, and/or the easier charge exchange between interacting molecules.

Acknowledgements

We would like to thank dr S. KOCHOWSKI and K. GUT M. Sc. from the Institute of Physics at the Silesian Technical University respectively, for preparing the CuPc layers and manufacturing the SAW transducers.

We are very grateful to Mr. A. Szczelina from "Air Products Poland" for providing special NO_2 gas.

The work was sponsored by the Polish State Committee for Scientific Research within the research grant 8T10C 036 08.

References

[1] M. von SCHICFUS, R. STANCEL, T. KAMMERECK, D. WEISKAT, W. DITTRICH and H. FUCHS, *Improving the SAW gas sensor: device, electronic and sensor layer*, Sensors and Actuators B, 18-19, 443-447, (1994).

[2] M. S. NIEUWENHUIZEN, J. L. N. HARTEVELD, *An automated SAW gas sensor testing system*, Sensors and Actuators A, 44, 219-229 (1994).

[3] V. I. ANISIMKIN and I. M. KOTELYASKII, *Operating characteristic of SAW gas detectors*, Sov. Phys. Tech. Phys. 37(2), February 1992.

[4] P. BANDA, W. WŁODARSKI and J. SCOTT, *Modelling aspects of surface acoustic wave gas sensors*, Sensors and Actuators A, 41-42, 638-642 (1994).

[5] A. J. RICCO, S. J. MARTIN and T. E. ZIPPERIAN, *Surface acoustic wave gas sensor based on film conductivity changes*, Sensors and Actuators, 8, 319-333 (1985).

[6] A. VENEMA, E. NIEUWKOOP, M. VELLEKOOP, W. GHIJSEN, A. BARENDSZ and M. NIEUVENHUIZEN, *NO_2 gas-concentration measurement with a SAW-chemosensor*, IEEE Trans. Ultrasonics, Ferroelectr. Freq. Control, **UFFC-34** (2) 148-155 (1987).

[7] R. VAN EWYK, A. CHADWICK and J. WRIGHT, *Electron donor – acceptor interactions and surface semiconductivity in molecular Crystals as a function of Ambient Gas*, J. C. S. Faraday I, 76, 2194-2205 (1980).

[8] B. BOTT and T. A. JONES, *A highly sensitive NO_2 sensor based on electrical conductivity changes in phthalocyanine films*, Sensors and Actuators, 5, 43-54 (1984).

[9] R. M. LEĆ *et al.*, *Macroscopic theory of surface acoustic wave gas microsensors*, IEEE ultrasonic Symposium, Chicago 1988, 585-589.

[10] R. M. LEĆ, *Acoustic wave sensors*, Mat. Konf. COE'96. 31-43.

[11] M. URBAŃCZYK and W. JAKUBIK, *Optimal conditions for the generation system of a SAW gas sensor*, Archives of Acoustics, **21**, 1, 85-88 (1996).

[12] M. URBAŃCZYK, W. JAKUBIK and S. KOCHOWSKI, *Investigation of sensor properties of copper phthalocyanine with the use of surface acoustic waves*, Sensors and Acuators B 22, 133-137 (1994).

ARCHIVES OF ACOUSTICS
21, 4, 421–429 (1996)

ULTRASONIC ANISOTROPY IN MAGNETIC LIQUIDS

T. HORNOWSKI, A. SKUMIEL and M. ŁABOWSKI

Institute of Acoustics, Adam Mickiewicz University
60-769 Poznań, Matejki 48/49

Experimental results for magnetic field influence on the ultrasonic anisotropy in magnetic fluids are reported. The measurements have been carried out for the frequency 3.37 MHz, at the temperature 20°C and magnetic field of strength $B = 100$ mT, 200 mT and 500 mT. The results were analyzed in terms of Gotoh/Chung theory and Taketomi theory. The former was found to exhibit a lack of inner consistency while the latter gives reliable values of the physical parameters obtained by best-fit procedure.

1. Introduction

Magnetic liquids are homogeneous colloidal suspensions of ferromagnetic particles in a carrier liquid, such as water, mineral oil, or an organic compound [1, 2]. Typically, the diameter of the magnetic particles or grains in the suspension ranges from 50 to 100 Å. They are coated with a surface-active dispersive medium to avoid coagulation. However, even if atrraction between the magnetic particles is weak some coagulation dependent on the temperature, the external magnetic field, as well as their concentration cannot be avoided.

An external magnetic field acting on a magnetic liquid gives rise to a volume magnetic moment: simultaneously, the magnetization of the liquid undergoes a variation achieving saturation at a well defined value of magnetic field induction. The physical mechanism underlying the macroscopic magnetization of a magnetic liquid in an external magnetic field is related with the fact that the particles possess a rotational degree of freedom. Under the influence of the external magnetic field, by way of the electromagnetic interaction, a spatial moment appears in the liquid and orients the particle magnetic dipoles along the field direction.

Moreover, the magnetic particles in the magnetic liquid were observed to form chain-like structures due to their mutual magnetic interaction under an external magnetic field. The clusters arising under these conditions can contain more than 10^6 particles and attain a size of several micrometers [3, 4].

One of the most interesting features of magnetic liquids is their anisotropic behaviour: their physical properties exhibit directional effects of the magnetic field. One of the methods to study this anisotropy is by measuring the ultrasonic velocity and attenuation as a function of the magnetic field angle θ.

The anisotropy of sound velocity and attenuation in a magnetic fluid under an external magnetic field was studied by several authors both theoretically and experimentally [5-8]. However, there are still many problems that require elucidation. In this and subsequent articles we will report the results of our experimental studies of the ultrasonic properties of magnetic liquids and a comparison of the experimental findings with existing theories.

2. Theoretical background

The linear hydrodynamical theory of a magnetic liquid in a magnetic field is due to PARSONS [5], who dealt with magnetic fluids as nematic liquid crystals. Thus, he introduced a director n, i.e. a unit vector parallel to the local magnetization vector. Neglecting the spatial derivative terms of order higher than the first, he obtained the following expressions for the velocity and absorption coefficient of the ultrasonic wave in a magnetic liquid:

$$\frac{c-c_0}{c_0} = \frac{\omega\gamma_2^2}{8\rho c_0^2\gamma_1} \frac{\omega\tau[1-(\omega/\omega_c)^2]}{[1-(\omega/\omega_c)^2]^2+(\omega\tau)^2} \sin^2 2\theta, \tag{1}$$

$$\alpha = \frac{\omega^2\gamma_2}{8\rho c^3} \frac{[1-(\omega/\omega_c)^2]^2}{[1-(\omega/\omega_c)^2]^2+(\omega\tau)^2} \sin^2 2\theta, \tag{2}$$

where ρ is the magnetic liquid density, ω is the angular frequency of the sound wave, c is the sound velocity and ω_c is given by

$$\omega_c = \sqrt{m_0 H/I}, \tag{3}$$

with I – the moment of inertia density of the colloidal particles, m_0 – the average of the magnetization throughout the fluids, and τ is defined as

$$\tau = \gamma_1/(m_0 H). \tag{4}$$

The constants γ_1 and γ_2 can be expressed in terms of Leslie's coefficient appearing in the theory of liquid crystals [9]. Parson's theory states that the ultrasonic velocity and absorption coefficient are endowed with anisotropy dependent on the angle θ between the propagation direction of the wave and the direction of the magnetic field H. According to Parsons, this anisotropy is proportional to $\sin^2 2\theta$.

Experiment, however, failed to confirm Parsons' theory [6, 7]. Accordingly, GOTOH and CHUNG [7], on the basis of the work of TARAPOV [10] proceeded to derive a set of magnetohydrodynamical equations for magnetic liquids in an external DC magnetic field. Linearizing the equations, they obtained expressions for the

velocity and attenuation of the sound wave. In a first approximation, their theory leads to the following expressions for the attenuation and velocity of the ultrasonic wave:

$$c = c_0 \sqrt{\frac{1+a_1 x}{1+a_2 x}}, \tag{5}$$

$$\alpha = \alpha_0 \sqrt{\frac{1+a_2 x}{1+a_1 x}} \frac{1+a_3 x+a_4 x^2}{(1+a_1 x)^2}, \tag{6}$$

where $x = \sin^2\theta$. The coefficients a_1, a_2, a_3 and a_4 are in general highly complicated functions of the squared magnetic field strength H^2 and various material constants characterizing the magnetic liquid. Their determination requires that the functions of state $p(\rho, s)$, $T(\rho, s)$ and $M(\rho, T. H)$ shall be available. Nonetheless, the Eqs. (5) and (6) permit a qualitative prediction of the behaviour of the ultrasonic velocity and attenuation as functions of the angle θ between the direction of H and the propagation direction of the wave. Analysis of the derivative

$$\frac{dc}{d\theta} = c_0 \sin\theta\cos\theta(1+a_1 x)^{-1/2}(1+a_2 x)^{-3/2}(a_1 - a_2) \tag{7}$$

shows that in the interval $0 \leqslant O \leqslant 90^0$ the $dc/d\theta$ undergoes no change in sign and vanishes at the boundaries. Thus, the velocity changes monotonically with θ and has extreme values at both ends of the above interval, whereas the answer to the question of whether we deal with a decrease or an increase of the velocity depends on the sign of the expression $a_1 - a_2$. Similarly, the analysis of the derivative

$$\frac{d\alpha}{d\theta} = \alpha_0 \sin\theta\cos\theta(1+a_1 x)^{-1/2}(1+a_4 x)^{-7/2}(A_0 + A_1 x + A_2 x^2), \tag{8}$$

where

$$A_0 = a_1 + 2a_2 - 5a_4, \quad A_2 = 3a_1 a_2 - 4a_1 a_4 - 3a_2 a_4 + 4a_3, \quad A_2 = 5a_1 a_3 - 2a_1 a_2 a_4 - a_3 a_4$$

shows that depending on the value of the coefficients a_j's, attenuation has two, one or no extreme points in the interval $0 \leqslant O \leqslant 90^0$. Obviously, the linear hydrodynamical theory of Parsons and the magnetohydrodynamical theory of Gotoh and Chung lead to completely different predictions concerning the anisotropy of the ultrasonic wave propagation velocity in magnetic liquids.

The equations of motion adopted by GOTOH and CHUNG [7] do not take into account internal freedoms of the fluid. However, magneto-optical experiments [3, 4] suggest that in the presence of an external magnetic field the magnetic particles form chain-likes clusters which remain in the sample even after removal of the field. With this in mind TAKETOMI [8]) developed a theory which attributes the anisotropy of the sound absorption coefficient to the two types of motion of the clusters: rational and translational. Using a special liquid crystal theory [11] he obtained the following expression for the sound attenuation arising from rotation of the magnetic particles:

$$\alpha_{\text{rot}} = \frac{\omega^2}{2\rho c^3}\left(\frac{4}{3}\eta_s + \eta_b + 2\alpha_5 \cos^2\theta + \alpha_1 \cos^4\theta\right), \tag{9}$$

where η_s, η_b are the shear and bulk viscosities respectively, and α_1, α_5 are Leslie's coefficients [9]. It can be noted that neglecting the third and fourth terms on the righthand side of Eq. [9] one obtains the sound absorption coefficient of ordinary fluids. In order to evaluate the translational motion contribution to the coefficient of absorption of the ultrasonic wave in a magnetic fluid Taketomi assumed the model of a vibrating sphere in viscous fluid. Calculating the dissipative energy per unit volume of the magnetic fluid, he obtained the following equation for the additive sound attenuation due to translational motion of the clusters:

$$\alpha_{\text{tra}} = \frac{3\pi\eta_0 a\omega^3 VN(6\pi\eta_0 + \rho_0 V\omega)/(k^2 c)}{(\sin\theta - \rho_m V\omega^2/k^2) + (6\pi\eta_0 a\omega/k^2)}, \tag{10}$$

where k is the force constant, ρ_0, η_0 are the density and shear viscosity of the solvent, N is the number density of the clusters and ρ_m, V, a are the density, volume and radius of the cluster respectively. Qualitatively, the sum of Eqs. (9) and (10) gives predictions similar to the theory of Gotoh and Chung (two extrema in the interval $0 \leqslant \theta \leqslant 90^0$) but is more useful since it enables the assessment of some physical parameters characterizing magnetic fluids such as the number density and radious of the clusters.

3. Experimental technique

Measurements of absorption and velocity were carried out using the Matec pulse-echo technique (Fig. 1). The radio-frequency gated amplifier model 755 and gating modulator model 7700 were used to drive the piezoceramic transducer. The ultrasonic pulse, on traversal of the sample, was detected by the receiver transducer and amplified in a wide-band amplifier. The resulting pulse-echo train was observed on a CRT display. The velocity of the ultrasonic wave can be evaluated from the expression

$$c = 2lf, \tag{11}$$

where l is the distance between the transducers and f is the inverse of the double round trip time in the sample.

The model 2460B Automatic Attenuation Recorder measures the logarithmic difference (in dB) between two selected echos, say A and B, if the time gates correctly cover the main portion of the echoes. When A and B are two consecutive echoes the log(A/B) output is proportional to the absorption coefficient of the sample. The variations of log(A/B), e.g. as a function of the angle θ, give direct changes in the absorption coefficient. The accuracy of our determination of the velocity was of the order of 0.05% whereas changes in absorption coefficient were measured with error less than 1%. The absolute values of the absorption coefficient were accurate within $\pm$ 5%.

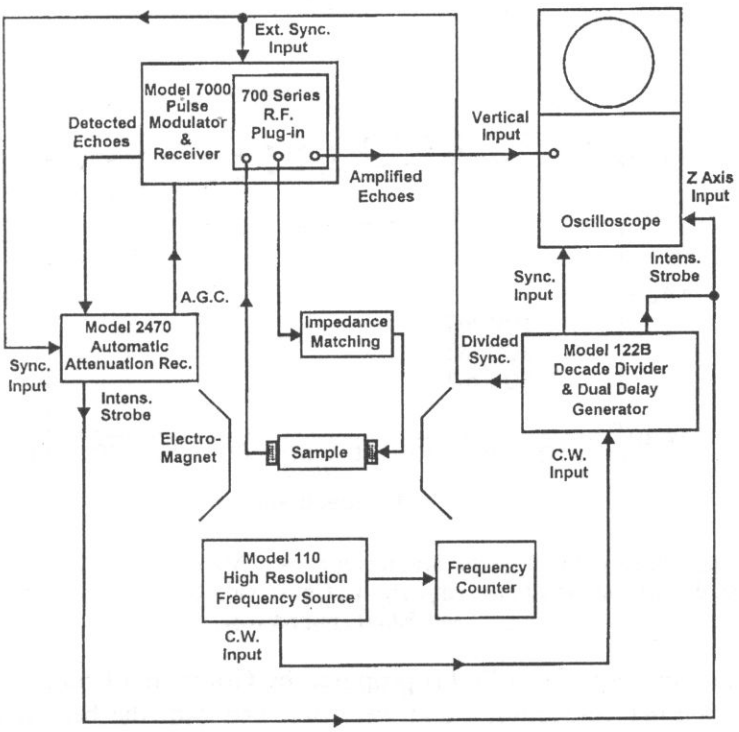

Fig. 1. Block diagram of the experimental setup.

The ultrasonic cell used in our measurements was made of brass. For the angular dependence experiment the magnetic field was rotated by five degrees each time while the measuring cell remained stationary in the gap between the electromagnetic pole pieces. The magnetic field induction was measured to within 0.5% with a F.W. Bell Gaussmeter model 9200.

4. Results and analysis

Our measurements were carried out in a magnetic liquid denoted as EMG-605 (produced by Ferrofluidics Inc.) consisting of magnetite particles Fe_3O_4 suspended in water. The values of saturation magnetization, initial susceptibility, volume concentration and viscosity were 20 mT, 0.5, 3.5% and $< 0.5\ \mathrm{N \cdot m^{-2}}$ (at 25°C), respectively. The particle distribution was a normal distribution with a maximum at 100 Å The measurements were carried out in 20°C at 4.37 MHz and in three magnetic fields B, namely 100 mT, 200 mT and 500 mT.

The angular dependence of ultrasonic velocity for the three values of B is shown in Fig. 2. Without any numerical analysis it is obvious that the experimental data do not vary in the manner predicted by Parson's theory, i.e as $\sin^2 2\theta$. The solid, dashed

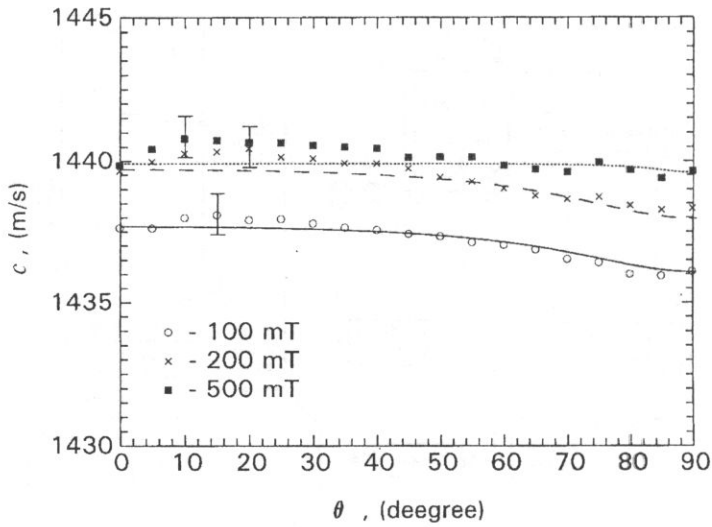

Fig. 2. Angular dependence of the ultrasonic velocity for $f = 4.37$ MHz in three magnetic field strengths. The solid, dashed and dotted lines represent the Gotoh and Chung theory for 100 mT, 200 mT and 500mT, respectively.

and dotted lines correspond to Eq.(5) proposed by Gotoh and Chung for 100 mT, 200 mT and 500 mT respectively, and were obtained with the best-fit procedure. Agreement between experiment and theory is fair, except for higher values of B for which the experimental points lie systematically above the theoretical curves. However, the data distribution does not decrease monotonically as predicted by Eq.(5) but exhibit two small extrema on both ends of the interval $0 \leqslant \theta \leqslant 90^0$.

Figure 3 shows the results for attenuatiuon, $\Delta\alpha = \alpha - \alpha_0(\theta = 0)$, *versus* θ for three values of B: 100 mT, 200 mT and 500 mT. Here, also, the experimental data do not match Parson's experssion given by Eq.(2). The lines drawn in Fig. 2 were obtained by fitting the attenuation data to Eq.(6) derived by Gotoh and Chung. Qualitatively, agreement between the experimental data and the theoretical lines is quite good though one aspect of this fitting requires clarification. Below we give the expressions used to draw the theoretical lines in Figs. 1 and 2:

$$\alpha = 28.8\sqrt{\frac{1+2.20x}{1+0.46x}}\,\frac{1+0.17x+0.23x^2}{(1+0.46x)^2}, \qquad \text{for 100 mT}$$

$$c = 1437.68\sqrt{\frac{1-0.82441x}{1-0.82399x}},$$

$$\alpha = 29.3\sqrt{\frac{1+3.19x}{1+1.63x}}\,\frac{1+2.57x+1.53x^2}{(1+1.63x)^2}, \qquad \text{for 200 mT}$$

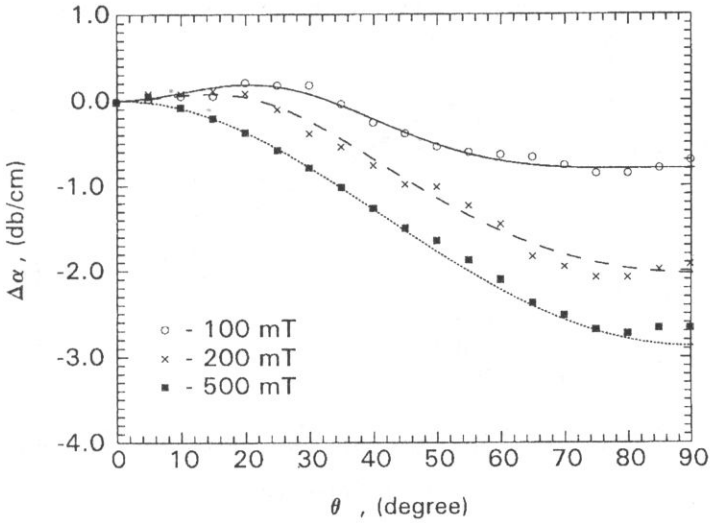

Fig. 3. Angluar dependence of ultrasonic attenuation $\Delta\alpha$ for $f = 4.37$ MHz in three magnetic field strengths. The solid, dashed and dotted lines represent the Gotoh and Chung theory for 100mT, 200 mT and 500 mT, respectively.

$$c = 1439.69\sqrt{\frac{1-0.82508x}{1-0.82465x}},$$

$$\alpha = 29.9\sqrt{\frac{1+0.35x}{1+0.29x}}\,\frac{1+0.44x+0.03x^2}{(1+0.29x)^2}, \qquad \text{for 5200 mT}$$

$$c = 1439.90\sqrt{\frac{1-0.97819x}{1-0.97818x}},$$

The coefficients a_1 and a_2 which appear both in Eqs.(5) and (6) should have similar (if not the same) values for given magnetic fields since the velocity and attenuation were measured under the same thermodynamical conditions and at the same frequency of the ultrasonic wave. This is not the case. In fact, it is impossible to get satisfactory agreement between experiment and Gotoh/Chung theory when the coefficients a_1 and a_2 obtained from fitting the velocity data to Eq.(5) are inserted into Eq.(6) for attenuation and the fitting procedure is restricted only to the coefficients a_3 and a_4. This indicates that the Gotoh/Chung theory lacks inner consistency. One possible origin of this situation seems to reside in the approximation used to solve the eigenvalue equation. However, the usefulness of the Gotoh/Chung theory is very limited since it is rather difficult to deduce any valuable information concerning the magnetic liquid on the basis of the parameters obtained through the fitting process.

Figure 4 shows the results of the analysis of the angular dependency of the absorption coefficient in terms of Taketomi's theory. The solid, dashed and dotted

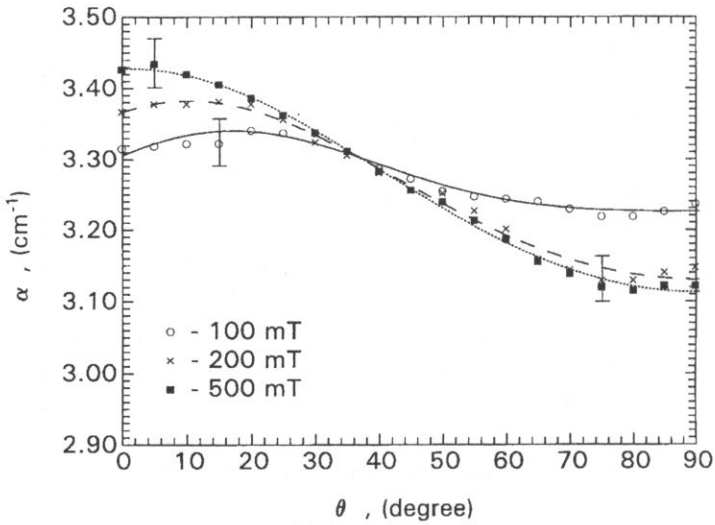

Fig. 4. Angular dependence of the absorption coefficient α for $f =$ MHz in three magnetic field strengths. The solid, dashed and dotted lines represent Taketomi theory for 100 mT, 200 mT and 500 mT, respectively.

lines were obtained by fitting the experimental results to the sum of Eqs.(9) and (10). The fitting parameters values, $\eta_s+4/3\eta_b$, α_5, α_1, a, k, N are listed in Table 1. Here, we take the values $\eta_0 = 0.1003\ \mathrm{N\cdot s\cdot m^{-2}}$, $\rho_0 = 996\ \mathrm{km\cdot m^{-3}}$ for water, and $\rho_m = 5240\ \mathrm{kg\cdot m^{-3}}$ for magnetite.

The values of $\eta_s+4/3\eta_b$ listed in Table 1 show that viscosity is about 4 – 5 cP and increases slightly with the magnetic field. The viscosity values obtained are close to those reported by the Ferrofluidics Corp.

Table 1

B mT	$\eta_s+4/3\eta_b$ $\mathrm{N\cdot m^{-2}\cdot s^{-1}}$	α_5 $\mathrm{N\cdot m^{-2}\cdot s^{-1}}$	α_1 $\mathrm{N\cdot m^{-2}\cdot s^{-1}}$	$a\times 10^6$ m	k $\mathrm{N\cdot m^{-1}}$	$N\times 10^{-16}$ $\mathrm{m^{-3}}$
100	0.41 ± 0.02	0.07 ± 0.02	0.13 ± 0.01	1.678 ± 0.002	4.27 ± 0.05	56 ± 4
200	0.42 ± 0.06	0.13 ± 0.03	0.08 ± 0.01	1.673 ± 0.009	2.87 ± 0.09	56 ± 4
500	0.48 ± 0.03	0.10 ± 0.01	0.05 ± 0.01	1.684 ± 0.009	0.14 ± 0.02	57 ± 3

Table 1 shows that the cluster radius and number density of the clusters do not change (within error) with respect to the magnetic field. We speculate that in the external magnetic field $B = 100$ mT most of the magnetic particles are bounded within the clusters so the further increase of the magnetic field neither changes the number density of the cluster nor its radius. If we assume the magnetic particles to be spheres of radius 100 Å then the number density of the magnetic particles is obtained to be $2.6 \times 10^{24}\ \mathrm{m^{-3}}$.

The force constant k depends strongly on the magnetic field, i.e. k decreases with the external field. The same effect was observed by TAKETOMI [11] who proposed the explanation of this behaviour.

The Taketomi's theory enables the assessment of some useful parameters characterizing magnetic liquids. However, it would be desirable to expand the Taketomi model to include an expression for the ultrasonic velocity.

Acknowledgements

The present work was carried out within KBN Research grant No. 2PO3B 17908.

References

[1] FERROFLUIDS CORPORATION, J. Magn. Magn. Mater., **1-4** (1986).
[2] K. RAJ, R. MOSKOWITZ, J. Magn. Magn. Mater., **85**, 233 (1990).
[3] C. F. HAYES, J. Coll. Int. Sci, **52**, 239 (1975).
[4] S. TAKETOMI, Jpn. J. Appl. Phys., **22**, 1137 (1983).
[5] J. D. PARSONS, J. Phys. D., **8**, 1219 (1975).
[6] Y. CHUNG, W. E. ISLER, J. Appl. Phys., **49**, 1809 (1978).
[7] K. GOTOH, D. Y. CHUNG, J. Phys. Soc. Jpn., **53**, 2521 (1984).
[8] S. TAKETOMI, J. Phys. Soc. Jpn., **55**, 838 (1986)
[9] M. J. STEPHEN, J. P. STRATLEY, Rev. Mod. Phys., **46**, 617 (1974).
[10] I. E. TARPOV, Appl. Math. and Mech., **37**, 770 (1973).
[11] S. TAKETOMI, J. Phys. Soc. Jpn., **54**, 102 (1985).

ARCHIVES OF ACOUSTICS
21, 4, 431–446 (1996)

ULTRASONIC INVESTIGATIONS OF INCLUSION COMPLEXES OF α-CYCLODEXTRIN WITH SODIUM ALKYL SULFATES. KINETIC AND THERMODYNAMIC PARAMETERS

A. JUSZKIEWICZ

Department of Chemistry
Jagiellonian University
(30-060 Kraków, ul. Ingardena 3)

A. BALCERZAK

Institute of Fundamental Technological Research
Polish Academy of Sciences
(00-049 Warszawa, Świętokrzyska 21)

Velocity and attenuation measurements of ultrasonic waves in aqueous solutions of α-cyclodextrin containing different sodium alkyl sulfates were made. The occurrence of an ultrasonic relaxation process, most probably connected with a deeper penetration of the alkyl chain into the cyclodextrin cavity and a more tight structure of the inclusion complexes of α-cyclodextrin with sodium decyl-, dodecyl- and tetradecyl sulfates, has been established. Thermodynamic and kinetic parameters related to this process have been calculated.

1. Introduction

Cyclodextrins (CD) are known to form so-called inclusion compounds by capturing a number of compounds into their cavities. CD are cyclic carbohydrates consisting of six (α-CD), seven (β-CD), or eight (γ-CD) D–(+) – glucopyranose units linked by α– (1.4) interglucose bonds. CD has a unique spatial configuration forming a torus shaped molecular structure with a hydrophilic exterior and a hydrophobic interior. The hydrophobic cavity forms an ideal harbor in which poorly water-soluble molecules can shelter their most hydrophobic parts. The contact between such a poorly soluble compound and CD in aqueous enviroment can result in complexation in that no covalent bonds are formed. Due to the hydrophilic outside of the CD, such a complex is a soluble entity on its own. Thus, the CD has been well-known to form inclusion compounds with a variety of molecular species by several kinds of driving forces [1, 2], where the hydrophobic interaction has been found to play an important role [2-6].

Inclusion of organic compounds by CD sometimes inhibits oxidation or biological digestion of the included compounds. The inclusion complexes have been, therefore, widely used in the fields of food, drug and agricultural industries as an encapsulating agent to protect sensitive molecules in hostile environments. CS also show catalytic activities in many kinds of reactions such as hydrolysis, decarboxylation, hydrogenation of olefins, site-specific substitution reactions of included compounds, and so on. Thus it would be of special interest to determine the fundamental processes at work when the cyclodextrin play host to other molecules in the solution.

It has been demonstrated that the addition of CD to an aqueous solution of a surfactant affects dramatically the physicochemical properties of the solution [7-32]. The reason for these changes is the ability of CD to screen the hydrophobic moieties of the surfactant molecules from contact with the surrounding aqueous media by the formation of an inclusion complex in which the hydrophobic chain of the sufractant is inserted into the CD cavity. As a result, surfactants are ideal guests which allow a systematic study of complexation with cyclodextrins since both their hydrophobic and hydrophilic (with different degree of hydrophobicity) moieties can be systematically changed. Indeed, the ability of cyclodextrins to modify the physicochemical properties of such aqueous solutions has been used to study their complexation behavior with surfactants, and a variety of experimental techniques have been used for this purpose. They include conductivity [10-16], competitive bindind using UV – visible and fluorescent probes [16-21], NMR [22], surface tension [23], sound velocity [24-28] ultrasound absorption [29, 30] and electrochemical [24, 31, 32] methods.

The ultrasonic spectroscopy technique is an important tool for the elucidation of basic solution processes and reaction mechanisms occurring in the microsecond to nanosecond range. Despite of the kinetic information, ultrasonic relaxation studies can provide thermodynamic information about the relaxation process [29, 30, 33, 34]). One such area still not well understood is the inclusion of guest molecules by cyclodextrins in their cavities.

In this article the results of the ultrasonic investigation of the inclusion complexes of α-cyclodextrin (α-CD) with sodium alkyl sulfates C_nH_{2n+1} OSO_3Na (n = 6, 8, 10, 12, 14) are presented.

2. Experimental part

Measurements of the ultrasonic velocity and the attenuation coefficient α/f^2, in the aqueous solutions of the α-CD with the sodium alkyl sulfates C_nH_{2n+1} OSO_3 (n = 6, 8, 10, 12, 14) were performed in the frequency range 1-150 MHz at 15, 25, 35 and 45°C and the concentration of 0.04M of each of the component. At 25° the measurements were also made for 0.01, 0.02 and 0.03 M equimolar solutions.

The measurements were made by means of the resonator [35-37] and pulse [34, 38] methods in the frequency range 1-10 MHz and 10-150 MHz, respectively. The measurement errors were about 5% for the former method and below 1% for the

latter one. Detailed descriptions of the equipments used in the resonator and pulse methods are presented in [36, 37] and [38, 39], respectively.

The theoretical curves were fitted to the experimental results by means of computer calculation programs. Those curves are given by the well known theoretical equation

$$\mu = 2\sum_{i=1}^{n} \mu_{m_i} \frac{f/fr_i}{1 + (f/fr_i)^2}, \tag{2.1}$$

where f is the measured frequency, fr_i the relaxation frequency, $\mu = (\alpha - Bf^2)\lambda$ represents the excess attenuation wavelength ($\lambda = c/f$, c is the ultrasonic velocity), α is the ultrasonic attenuation, B is the contribution to sound attenuation from any other processes that may occur at higher frequencies beyond the frequency range measured, μ_{m_i} is the maximum excess attenuation per wavelength, n is the number of relaxation processes.

3. Results and discussion

Results of the measurements are presented in Table 1 and Figs. 1, 2.

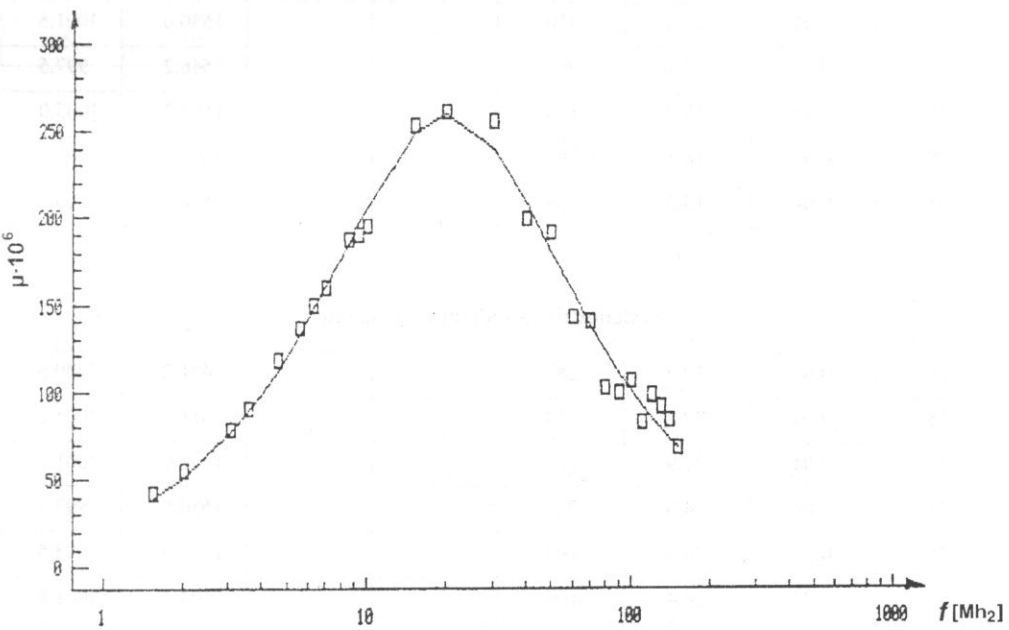

Fig. 1. Representative plot of the excess sound attenuation per wavelength, μ, vs. frequency, f, for the aqueous solution of α-CD and sodium octyl sulfate. Temperature 25°C, concentration $C = 0.04$M.

Table 1. Ultrasonic relaxation parameters, sound velocities and densities at various temperatures and concentrations for the aqueous solutions of α-cyclodextrin with sodium alkyl sulfates.

t [°C]	C [M]	f_{r1} [MHz]	$\mu_{m1} \times 10^6$	f_{r2} [MHz]	$\mu_{m2} \times 10^6$	c [m/s]	ρ [kg/m^3]
			α-cyclodextrin				
15	0.04	15.9	264			1478.2	1009.0
25	0.04	16.7	234			1506.0	1004.9
35	0.04	18.8	204			1528.9	1001.2
45	0.04	19.6	189			1543.4	997.0
25	0.03	16.8	172			1503.6	1003.1
25	0.02	16.7	102			1501.4	1001.0
25	0.01	16.4	68.2			1499.1	999.0
			α-cyclodextrin + sodium hexyl sulfate				
15	0.04	18.0	284			1480.1	1009.3
25	0.04	18.9	250			1510.0	1005.3
35	0.04	20.6	210			1530.0	1001.5
45	0.04	22.1	203			1546.2	997.5
25	0.03	18.8	175			1506.7	1003.0
25	0.02	18.5	103			1503.3	1001.2
25	0.01	19.2	69.3			1500.1	999.1
			α-cyclodextrin + sodium octyl sulfate				
15	0.04	19.5	287			1481.2	1009.6
25	0.04	20.2	259			1511.7	1005.6
35	0.04	21.9	233			1531.6	1001.7
45	0.04	24.0	203			1550.5	997.7
25	0.03	20.5	193			1508.0	1003.5
25	0.02	20.4	109			1504.3	1001.6
25	0.01	20.3	70.5			1500.4	999.2

Table 1 [cont.]

α-cyclodextrin + sodium decyl sulfate

15	0.04	24.7	293	5.4	778.3	1480.3	1010.8
25	0.04	25.8	263	6.3	85.6	1511.87	1007.0
35	0.04	28.1	240	8.8	96.8	1530.5	1003.0
45	0.04	29.9	205	9.9	106	1549.4	999.1
25	0.03	26.0	206	5.9	71.5	1508.1	1004.5
25	0.02	25.8	120	6.4	38.4	1504.3	1001.9
25	0.01	25.3	70.7	6.2	20.1	1500.5	999.6

α-cyclodextrin + sodium dodecyl sulfate

15	0.04	32.1	319	7.0	157.3	1481.9	1012.7
25	0.04	33.6	283	8.0	181	1512.1	1008.9
35	0.04	36.1	261	9.4	210	1531.9	1004.7
45	0.04	38.0	222	11.2	225	1550.8	1000.8
25	0.03	33.8	227	7.8	129	1508.1	1005.7
25	0.02	33.9	128	8.0	105	1504.4	1002.5
25	0.01	33.4	77.2	7.9	53.1	1500.6	1000.0

α-cyclodextrin + sodium tetradecyl sulfate

15	0.04	34.1	336	7.6	216.3	1482.1	1013.6
25	0.04	35.7	290	8.9	247	1513.0	1009.8
35	0.04	38.3	254	9.6	278	1533.0	1005.7
45	0.04	39.9	234	10.9	333	1551.8	1001.8
25	0.03	35.3	228	9.3	168	1509.1	1006.6
25	0.02	36.0	144	9.0	112	1504.8	1003.4
25	0.01	36.1	83.1	8.6	64.5	1500.8	1000.3

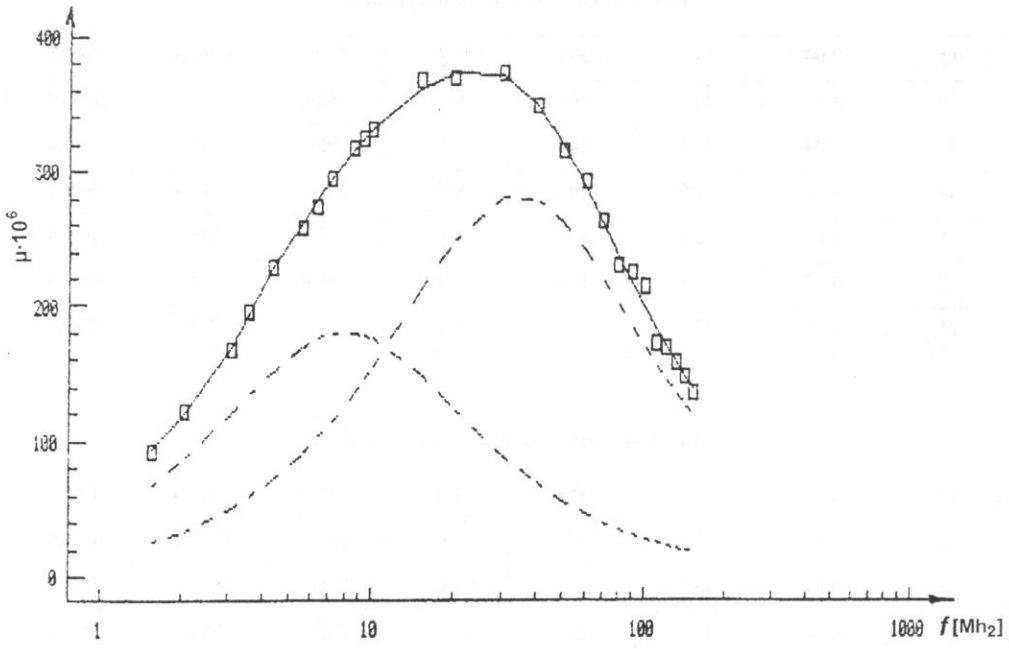

Fig. 2. Representative plot of the excess sound attenuation per wavelength, μ, vs. frequency, f, for the aqueous solution of α-CD and sodium dodecyl sulfate. Temperature 25°C, concentration $C = 0.04$M.

As an result of the carried out measurements, the high frequency relaxation processes 18-33 MHz have been found in all the investigated aqueous solutions of α-CD and the surfactants. The ultrasonic, kinetic and thermodynamic parameters of these processes are similar to those for the aqueous solution of α-CD without surfactants [39]. These relaxation processes are caused by the water molecule exchange in the hydratation shell of the α-CD molecule [29, 40]. Thus one can conclude that this kind of exchange is only slightly modified by the surfactant accomodated in the cavity of CD. More information about that will be published in another work.

In aqueous solutions of sodium decyl-, dodecyl- and tetradecylsulfate with α-CD, additional low-frequency relaxation processes were found. Within the limits of the experimental error ($\cong \pm 5\%$), for all these processes there is no dependence of the relaxation frequency f_r on the concentration of the solution C within the investigated f_r and C ranges. A linear dependence of the maximum excess attenuation per wavelength μ_m, on the concentration C has been found. Both these experimental facts indicate that the origin of these low-frequency relaxation processes is a first-order or pseudo-first-order reaction, the equilibrium of which is disturbed by the propagating ultrasonic wave

$$A_1 \underset{k_{-1}}{\overset{k_1}{\rightleftharpoons}} A_2, \tag{3.1}$$

where, in this case, A_1 and A_2 denote two stages of the inclusion complex, k_1 and k_{-1} are the rate constants for the direct and opposite reactions, respectively.

For this kind of reaction, the following kinetic and thermodynamic formulas can be derived [41-43].

The relaxation time τ^{-1} is given by

$$\tau^{-1} = 2\pi f_r = k_1 + k_{-1} = k_{-1}(1 + k) = \frac{kT}{h} \exp(\Delta S^*_{-1}/R) \exp(-\Delta H^*_{-1}/RT)\,(1 + K), \tag{3.2}$$

where $K = k_1/k_{-1}$ is the equilibrium constant for reaction (3.1) ΔS^*_{-1} and ΔH^*_1 are the activation entropy and activation enthalpy for the opposite reaction, respectively, T is the absolute temperature, R is the gas constant, k is the Boltzmann constant and h is the Planck constant.

The plot of the function (3.2) in $\ln(f_r/T)$ and $(1/T)$ coordinates is a straigth line with the slope

$$a_f = \frac{\Delta H^*_{-1}}{R} - \frac{K}{(1 + K)} \frac{\Delta H^0}{R}, \tag{3.3}$$

and the intercept b_f

$$b_f = \ln(k/2\pi h) + \frac{\Delta S^*_{-1}}{R} \tag{3.4}$$

if the following formula

$$\frac{d \ln(K)}{d\ (1/T)} = -\frac{\Delta H^0}{R} \tag{3.5}$$

has been applied. ΔH^0 is the enthalpy of the reaction (3.1).

The maximum excess attenuation per wavelength μ_m can be expressed as

$$\mu_m = \frac{\pi}{2\beta} \frac{\Delta V_s^2}{RT} ([A_1)^{-1} + [A_2]^{-1}) = \frac{\pi}{2\beta} \frac{\Delta V_s^2}{RT} \frac{K}{(1 + K)^2} C, \tag{3.6}$$

where β is the adiabatic compressibility, ΔV_s is the isentropic change of volume which accompanies the transition from the state A_1 to state A_2. $[A_1]$ and $[A_2]$ are the molar concentrations of molecules being in both the states, C is the total molar concentration, ΔV_s is related to ΔV_T, the isothermic change of volume, by the relation

$$\Delta V_s = \Delta V_T - \frac{\Theta}{\rho C_p} \Delta H^0, \tag{3.7}$$

where ρ denotes density, Θ is the expansivity and C_p is the specific heat under constant pressure. In the $\ln(\mu_m \beta T)$ and 1/T coordinates, the plot of equation (3.6) is a straigth line if the very weak temperature dependencies of ΔV and C are neglected. The slope a_μ of this line is equal to

$$a_\mu = \frac{\Delta H^0}{R} \frac{K-1}{K+1}. \tag{3.8}$$

The inercept b_μ is

$$b_\mu = \ln\left[\frac{\pi}{2} \frac{\Delta V_s^2}{R} C\right]. \tag{3.9}$$

In order to calculate the equilibrium constant K, equations (3.3) and (3.8) can be combined into the following one

$$\frac{f_r}{\frac{kT}{2\pi h}\exp(\Delta S^*_{-1}/R)} = \exp\left[\frac{1}{T}\left(a_f + \frac{K}{K-1} a_\mu\right)\right](1+K). \tag{3.10}$$

From the ultrasonic measurements one can determine a_f, a_μ and ΔS^*_{-1} (eq. (3.4)), and subsequently K.

Thus from the above mentioned dependencies, the values of the following parameters can be calculated: ΔS^*_{-1} (Eq. (3.4)), K (Eq. (3.10)), ΔH^0 (Eq. (3.8.)), ΔH_1 (Eq. (3.3)), k_{-1} (Eq. (3.2)). Next, from these values one can determine:

the rate constant of the direct reaction

$$k_1 = K k_{-1}, \tag{3.11}$$

the free enthalpy of activation of the opposite reaction ΔG^*_{-1},

$$\Delta G^*_{-1} = \Delta H^*_{-1} - T\Delta S^*_{-1}, \tag{3.12}$$

the free enthalpy of activation of the reaction (3.3), ΔG^0,

$$\Delta G^0 = -RT \ln K, \tag{3.13}$$

the entropy of this reactions, ΔS^0,

$$\Delta S^0 = \frac{\Delta H^0 \Delta G^0}{T}, \tag{3.14}$$

the enthalpy of activation of the direct reaction, ΔH^*_1,

$$\Delta H^*_1 = \Delta H^0 + \Delta H^*_{-1}, \tag{3.15}$$

the entropy of activation of this reaction, ΔS^*_1,

$$\Delta S^*_1 = \Delta S^0 + \Delta S^*_{-1}, \tag{3.16}$$

and the free enthalpy of a activation of the direct reaction, ΔG^*_1,

$$\Delta G^*_{1} = \Delta G^0 + \Delta G^*_{-1}. \tag{3.17}$$

The modulus of the molar volume change which accompanies reaction (3.1) $|\Delta V_s|$ could be obtained by transforming Eq. (3.9)

$$|\Delta V_s| = \left[\frac{2R}{\pi}\frac{1}{C}\exp b_\mu\right]^{\frac{1}{2}} \tag{3.18}$$

However, the error of this value is usually significant. Eq. (3.18) contains an exponential function which exponent b_μ is not too reliable because of the long extrapolation required. $|V_s|$ can be determined more precisely from Eq. (3.19), which results from the transformation of Eq. (3.6)

$$|V_s| = \left[\frac{2RT\beta}{\pi}\frac{(1+K^2)}{K}\frac{\mu_m}{C}\right]^{\frac{1}{2}} \tag{3.19}$$

In this case, as one can notice, it is necessary to measure the ultrasonic absorption for different values of C to determine the ratio μ_m/C.

For the tested solutions of α-CD and a surfactant, the kinetic and thermodynamic parameters of the low-frequency relaxation process, calculated from the above formulas, are presented in Table 2 and Figs. 3-11.

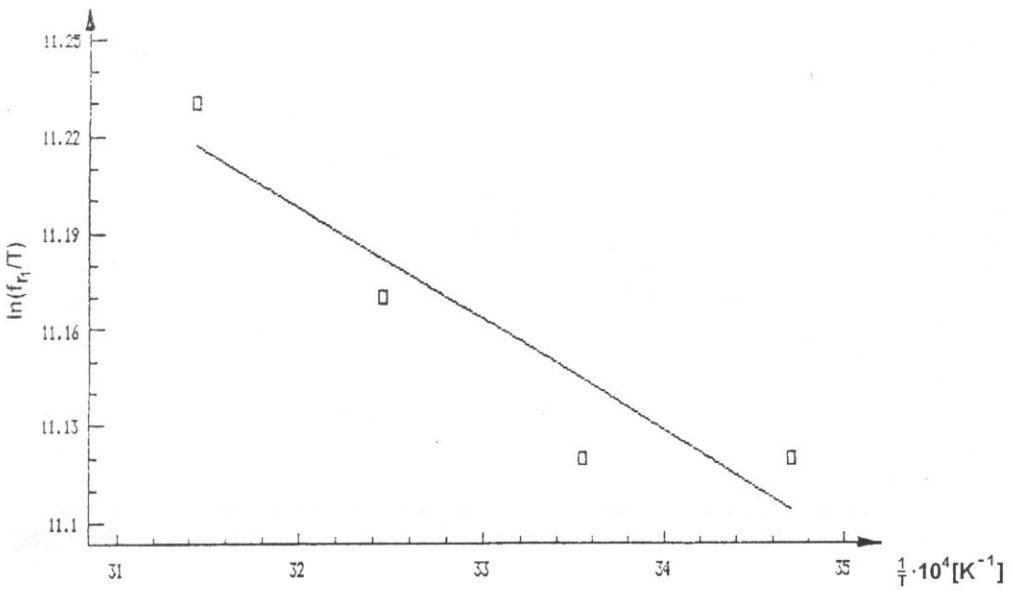

Fig. 3. Plot of μ_{m1} vs. C for the aqueous solution of α-CD and sodium octyl sulfate. Temperature 25°C.

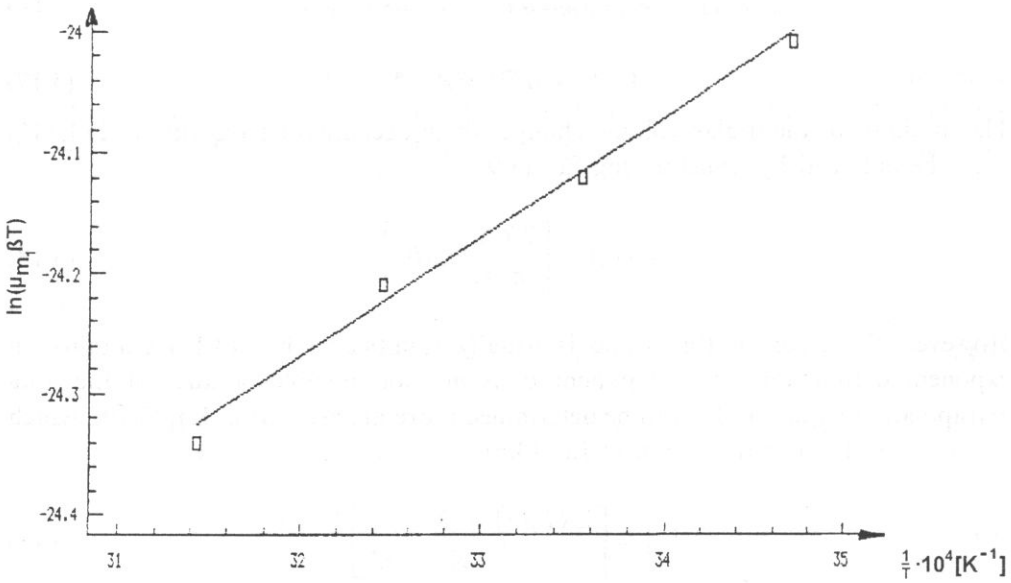

Fig. 4. Plot of $\ln(f_{rl}/T)$ vs. $(1/T)$ for the aqueous solution of α-CD and sodium octyl sulfate. $C = 0.04$ M.

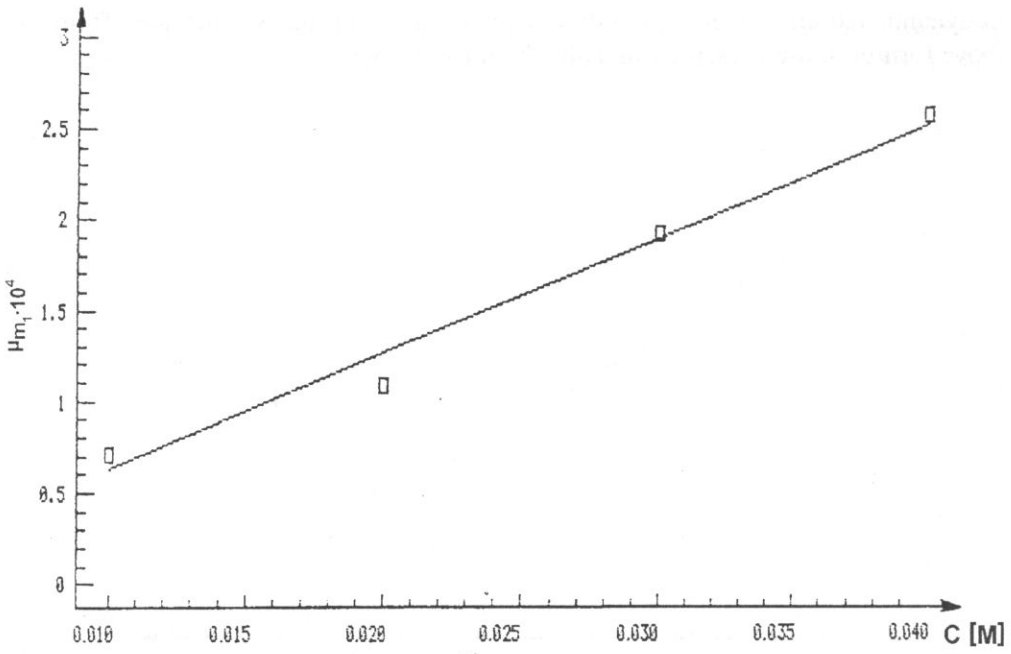

Fig. 5. Plot of $\ln(\mu_{m1}\beta T)$ vs. $(1/T)$ for the aqueous solution of α-CD and sodium octyl sulfate. $C = 0.04$ M.

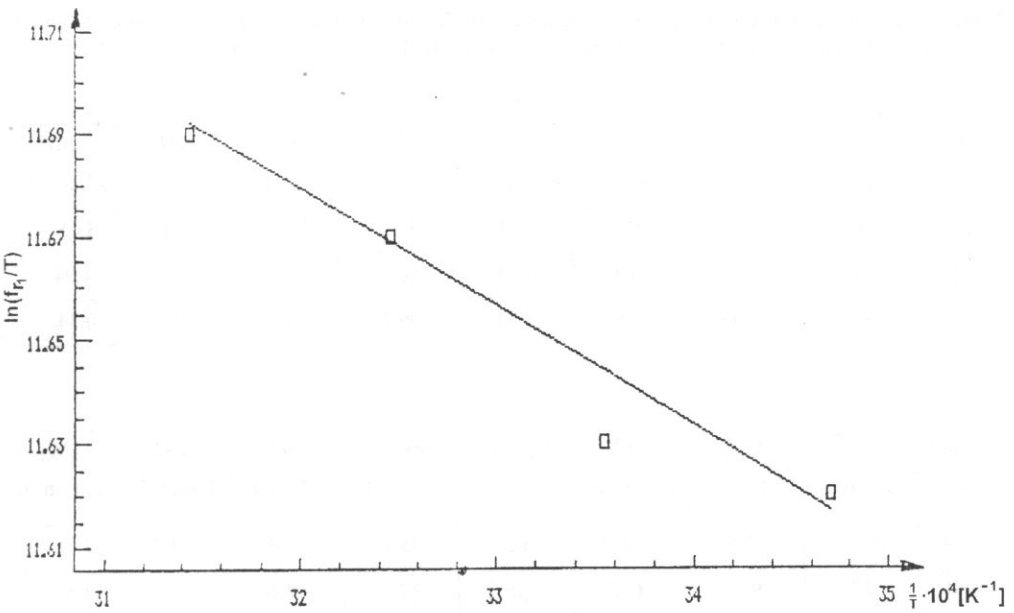

Fig. 6. Plot of μ_{m1} vs. C for the aqueous solution of α-CD and sodium dodecyl sulfate.Temperature 25°C.

The results obtained suggest that the investigated relaxation process is due to the penetration of the hydrophobic alkyl chain of the surfactant into the cavity of α-CD, this being connected with the rearrangement of the inclûsion complex into a more tight structure. The hydrophobicity of the alkyl chain increases with the length of its chain. This allows for a deeper penetration of the surfactant chain into the hydrophobic cavity of CD. This fact is confirmed by the observed increases of both the rate constant k and the equilibrium constant K when the value of n increases. The latter being rearranged into a more tight structure with a deeper built-in surfactant molecule. This complex makes CD + surfactant association more stable when the alkyl chain becomes longer. No low-frequency relaxation processes are observed for sodium hexyl sulfate and sodium octyl sulfate. This means that the above described complex does not occur in solution containing these surfactants. This is due to the lower hydrophobicity of the shorter alkyl chains of these surfactants which does not allow this chain to penetrate into the CD's cavity. Thus, the stability of this kind of association is very low.

There are several kinds of interactions between CD and the guest molecule: hydrophobic interaction, polar interaction, steric interaction, hydrogen bonding,

Table 2. Kinetic and thermodynamic parameters of the low-frequency relaxation process for the aqueous solutions of α-cyclodextrin with sodium alkyl sulfates $C_nH_{2n+1}OSO_3Na$ at 25°C.

n	a_f K^{-1}	b_f	a_μ K^{-1}	$\mu_m/C \cdot 10^6$ m^3/mol	K	ΔG^0 kJ/mol	ΔH^0 kJ/mol	ΔS^0 J/mol·K
10	-1706	15.73	-1007	2.18	30.2	-8.5	-9.0	-1.68
12	-1134	14.02	-1195	4.58	56.9	-10.3	-1.00	4.94
14	-762.3	12.83	-1352	5.94	99.4	-11.4	-11.5	-0.34

$k_1 \cdot 10^{-7}$ s^{-1}	ΔG^*_1 kJ/mol	ΔH^*_1 kJ/mol	ΔS^*_1 J/mol·K	$k_{-1} \cdot 10^{-5}$ s^{-1}	ΔG^*_{-1} kJ/mol	ΔH^*_{-1} kJ/mol	ΔS^*_1 J/mol·K	$\lvert V_s \rvert$ cm^3/mol
3.83	29.8	13.8	-53.2	12.7	38.2	22.8	-51.5	7.0
4.94	29.2	9.3	-66.7	8.7	39.2	19.6	-65.7	13.8
5.54	28.8	6.2	-75.9	5.6	40.2	17.7	-75.6	20.5

the torsional energy of the CD ring and the release of water molecules with high energies. Among these interactions, the hydrophobic and van der Waals (polar + steric) interactions might be mainly attributable to the thermodynamic parameters [44, 45].

The relatively very low value of ΔS^0 and its increase with increasing n can be caused by two competitive interactions. The increase of the length of the alkyl chain causes a decrease of the van der Waals interactions between a polar head of the surfactant and the hydroxyl groups at the edge of the CD molecule ($\Delta S < 0$). At the same time, the hydrophobic interactions of the more hydrophobic chain with the cavity increase ($\Delta S \geqslant 0$).

The decrease of ΔH^0, when n increases, can be attributed to the increase in the van der Waals interaction between the inner wall of the CD molecule and the alkyl chain of the surfactant.

Experimental data confirms the conclusions mentioned above.

The results of measurements obtained by means of different methods [10, 12, 16, 31, 46] indicate an increase in the stability constants of association of CD and the surfactants when the length of the carbon chain increases. The values of the stability constants are significantly greater than those of K. This indicates that K referes to one of the many steps that occurr in the complexation process [2].

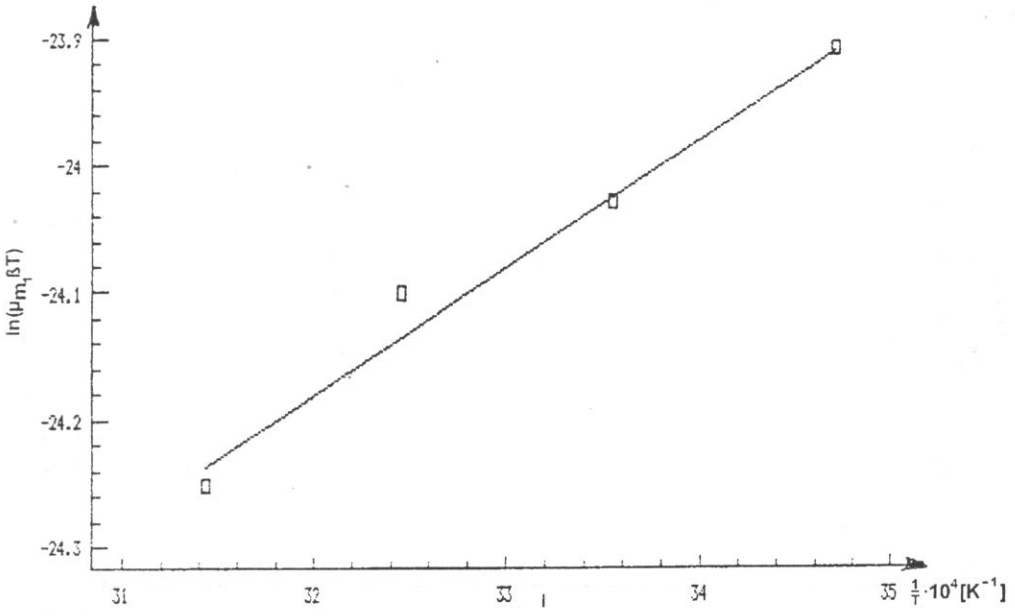

Fig. 7. Plot of μ_{m2} vs. C for the aqeous solution of α-CD and sodium dodecyl sulfate. Temperature 25°C.

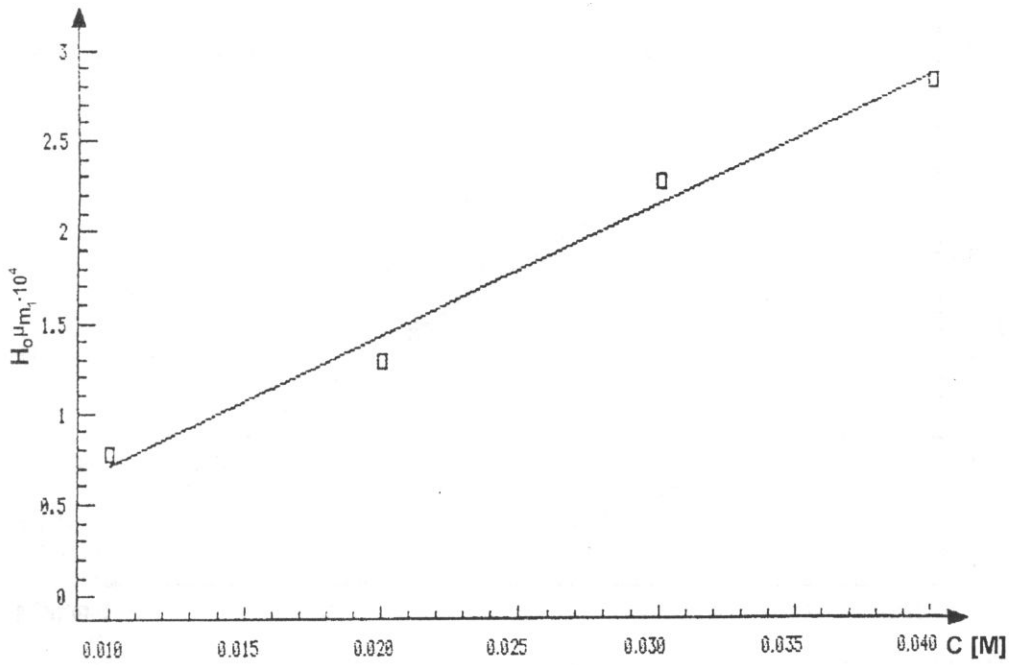

Fig. 8. Plot of $\ln(f_{r1}/T)$ vs. $(1/T)$ for the aqeous solution of α-CD and sodium dodecyl sulfate. $C = 0.04$ M.

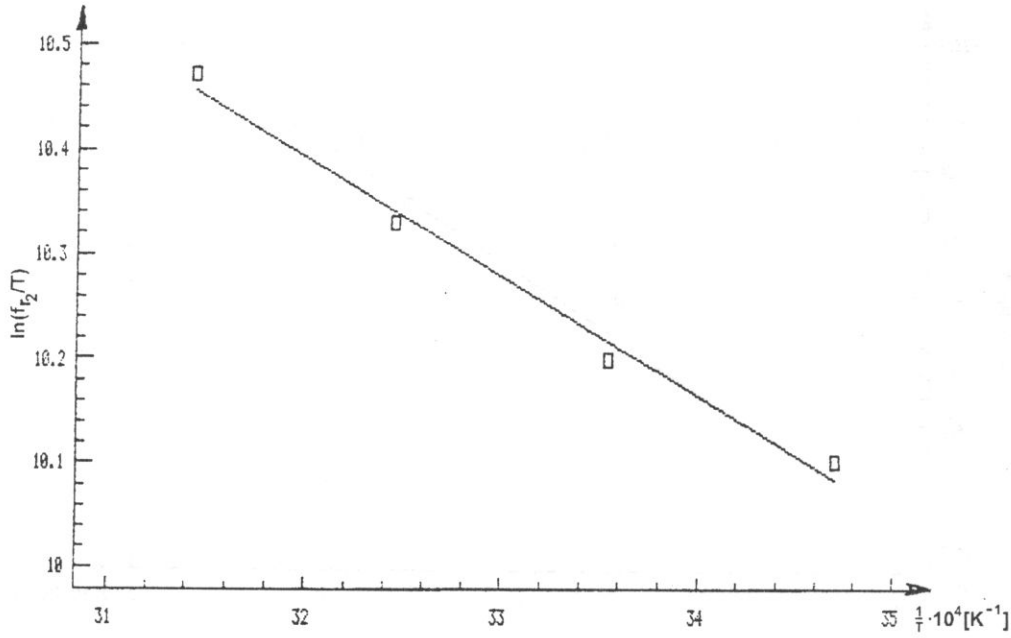

Fig. 9. Plot of $\ln(f_{r2}/T)$ vs. $(1/T)$ for the aqueous solution of α-CD and sodium dodecyl sulfate. $C = 0.04$ M.

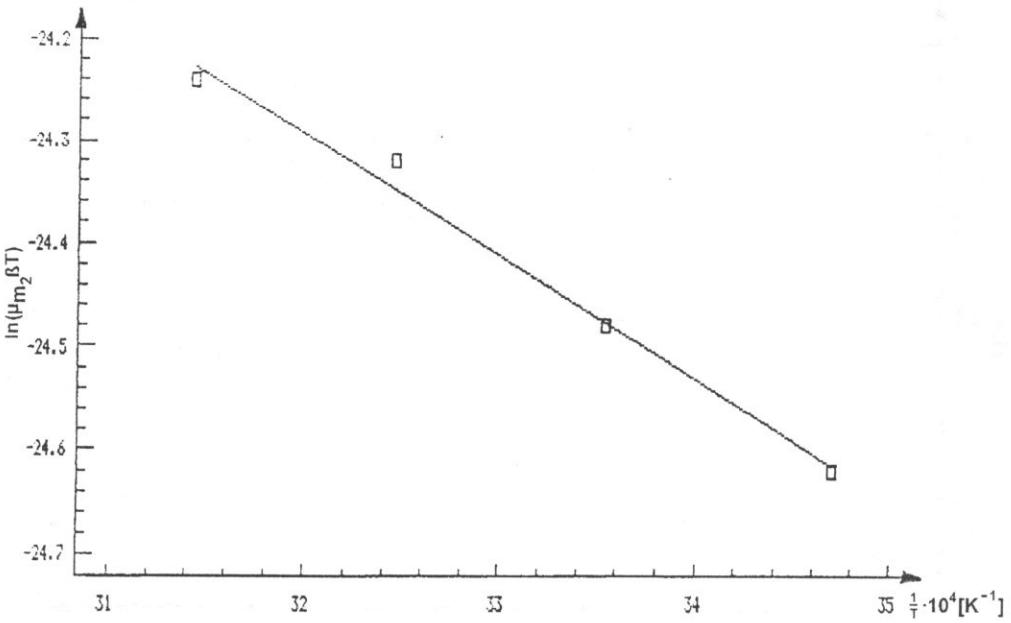

Fig. 10. Plot of $\ln(\mu_{m1}\beta T)$ vs. $(1/T)$ for the aqueous solution of α-CD and sodium dodecyl sulfate. $C = 0.04$M.

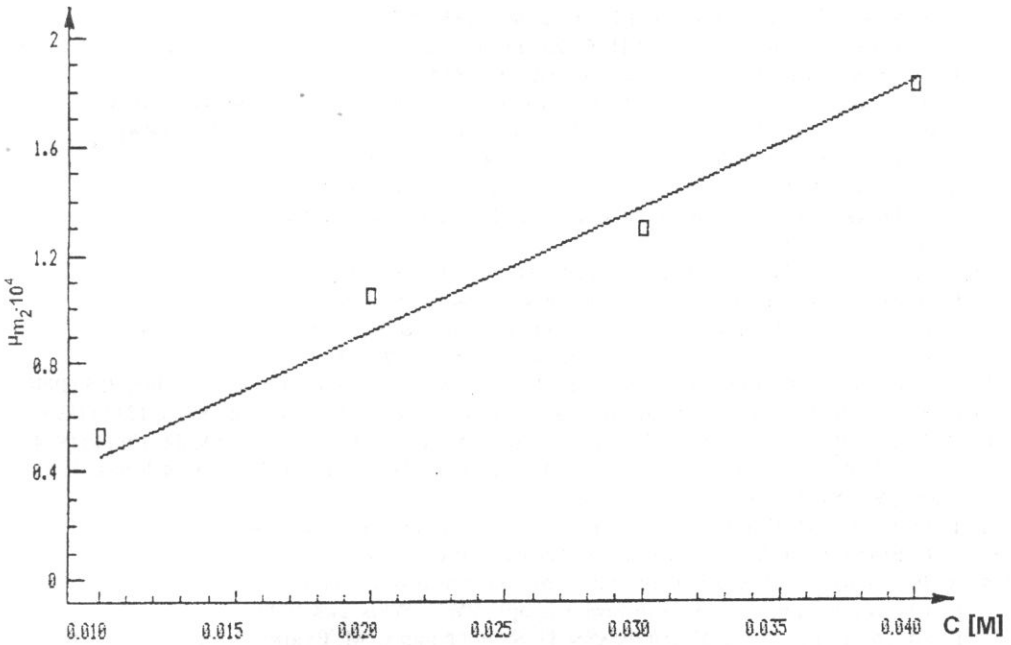

Fig. 11. Plot of $\ln(\mu_{m2}\,\beta T)$ vs. $(1/T)$ for the aqueous solution of α-CD and sodium dodecyl sulfate. $C = 0.04$ M.

References

[1] M. L. BENDER and M. KOMIYAMA, *Cyclodextrin chemistry*, Springer Verlag, Berlin 1978.
[2] J. SZEJTLI, *Cydlodextrins and their inclusion complexes*, Akademiai Kiado, Budapest 1982.
[3] M. KOMYIAMA and M. L. BENDER, J. Am. Chem. Soc., **100,** 2259 (1978).
[4] W SAENGER, Angew. Chem., **19,** 344 (1980).
[5] W. SAENGER, *Inclusion compunds*, (Eds.] J.L Atwood, J. E. D. Davies. D. D MacNicol. Academic Press, London 1984, vol. 2.
[6] C. TANFORD, *The hydrophobic effect. Formation of micelles and biological membranes*, 2 nd ed., John Wiley and Sons, New York 1980.
[7] T. OKUBO, H. KITANO and N.ISE, J. Phys. Chem., **80,** 2661 1976.
[8] N. FUNSSAKI, H.YODO and S. NEYA, Bull. Chem. Soc. Jpn., **65,** 1323 (1992).
[9] V. T. LIVERI, G. CAVALLARO, G. GIAMMONA, G. PITARRESI, G. PUGLISI and C. VENTUNA, Termochim. Acta, **199,** 125 (1992).
[10] I. SATAKE, T. IKENOUE, T. IAKESHITA, K. HAYAKAWA, T. MAEDA, Bull. Chem. Soc. Jpn., **58,** 2746 (1985).
[11] I. SATAKE, S. YOSHIDA, K. HAYAKAWA, T. MAEDA and Y. KOSUMOTO, Bull. Chem. Soc. Jpn., **59,** 3991 (1986).
[12] R. PALEPU and V. C. REINSBOROUGH, Can. J. Chem., **66,** 325 (1988).
[13] D. J. JOBE, R. E. VERRAL, R. PALEPU and V. C. REINSBOROUGH, J. Phys. Chem., **92,** 3582 (1988).
[14] R. PALEPU and V. C. REINSBOROUGH, Can. J. Chem., **67,** 1550 (1989).
[15] R. PALEPU, J. E. RICHARDSON, V. C. REINSBOROUGH, Langmuir, **5,** 218 (1989).

[16] E. S. AMAN, D. SERVE, J. Colloid Interface Sci., **183,** 365 (1990).
[17] A. HERSEY, B. H. ROBINSON and H. C. KELLY, J. Chem. Soc. Faraday Trans., I **82**, 1271 (1986).
[18] J. W. PARK and H. J. SONG, J. Phys. Chem., **93,** 6454 (1989).
[19] K. J. SASAKI, S. D. CRISTIAN, E. E. TUCKER, J. Colloid Interface Sci., **134,** 412 (1990).
[20] J. W. PARK, K. H. PARK, J. Inclusion Phenom. Mol. Recognit. Chem, **17,** 277 (1994).
[21] Y.-B. JIANG and X.-J WANG, Appl. spectrosc., **48,** 1428 (1994).
[22] B. M. FUNG, W. GUO, S. D. CHRISTIAN, Langmuir, 8, 446 (1992).
[23] U. R. DHARMAWARDANA, S. D. CHRISTIAN, E. E. TUCKER, R. W. TAYLOR, and J. F. SCAMEHORN, Langmuir, **9**, 2258 (1993).
[24] D. JEZEQUEL, A. MAYAFFRE, and P. LETELLIER, Can. J. Chem., **69,** 1865 (1991).
[25] E. JUNQUERA, E. AICART, and G. TARDAJOS, J. Phys. Chem., **96,** 4533 (1992).
[26] E. JUNQUERA, G. TARDAJOS and E. AICART, J. Colloid Interface Sci., **158,** 388 (1993).
[27] E. JUNQUERA, G. TARDAJOS and E. AIRCART, Langmuir, **9,** 1213 (1993).
[28] E. JUNQUERA, J. G. BENITO, L. PENA and E. AIRCART, J. Colloid Interface Sci., **163,** 355 (1994).
[29] D. J. JOBE, R. E. VERRALL, E. JUNQUERA and E. AIRCART, J. Phys. Chem., **97**, 6, 1243 (1993).
[30] D. J. JOBE, R. E. VERRALL, E. JUNQUERA and E. AICART, J. Phys. Chem., **98**, 42, 10814 (1994).
[31] W. M. Z. Wan YUNUS, J. TAYLOR, D. M. BLOOR, D. G. HALL and E. J. WYN-JONES, J. Phys. Chem., **96.**, 8979 (1992).
[32] T. TOMINAGA, D. HACHISU, and M. KAMADO, Langmuir, **10,** 4676 (1994).
[33] C. F. BERNASCONI, *Relaxation kinetics,* Academic Press, New York 1976.
[34] A. JUSZKIEWICZ and A. ANTOSIEWICZ, *Ultrasonic spectroscopy in molecular biophysics,* [in Polish] part II, vol. 5 [in monograph:] Biospectroscopy, PWN, Warszawa 1990.
[35] F. EGGERS, F. FUNCK, K. H. RICHMANN, H. SNEIDER and E. M. EYRING, J. Phys. Chem., **91**, 1961 (1987).
[36] G. GALIŃSKI, Z. KOZŁOWSKI, Sci. Instrum., **43,** 4 (1989).
[37] A. BALCERZAK, Z. BAZIOR, and Z. KOZŁOWSKI, [in Polish], IFTR Reports 17 (1992).
[38] A. BALCERZAK and R. PŁOWIEC [in Polish], IFTR Reports 21 (1994).
[39] A. JUSZKIEWICZ and A. BALCERZAK, Archives of Acoustics, **18,** 447 (1993).
[40] S. KATO, H. MOMURA and Y. MIYARA, J. Phys. Chem., **89,** 5417 (1985).
[41] J. LAMB, *Physical acoustics* , [Ed.] W. P. Mason, Academic Press, New York 1965, vol. II, part A, chapter 4.
[42] C. C. CHEN, S. PETRUCII, J. Phys. Chem., **86**, 2601 (1982).
[43] L. J. RODRIGUEZ, E. M. EYRING and S. PETRUCCI, J. Phys. Chem., **93,** 6356 (1989).
[44] S. J. GILL, N. F. NICHOLS and I. WADSO, J. Chem. Thermodyn., **8**, 445 (1976).
[45] P. D. ROSS and S. SUBRAMANIAN, Biochemistry, **20,** 3096 (1981).
[46] H. KITANO and T. OKUBO, J. Chem. Soc. Perkin Trans., **2,** 432 (1977).

ARCHIVES OF ACOUSTICS
21, 4, 447–458 (1996)

SHEAR ULTRASONIC INVESTIGATIONS OF POLYHYDRIC ALCOHOLS

M. WACIŃSKI

Institute of Chemistry Silesian University
40-006 Katowice, ul. Szkolna 5

R. PŁOWIEC

Institute of Fundamental Technological Research
Polish Academy of Sciences
00-049 Warszawa, ul. Świętokrzyska 21

The influence of the hydrogen bonds and the steric factor on the steady flow viscosity (η_0) and the limited shear elasticity (G_∞) of polyhydric alcohols have been investigated by ultrasonic methods.

1. Introduction

Hitherto investigations showed, that the viscosity of liquids depends on the frequency of shearing and decreases when the latter increases, i.e. a liquid behaves as a non-newtonian one. When the frequency of shearing is sufficiently high, the reaction of a liquid to the shearing stress may be viscoelastic or even elastic. To determine the reaction of a liquid on shear stress, the ultrasonic methods are irreplacable by other methods since they allow to generate the shear stress within a broad frequency range (from 10^4 Hz to 10^9 Hz). It is possible to extend this range up to 10^{12} Hz when the frequency-temperature superposition method is applied. [1, 2]. For most of the liquids it is possible to determine the full relaxation curve, i.e. to find the range of the viscous, viscoelastic and pure elastic reactions on shearing stresses.

2. Theory

In shear ultrasonic measurements the shear mechanical impedance is measured. This value is determined as a reaction of a liquid on the shearing stress. The shear

impedance (Z_T) is the quotient of the shearing stress to the velocity of the particle. For a solid this value is real and equal to

$$Z_T = \rho C_T = \sqrt{\rho C_\infty}, \tag{1}$$

where C_T is the shear wave velocity, G_∞ – the shear elastic modulus and ρ is the density of solid.

The mechanical shear impedance of a liquid is complex and frequency dependent:

$$Z_T^*(\omega) = \sqrt{\rho G^*} = (1+j)\sqrt{\pi f \rho \eta} = R_T(\omega) + j X_T(\omega) \tag{2}$$

$$\text{as } G^x(j\omega) = G'(\omega) + jG''(\omega)$$

$$Z_T^*(\omega) = \rho G^* = \rho G'(\omega) + j G''(\omega)) \tag{3}$$

where ω is the angular frequency and ρ the density of the liquid. There is a simple relationship between the shear mechanical impedance, which is measured by ultrasonic methods, and the components of the shear elastic modulus:

$$G'(\omega) = \frac{R_T^2 - X_T^2}{\rho} \qquad G''(\omega) = \frac{2R_T X_T}{\rho} \tag{4}$$

$$\lim_{\omega \to 0} G'(\omega) = G_0 = 0 \qquad \lim_{\omega \to 0} G''(\omega) = \frac{2RT^2}{\rho} = \frac{2X_T^2}{\rho} = \omega \eta_0 \tag{5}$$

For a non-newtonian liquid, the real component (R_T) is higher than the imaginary one and when the frequency increases also the shear elasticity of the liquid does so. For very high frequencies of shearing the shear elasticity $G'_{(\omega)}$ reaches limited value, G_∞ while the viscosity decreases to zero:

$$\lim_{\omega \to 0} G'(\omega) = G_\infty = \frac{1}{I_\infty} = \frac{R_T^2}{\rho}, \qquad \lim_{\omega \to 0} G''(\omega) = 0, \tag{6}$$

where J_∞ is the shear compliance of the liquid.

The G_∞ values are different for various liquids and characterize the molecular structure of the liquid. This investigation is aimed at the determination of the relation between G_∞ and the molecular structure of alcohols which have two or three hydroxyl groups in the molecule. The formulas of investigated alcohols are given in Table 1.

The value $^{n}OH/n_c$ in Table 1 is the number of - OH groups corresponding to a carbon atom, and may be considered to be the concentration of H bonds. The last column informs about the number of alkyl groups $^{n}CH_3$,$^{n}CH_5$ $^{n}C_2H_7$, present in a molecule of the investigated alcohols.

3. Measurements

– The density of alcohols was measured by a pycnometer within the temperature range 273 – 303 K. The temperature was stabilized better than $\pm$ 0.05 deg. and the density was measured with an accuracy of $\pm$ 0.02%,

Table 1.

Alcohol investigated	Structural formula	$^{n}OH : n_c$	No. of alkyl groups
Glycerol	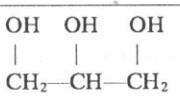	3:3 (1:1)	0
Hexanetriol-1,2,6	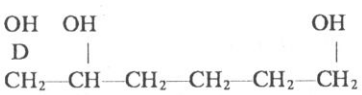	2:6 (1:3)	0
Ethanediol-1,2 (Ethylene glycol)	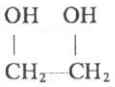	2:2 (1:1)	0
Propanediol	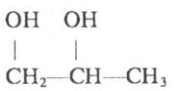	2:3 (1:1,5)	1 (-CH_3)
Butanediol-1,3	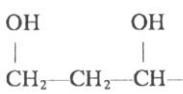	2:4 (1:2)	1 (-CH_3)
Butanediol-1,3	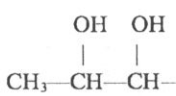	2:4 (1:2)	2 (-CH_3)
Pentanediol-1,5	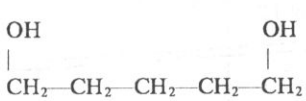	2:5 (1:2,5)	0
2-Methyl-pentanediol-2, 4	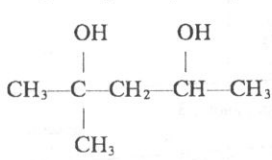	2:6 (1:3)	3 (-CH_3)
2-Ethyl-hexanediol-1, 3	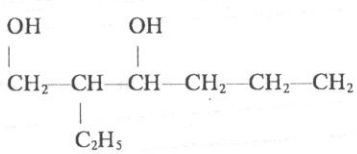	2:8 (1:4)	2 (-C_2H_5) (-C_3H_7)

– A Hoeppler and an ultrasonic viscometer UNIPAN 304A were used for viscosity measurements in temperature range 263 – 303 K. The stabilisation of temperature was better than $\pm$ 0.05 deg. and the values of the measured viscosity was determined with an accuracy of 2%,

– The ultrasonic shear resistance (R_T) in the high frequency range, (350 – 1300 MHz) was measured by means of a Matec instrument at the IFTR Warsaw [1, 2]. These measurements were performed in temperature range 218 – 243 K $\pm$ 0.1 deg. The shear mechanical resistance was determined with an accuracy of $\pm$ 10%.

4. Results

4.1. Density

The densities of the alcohols under test confirm a linear dependence on temperature according to the formula:

$$\rho = a + bT. \tag{7}$$

This relation is shown in Fig. 1 and the values of the coefficients a and b are listed in Table 2. The linear relationship between density and temperature allows to extrapolate

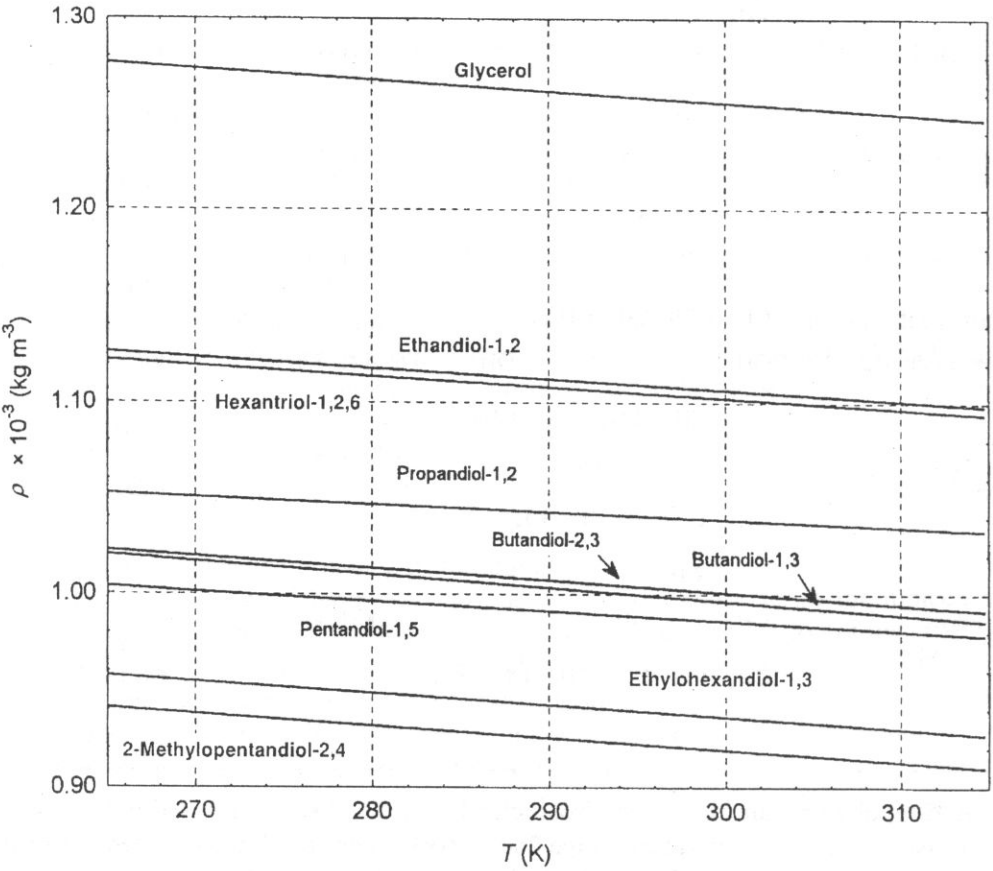

Fig. 1. The density of investigated alcohols as a function of temperature.

the density out of the measurement range. As shown in Table 2, the values of coefficients a and b of the alcohols tested do not differ much from each other, while the values of density increase in the following sequence:

Table 2. The coefficients a and b (Eq. 7) and c and d (Eq. 9) of investigated alcohols

ALCOHOL INVESTIGATED	DENSITY (kg/m³) [$\rho = a\text{-}bT$]			VISCOSITY (Pa·s) [$\lg\eta = c + dT^{-3}$]		
	a	b	r	c	d	r
1. GLYCEROL	$1.4360\ 10^3$	-0.6012 T	-0.9995	-3.6345	$0.93908\ 10^8\ T^{-3}$	0.0998
2. HEXANETROIL-1,2,6*	$1.2724\ 10^3$	-0.5671 T	-0.9997	-3.5278	$1.00231\ 10^8\ T^{-3}$	0.9998
3. ETHYLENE GLYCOL	$1.1218\ 10^3$	-0.5710 T	-0.9998	-3.6924	$0.49085\ 10^8\ T^{-3}$	0.9995
4. PROPANEDIOL-1,2	$1.0487\ 10^3$	-0.3750 T	-0.9994	-3.2237	$0.48346\ 10^8\ T^{-3}$	0.9972
5. BUTANEDIOL-1, 3	$1.0155\ 10^3$	-0.7090 T	-0.9997	-3.9602	$0.73287\ 10^8\ T^{-3}$	0.9995
6. BUTANEDIOL-2, 3	$1.0176\ 10^3$	-0.6290 T	-0.9999	-3.4451	$0.64036\ 10^8\ T^{-3}$	0.9996
7. PENTANEDIOL-1,5	$1.1382\ 10^3$	-0.5074 T	-0.9995	-3.1607	$0.57197\ 10^8\ T^{-3}$	0.9994
8. 2-METHYLOPENTANEDIOL-2,4	$1.1051\ 10^3$	-0.6197 T	-0.9996	-3.9021	$0.70763\ 10^8\ T^{-3}$	0.9999
9. 2-ETHYLOHEXANEDIOL-1,3	$1.1206\ 10^3$	-0.6150 T	-0.9992	-4.7946	$1.0532\ 10^8\ T^{-3}$	0.9989

* Densities and static viscosities were measured at the Institute of Chemistry, University of Wroclaw (3, 4).

Table 3. The coefficients m, n and r (reliablity) of Eq. (11) and values of activation energy E^* for different temperatures.

Alcohol investigated	Limiting shear modulus G_∞[N m^{-2}]			273 [K] η [Pa s]	E^H [kJ mol^{-1}]	G_∞ [N m^{-2}]	T_g [K]	T_o [K]	U [J] 10^{21}
	m	10^{-9}	$^n10^{-7}$ r						
1. Glycerol	.3831	-1.6883T	-0.9833	9.40	69.9	2.77	182	473	6.04
2. Hexanetriol-1, 2, 6	5.8840	-1.4250T	-0.9899	24.2	74,5	1.95	186	410	5.67
3. Ethanediol-1, 2	2.9199	-0.8910T	-0.9869	0.0519	36.5	0.487	146	328	4.53
4. Propanediol-1, 3	3.1224	-0.9211T	-0.9902	0.141	36.0	0.611	147	339	4.68
5. Butanediol-1, 3	4.3250	-1.1800T	-0.9963	0.432	54.6	1.10	166	366	5.06
6. Butanediol-1, 5	4.2293	-1.1122T	-0.9956	0.498	47.7	1.19	162	380	5.25
7. Pentanediol-1,5	2.6990	-0.9006T	-0.9872	0.442	42.6	0.239	156	300	4.13
8. 2-Methylopentanediol-2, 4	4.0951	-1.3269T	-0.9992	0.372	52.4	0.473	165	309	4.26
9. 2-Ethylohexanediol-1, 3	5.1380	-1.3786T	-0.9589	2.36	78.4	1.37	184	373	5.14

glycerin > glycol et. > hexanetriol -1.2.6 > propanediol -1.2 > butanediols -2.3 and -1.3 > 2-ethylheksanediol -1.3 > 2-methylpentanediol -2.4.

The numbers of -OH groups corresponding to one carbon atom in the molecule and thereby the densities of hydrogen bonds are ordered in the same sequence. This sequence of the densities may suggest an increasing compactness of the molecules. It is also of interest that the lowest values of density have been found for 2-ethylohek-sanediol -2.4, and 2-methylopentanediol -2.4, i.e. for the diols with relatively large molecules but with a low density of hydrogen bonds. In this case the low densities may be caused by an additional steric hindrance. This steric effect seems to be likely because the molecules of both the diols contain the sizable rigid groups $-CH_3$ and $-C_2H_5$ which may cause a lower compactness of the molecules.

4. 2. Viscosity

To present the relationship between viscosity and temperature, the Arrhe-nius-Guzman formula is usually used:

$$\eta = A\exp\left(\frac{E^*}{RT}\right), \tag{8}$$

where η is the viscosity, E^* – the activation energy of viscous flow, R – gas constant, T – temperature and A – a constant for a given liquid. However, the viscosities of the liquids studied do not follow the Arrenius-Guzman formula, and the viscosity temperature relation may by described by the logarithmic formula [5], [6]:

$$\ln\eta = c + dT^{-3}, \tag{9}$$

The viscosity-temperature relation is shown on Fig. 2.

The activation energy of viscous flow can be calculated with the formula:

$$E^* = R\left[\frac{\delta(\ln\eta)}{\delta(T^{-1})}\right] \tag{10}$$

where $\frac{\delta(\ln\eta)}{\delta(T^{-1})}$ is the tangential coefficient of the function (9) which may be related approxymately Arrenius-Guzman equation (8). The values of the activation energy E^* calculated for different temperatures are listed in Table 3. Both the density and steady flow viscosity measurements were performed at the Institute of Chemistry of the University of Wrocław [3, 4].

4.3. Shear mechanical resistance

The shear mechanical resistance was measured within the frequency range 350 – 1300 MHz. The results at low temperatures allow to determine the values of G_∞ and the elastic region of the tasted liquids. A linear dependence of G_∞ on temperature was found according to the formula:

$$G_\infty = m - nT.$$

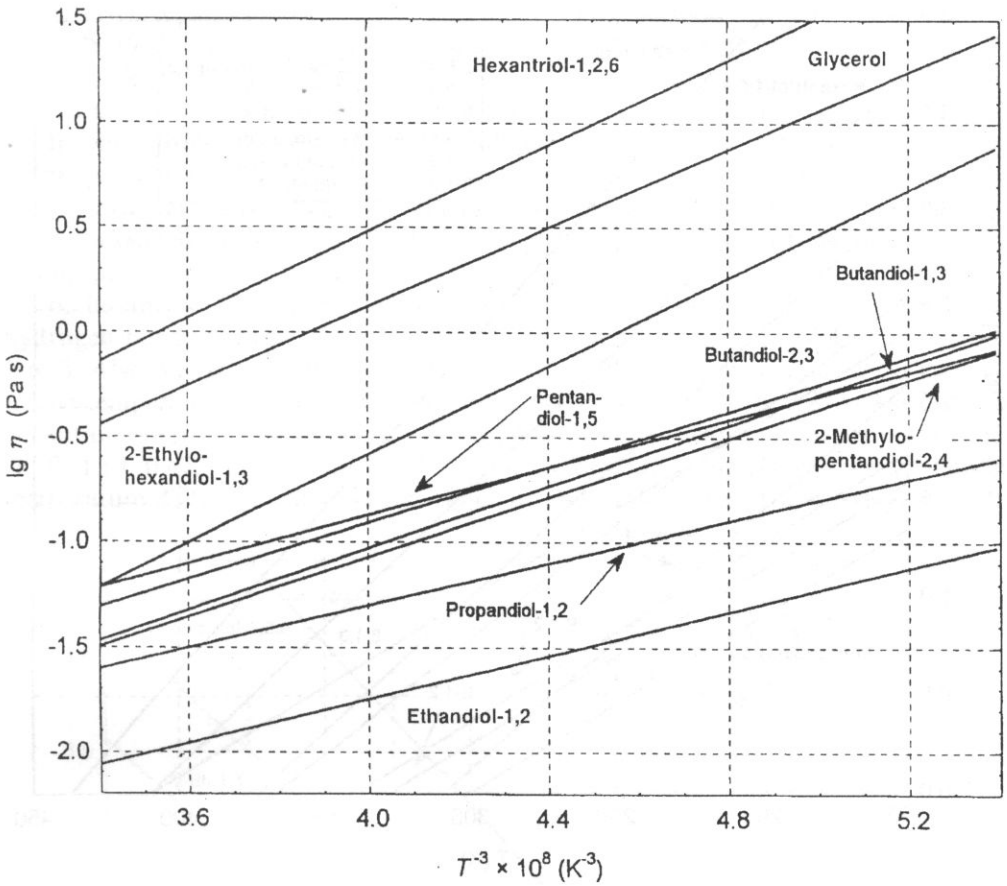

Fig. 2. Viscosity of investigated alcohols as a function of temperature.

The coefficients m and n of this equation are given in Table 3.

The extrapolation of G_∞ to the lower temperatures makes the determination of the glass transition temperature, T_g, possible. At that temperature the viscosity of a liquid is equal to 10^{12} Pa · s [8]. It is usually assumed that all relaxation processes in a liquid are locked up at the temperature T_g and the latter behaves as a solid. The values of T_g for investigated alcohols are given in Table 3. The linear dependence of G_∞ on temperature is shown in Fig. 3.

Issakovitch's and Caban's hole theory of very viscous liquids assumes the existence of two phases in a liquid with different arrangements of the molecules. The first phase consists of molecules in a pseudo-crystalline arrangement and the second one, a disordered phase, is made of free molecules. This mixture of two phases is in equilibrium at a given temperature and pressure. The ultrasonic wave, propagating in the liquid, disturbs the equilibrium between this two phases. A new equilibrium is reached by a diffusion processes after some time.

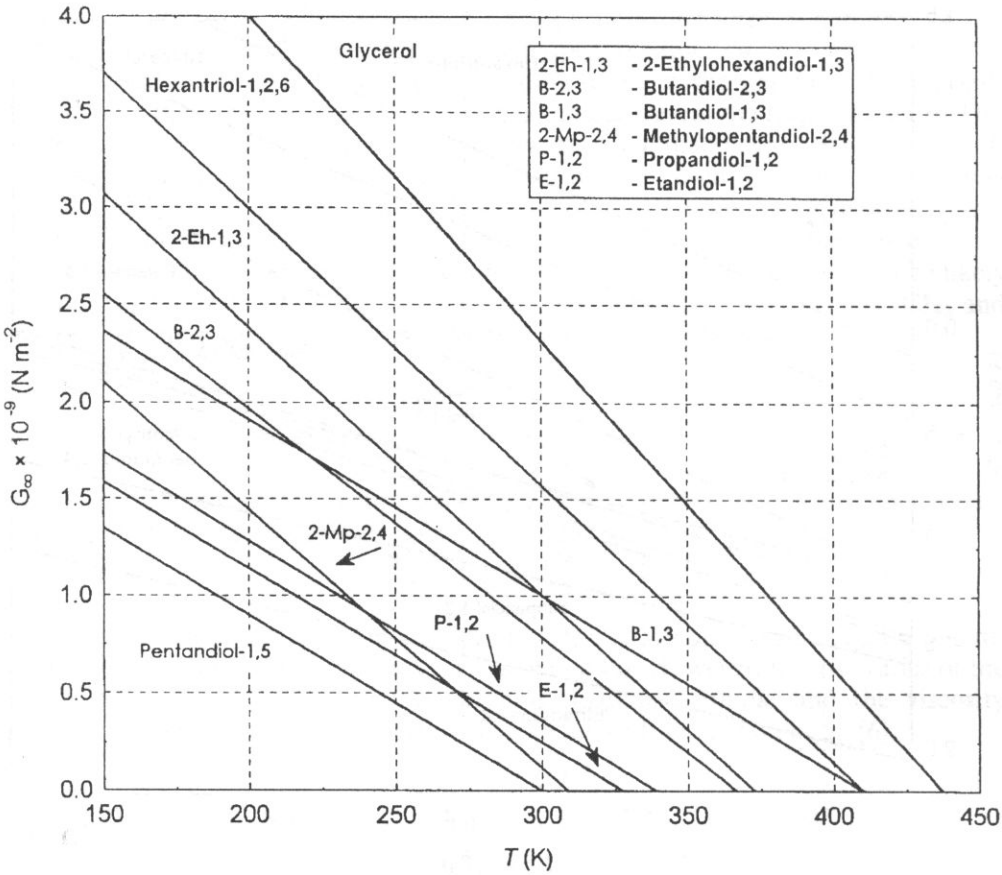

Fig. 3. G_∞ value of investigated alcohols as a function of temperature.

For a very high frequency the diffusion of holes is delayed in comparison with the stress variations. This causes a velocity dispersion and an additional absorption in the liquid. At the temperature T_0 the ordered phase diminishes and the longitudinal modulus K_0 and shear modulus G_∞ are equal to K_∞ and 0, respectively. At the temperature higher than T_0 all the molecules are free of any limitations due to the potential barrier, and the probability of any locations of a molecule is equal. From the linear dependence of G_∞ on temperature the values of the temperature T_0 and the interlocking potential barrier $U = KT_0$ (k is Boltzman constant) may be calculated.

All this values are given in Table 3.

5. Summary

To show the correlation between the chemical structure and space arrangements of molecules in the tested alcohols, the results may be divided into three groups

a) glycerol, hexanetriol -1.2.6 and 2 ethylheksanediol -1.3 show the highest viscosity, (9.40, 24, 2, 2, 36, Pa·s), the highest activation energy of viscous flow (69.9, 74.5, 78.4 kJ/mol), the highest values of the shear elasticity modulus G_∞ (2.77, 1.95, 1.37 N/m^2 × 10^9), and the lowest potential barrier.

In this group of alcohols large differences in the density of -OH groups (hydrogen bonds) and in the spatial arrangements exist. For example glycol and hexanetriol have any spatial arrangement of the alkyl groups, on the contrary, 2-ethylheksanetriol has big -C_2H_5 and C_3H_7 groups in a molecule, which are spatially arranged,

b) butanediol -1.3, pentanediol -2.3, 2 methylpentanediol -2.4, i.e. diols with hydrogen bonds density: 1/1, 1/2, 1/3 and an increasing amount of H bonds from 1 to 3. Also pentanediol -1.5 with H density bonds 1/2.5 and without alkyl groups. In the temperature 273 K the values of viscosity (0.432. 0.498, 0.372, 0.442 Pa·s), activation energy (54.6, 47.7, 52.4, 42.6 kJ/mol), and shear elasticity modulus G_∞ (1.10, 1.19, 0.473, 0.239 N/m^2 × 10^9), show moderate values. The glass transition temperature T_g for this alcohols is: 166K, 162K, 165K, 156K, respectively,

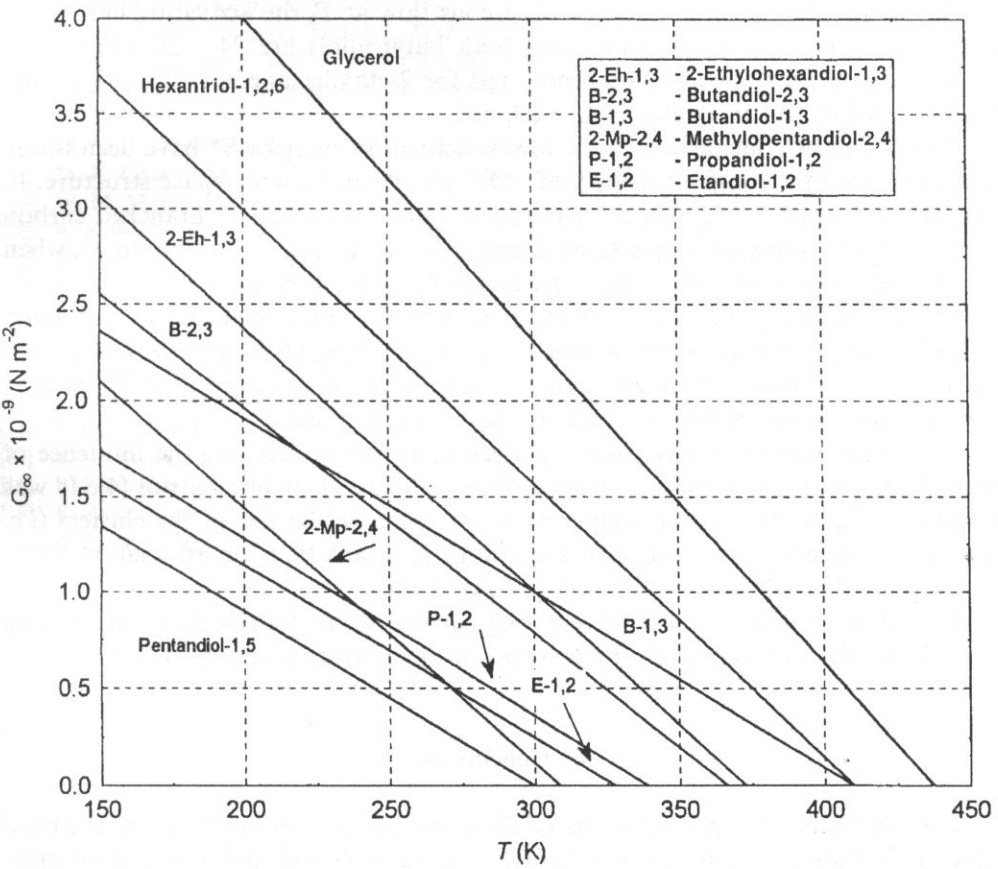

Fig. 4.

c) ethanediol -1.2 and propanediol -2.3 are diols with the lovest viscosities (0.052, 0.141 Pa·s) and the lowest activation energies (36.5, 36.0 kJ/mol). Their shear elasticity modulus G_∞ is 0.487 and 0.611 N/m^2 and the potential barriere are 2.73 10^3 and 2.82 10^3 J/mol. They differ from each other in the – OH group density (1 : 1 and 2 : 3) and the number of methyl groups (0 and 1). Their glass transition temperature is 146 K and 147 K, respectively.

Such division into three groups show the influence of –OH groups (hydrogen bonds) and alkyl groups -CH_3, -C_2H_5 or C_3H_7 on the results of measurements. The –OH groups may create a big associates (clusters), which limit the rotation and translation degrees of freedom of the molecules (i.e. the hydrogen bond model of MADIGOSKY, MCDUFFY and LITOVITZ [9] [10].

The alkyl groups may block the free space in a cluster structure. This suggestion is confirmed by other investigations of the elasticity and shear compressibility of other mixtures of alcohols [11]. Larger deviations of the compressibility for glycerol -2 methyl-pentanediol-2.4 mixture than for glycerol-butanediol -1.3 were found in this mixtures.

As regards the activation energy of viscous flow at T_0 the activation energy for glycerol, ethylene glycol, propanol and both butanediols are 24 – 26 kJ/mol, for hexanetriol and pentanediol 34 kJ/mol, and for 2-ethylhexanediol -1.3 and 2 methylopentanediol -2.4 this value is 42.5 kJ/mol.

Thus it can be concluded that the lowest activation energies E^* have been found for alcohols with the highest density of –OH groups and a week space structure. In contrary, the highest values of E^* have been found for diols with branched carbon chains and with a low hydrogen bond density. At the temperatures close to T_0, when the ordered phase diminishes, the steric factor becomes more important.

In the case of hexanetriol -1.2.6 and pentanediol -1.5 i.e. the alcohols with long, and unbranched carbon chains (without side alkyl groups) and with low -OH groups densities, the relatively high value of the activation energy may be explained by a strong association through intermolecular hydrogen bonds.

This suggestion is in agreement with earlier results concerning the influence of electrolytes on the structural and viscoelastic relaxation of heksantriol [4]. It was found that the electrolyte has only a week influence on the size of the clusters (i.e. there are weak effects of structural solvation). It means that the association limits the range of the influence of the electric field of ions.

The effect of joining the relatively long carbon chains (interlocking effects) can be the other factor that causes the increase of the activation energy [12] [13].

6. Conclusion

The results of this investigations confirm the correlation between the chemical structure and spatial arrangement of polyhydric alcohols and their reaction on shear ultrasonic strain in the viscous range (viscosity, activation energy) and elastic range

(shear elastic modulus). The results are in agreement with earlier results of investigation of alcohols and electrolyte solutions, according to that the concentration of hydrogen bonds correlates with the reaction on shear stress [14-20].

Acknowledgements

We thank prof St. ERNST of Institute of Chemistry Silesian University for helpful suggestion concerning this publication. Thanks are also due to A. BALCERZAK for the correction of english version.

References

[1] R. PŁOWIEC, Archiwum Akustyki, **5,** 4 (1970).
[2] N. B. LIEŻNIEW, Prace IPPT-PAN 45 (1978).
[3] S. ERNST and J. GLIŃSKI, Mat. Sci., **IV/2**, 81 (1978).
[4] S. ERNST and J. GLIŃSKI, Mat. Sci., **IV/2**, 45 (1978).
[5] R. PICCIRELLI and T. A. LITOVITZ, JASA, **29,** 1009 (1957).
[6] R. MEISTER, C. J. MARHOFFER, R. SCIAMANDA, L. COTTER and T. A. LITOVITZ, J. Appl. Phys., **31,** 5, 854 (1960).
[7] M. A. ISSAKOWICZ and J. A. CZABAN, Żurn. Eksp. Teoret. Fiz., **50,** 1343 (1966).
[8] M. R. CARPENTER, D. B. DAVIES and A. J. MATHESON, J. Chem. Phys., 46, 2451 (1967).
[9] W. M. MADIGOSKY, G. E. MC DUFFIE and T. A. LITOVITZ, J. Chem. Phys., **47**, 753- (1967).
[10] R. KONO, G. E. MCDUFFIE and T. A. LITOVITZ, J. Chem. Phys., **44,** 965 (1966).
[11] M. WACIŃSKI, K. BEBEK, E. ZARĘBSKI, Archiwum Akustyki, **9,** 3 (1984).
[12] J. VAN LEOF, J. Chem. Phys., **61,** 1605 (1974).
[13] J. J. VAN LEOF, Physica, **79B**, 86 (1975).
[14] S. ERNST and J. O. DZIĘGIELEWSKI, *Niektóre problemy fizykochemicznych badań roztworów*, Prace Naukowe Uniw. Śląskiego, Katowice 1986.
[15] S. ERNST, E. SOCZKIEWICZ and J. GLIŃSKI, Acustica, **56,** 2, (1984).
[16] S. ERNST and E. SOCZKIEWICZ, Acustica, **56,** 59 (1984).
[17] S. ERNST, K. BEBEK, E. ZORĘBSKI and E. SOCZKIEWICZ, Acta Phys. Slovakia **36** (1986).
[18] E. ZORĘBSKI, S. ERNST and E. SOCZKIEWICZ, Acustica, **62**, 151 (1986).
[19] E. ZARĘBSKI and S. ERNST, Acta Phys. Slovakia, **40** (1990).
[20] S. ERNST, E. ZORĘBSKI and K. BEBEK, Acustica, **72** (1990).

ARCHIVES OF ACOUSTICS
21, 4, 459–462 (1996)

C H R O N I C L E

100 th AES Convention in Copenhagen

Audio Engineering Society Conventions are organized regularly on a worldwide scale twice a year. The Spring Conventions in Europe are detoned with subsequent even numbers, while the Fall Conventions in America – with odd ones. All AES Conventions, apart from other more specialized meetings, such as e.g. AES Conferences, separately numbered, bear a specified character. They are, first of all, organizational meetings of the AES-Board of Governors with the Region- and Section-Officers, and Members of numerous AES Committees, as well of the Headquarters and Regional Offices. All members comming from various countries work together intensively during the Convention days, taking adventage of the direct personal contacts and opportunity for discussion.

It should be noticed here that the AES, although registered in its actual legal stature in the USA in 1955, was founded already in 1948 and had started its broader activities with First Convention held in New York City in 1949. The AES soon became a true international society. Actually, there are 92 AES Sections all over the World, 48 being in the USA. All AES Sections are grouped into seven AES Regions: three in North America (USA and Canada), three in Europe, and one for Sections situated in other parts of the World. So much of the general information about AES on the occasion of its jubilee Convention.

The 100 th Convention held at the Bella Center in Copenhagen, on May, 11 to 14, 1996 was, due to its "rounded" number, the Jubilee event for the AES, and so it was treated by the Danish Section Organizing Committee. Thanks to its initiatives a major historical landmark was achieved with this Convention. The number of submitted papers was the greatest ever received by the AES Convention and after selection 155 were chosen for presentation; up to three parallel sessions were organized in order to accommodate them. The number of workshops was also greater than ever. It should be added that Copenhagen was declared for the year 1996 the Cultural Capital of Europe, which contributed to the attractiveness of the Convention due to the number of accompanying events in the City, which were very interesting for the visitors.

The texts of 132 papers were edited as AES Preprints, prior to the debates. It may be worth mentioning that further 35 papers submitted were rejected by the Papers Chairmen, which proves the quality requirements were kept on a high level.

The most spectacular achievement of the convention was the huge exhibition, where more than three hundreds of the World leading enterprises, active on the pro-audio market, presented their latest products. Only one exhibitor from Poland participated therein (TOMMEX). The exhibition attracted numerous visitors from all over the World of course, Although the total attendance was reported to be around 7500, i.e. about one thousand less than during the 98th Convention in Paris, last year, the quality of participants and their professional interests were assessed as highly satisfying.

The scientific part of the Convention was organized into 20 sectional debates devoted to the following subjects:

Architectural Acoustics & Sound Reinforcement (Pt. I, II),
Musical Instuments Acoustics & Electronic Music,
Psychoacoustics, Hearing & Hearing Instruments (Pt. I, II),
Music Induced Hearing Impairment,
Transducers (Pt. I, II),
Recording & Reproduction Systems,
Audio in Broadcasting, Production Techniques & Transmission,
Signal Processing (Pt. I, II, III),
Perceptual Coding (Pt. I, II),
Multichannel Sound Systems & Multimedia,
Wave Field Synthesis in Audio Applications,
Auralization & Virtual Reality,
Measurements & Instrumentation (Pt. I, II).

The content of the workshop sessions was more diversified than ever. The following topics were presented (among others):

- Safeguarding the Audio Heritage for the Future,
- The Interaction of the Visual and Auditory Senses,
- Audio and Video Carriers, Technical and Organization Aspects,
- Use of Miniature Microphones in Theatre and Television,
- Perceptual Encoding: Subjective and Objective Methods of Evaluation,
- High Resolution Audio Mastering,
- Multichannel Sound Production Techniques,
- The digital Broadcasting House of the Future.

The last workshop was repeated many times and demonstrated at the special stand built at the Convention site as well as in the House of the Danish Radio in Copenhagen. The Danish Radio already implemented its DAR (Digital Audio Broadcasting) system and has it fully operational.

The participation of the Polish AES Section members and other Polish attendees was remarkable. Thirteen papers (i.e. ca. 10% of the total number) were published in Preprints, and read discussed during the session debates. They were written by 19 authors, or coauthors, coming from: Gdańsk (9), Wrocław (8), Warszawa (1), Poznań (1). A numerous group of students (41 – mostly from the Gdańsk TU) participated, first of all in workshop sessions. There were altogether over 150

persons from Poland. They took adventage of many cultural and social events which were available during the Convention period, and, besides, they had an excellent occasion to visit the beautiful City of Copenhagen in May.

The numerous participation of the Poles was possible thanks to the relatively cheap and easy sea-transport do Denmark, offered by the Polish Maritime Ferry Lines, between Świnoujście and Copenhagen. Despite stormy weather and rough sea during the forth-trip, which, may be, enriched the impressions of some of the participants, the whole outcome of the Polish participation in the 100th AES Convention, similar to the several previous ones, may be summed up as a successful one.

To end – some useful information about future AES Conventions. The 101st will be held in Los Angeles, November, 8-11, 1996. The 102nd – in Munich, March, 22-25, 1997. Further Convention sites are still under discussion.

Marianna Sankiewicz

As an enclosure to this Chronicle a list of papers published by Polish authors during the 100 th AES Convention is quoted below.

A. Czyżewski, P. Skórka „Modifications of the Auditory Feedback Loop Hearing and Speech Production" (Preprint 4148).

A. Czyżewski, A. Lorens „Testing some DSP Algorithms for Hearing Aidsand Cochlear Implants" (Preprint 4149)

M. J. Kin „Perception of Amplitude Modulation in Harmonic Complexes" (Preprint 4151)

T. Janeczko „Synthesis of Complex Audio Spectra by Computer Simulation of Chua's Circuit" (Preprint 4168)

B. Kostek, M. Szczerba „MIDI Database for the automatic Recognition of Musical Phrases" (Preprint 4169)

S. K. Zieliński „Digital Waveguide Modeling versus Mathematical Modeling of Organ Flue Pipe" (Preprint 4170)

M. Sankiewicz, G. Budzyński „Analysis of Dissonances in Carillon Chords" (Preprint 4172)

B. Kostek, A Wieczorkowska „Study of Parameter Relations in Musical Instruments Patterns" (Preprint 4173)

R. Królikowski „Noise Reduction in Old Musical Recordings Using the Perceptual Coding of audio" (Preprint 4180)

M. Niewiarowicz „The Analysis of spatial Distribution of Signals Emitted by a Loudspeaker-system" (Preprint 4182)

A. Dobrucki, P. Pruchnicki, B. Żółtogórski „Computer Modeling of Loudspeaker Vibrating System" (Preprint 4207)

K. Baściuk, S. Brachmański „Relation between Logatom Intelligibility and SNR Enhaced speach" (Preprint 4218)

C. Szmal „Subjective Evaluation of Sound Recordings versus Sound Spectra" (Preprint 4239)

13th FASE SYMPOSIUM
on Hydroacoustics and Ultrasonics
Jurata 12-16 May 1997

We are pleased to inform you that the XII-th FASE Symposium will be held in Jurata in May 1997. Jurata is placed on the Hel Peninsula 100 km from Gdańsk. The Hel Peninsula is quite unusual as it is 35 km long and only 300 m wide at the base. After Jurata it gradually broadens and reaches about 3 km. Nice, sandy beaches and ferry connection with Gdańsk or Gdynia make it a tourist attraction.

Organizers

The Symposium is organized by the Acoustical Committee of the Polish Academy of Sciences, the Polish Acoustical Society, the Naval Academy in Gdynia in co-operation with the Technical University of Gdańsk.

Technical programme

The main areas of the Symposium are hydroacoustics and ultrasonic technique. The topics include: acoustic noicse, underwater propagation in sea, underwater acoustic systems and devices, signal processing, nonlinear acoustics, ultrasonic transducers and arrays. Papers in the acoustics, ultrasonic transducers and arrays. Paper in the areas covered by the Symposium and similar tipics are welcome. The papers will be published in the "Proceedings of the XIIIth FASE Symposium".
The Symposium will include plenary lecture sessions, contributed and invited paper sessions, poster sessions and exhibition.

Address of the Organizing Committee

prof. Eugeniusz Kozaczka
Akademia Marynarki Wojennej
ul. Śmidowicza 71
81-919 Gdynia
Poland

fax: (+ +48-58) 25 48 46
e. mail: amw beta.nask.gda.pl
tel.: (+ +48-58) 26 28 72, 26 28 68